BeFo
STIFTELSEN BERGTEKNISK FORSKNING
ROCK ENGINEERING RESEARCH FOUNDATION

IMPACT OF FIRE ON THE STABILITY OF HARD ROCK TUNNELS IN SWEDEN

Erling Nordlund
Ping Zhang
Savka Dineva
Christine Saiang
Ganesh Mainali

BeFo Report 136

STIFTELSEN BERGTEKNISK FORSKNING
ROCK ENGINEERING RESEARCH FOUNDATION

IMPACT OF FIRE ON THE STABILITY OF HARD ROCK TUNNELS IN SWEDEN

Effekten av bränder på stabiliteten i svenska tunnlar

Erling Nordlund, Luleå University of Technology
Ping Zhang, Luleå University of Technology
Savka Dineva, Luleå University of Technology
Christine Saiang, Luleå University of Technology
Ganesh Mainali, Luleå University of Technology

BeFo Report 136
Stockholm 2014
ISSN 1104 – 1773
ISRN BEFO-R—136—SE

PREFACE

Safety in tunnels and mine drifts must have top priority so that people can travel and reside underground without being affected by accidents. Unfortunately, several tunnel fires around the world last 15 years have struck people, why safety should be prioritized everywhere. There is a need to know, not only how to build safe escape routes, alarm systems, video-surveillance etcetera, but also to have knowledge of the thermal properties for material in the tunnel systems. Rock is one of the main components in the structural system for underground hard rock openings.

Often, the rock surface is covered with shotcrete, but thinner shotcrete protects the rock only for a short time. Thick concrete may spall successively. Rock subjected to high temperature, e.g. during a vigorous fire, will initially start spalling. The understanding of rock behavior during thermal spalling is limited, and the objective for research is to build knowledge.

The research was, except for an initial literature survey, performed using rock samples heated in the laboratory to certain levels with a maximum of 1100°C. Three different rock types where used; granite, gabbro and schist. For different temperature levels the difference in material compressive strength, mineralogy, and micro-cracks where registered. By monitoring acoustic emission (AE) events at heating/cooling in 3D, the special micro-seismic even map was compared with other changes due to thermal change. Also, grain-scale numerical modelling and larger scale modelling (macro-mechanical model) were carried out as part of the project. A combination of several methods, as in this research project, will give more solid conclusions.

The research project generated a large amount of data to be handled scientifically and the result will surely be valuable for researchers as well as the engineering community.

This research was performed at the Luleå University of Technology by the group Erling Nordlund, Ping Zhang, Savka Dineva, Christine Saiang and Ganesh Mainali under the supervision of Erling Nordlund. A reference group assisted the project and was composed of Rolf Christiansson (SKB), Per Vedin (Transportstyrelsen, previously employed by the Swedish Transport Administration) and Per Tengborg (BeFo). The research funding was by the Rock Engineering Research Foundation (BeFo) together with the Swedish Transport Administration (Previous Banverket), SKB, Vattenfall, Formas and CAMM at the Luleå University of Technology.

Stockholm in November 2014

Per Tengborg

FÖRORD

Säkerhet i tunnlar och gruvorter ska ha högsta prioritet så att människor ska kunna transportera sig och vistas under jord utan att drabbas av olyckor. Tyvärr har fler tunnelbränder runt om i världen de senaste 15 åren drabbat människor, så säkerhetsproblematiken bör stå högt på agendan överallt. Förutom att projektera och bygga säkra utrymningsvägar, larmsystem, kameraövervakning mm så behöver vi också ha kunskap om termiska egenskaper för de material som tunnelsystemen är uppbyggda av. I våra bergtunnlar ingår berget som en huvudkomponent i det bärande huvudsystemet.

Ofta är bergytan täckt med sprutbetong, men tunnare sprutbetongskikt skyddar inte berget mer än kort tid. Tjockare betongskikt kan succesivt spjälkas av. När berget utsätts för höga temperaturer, t ex i samband med en kraftig brand, så kan en spjälkning av själva berget inledas. Förståelsen av bergets beteende vid termisk spjälkning är begränsad, och grunden till detta forskningsprojekt är att bygga upp denna kunskap.

Forskningen har förutom en inledande litteraturstudie utförts med bergprover som hettats upp i laboratorium till olika temperaturnivåer med maximalt 1100°C. Tre olika bergartstyper har använts; granit, gabbro och skiffer. Vid de olika temperaturnivåerna registreras förändringar av materialets tryckhållfasthet, mineralogi och mikrosprickor. Genom att mäta akustisk emission (AE) under upphettning/avsvalning i 3D ger AE-händelser en rumslig bild som kan jämföras med övriga förändringar. Vidare har numerisk modellering i såväl kornskala som större skala (makromekanisk modell) utförts som en del i projektet. Genom att kombinera flera metoder som är fallet här kan forskningens slutsatser bli bättre underbyggda.

Forskningsarbetet har genererat en omfattande mängd data att hantera vetenskapligt och resultatet kommer säkert att vara värdefullt för såväl forskare som ingenjörer.

Forskningen har bedrivits vid Luleå Tekniska Universitet av gruppen Erling Nordlund, Ping Zhang, Savka Dineva, Christine Saiang och Ganesh Mainali under ledning av Erling Nordlund. Den referensgrupp som har bistått forskarna och bidragit med råd bestod av Rolf Christiansson (SKB), Per Vedin (Transportstyrelsen, tidigare anställd vid Trafikverket) och Per Tengborg (BeFo). Forskningsarbetet finansierades av Stiftelsen Bergteknisk Forskning (BeFo) tillsammans med Trafikverket (f d Banverket), SKB, Vattenfall, Formas och CAMM vid Luleå Tekniska Universitet.

Stockholm i november 2014
Per Tengborg

Summary

In Sweden the majority of the tunnels are within hard rock, e.g. granite, granodiorite, gneiss, and gabbro and mainly supported with rock bolts and shotcrete. When the shotcrete lining is thin or non-existent, the rock will quickly be exposed to high temperatures caused by a tunnel fire. Rock with thicker shotcrete lining may also be exposed to fire if spalling of the shotcrete occurs. The objectives of the reported research project were to (i) determine the mechanism causing rock spalling observed in laboratory experiments, (ii) determine the type and extension of damage around rock tunnels caused by fire of a certain "size". The studied rock types were granite, gabbro and schist.

The project comprised the following activities (i) Investigations of the effect of slow heating on core-based rock samples, (ii) Physical model tests: Rock blocks exposed to uniform and point heating, respectively, (iii) Physical model tests: Simulated small scale tunnel subjected to heating and (iv) Numerical analyses of the physical model tests by using both macro-scale continuous and grain-scale discontinuous models (Voronoi tessellation).

The studies of the heated core-based samples showed (i) Similar trends with regard to the variation of their mechanical behaviour when subjected to different temperature levels for all tested rock types, (ii) Reasonable correlation between changes in the mechanical properties and the mineralogical changes and the accompanying changes in the micro-crack density for the tested rock types at the different temperature levels, (iii) A clear relationship between the density of micro-cracks and the temperature (increase with increasing maximum temperature) (iv) A significant influence of the micro-crack density, measured in terms of specific crack lengths, on the compressive strengths of the rocks, particularly for the temperature levels of 750°C and 1100°C. At 1100°C the samples were highly friable and crumbled easily upon compression.

The most general conclusions that could be made from the uniform and local heating tests are: (i) Micro-cracking is substantial in granite and gabbro – a large number of AE are generated during both local and uniform heating, (ii) During uniform heating the initiation of micro-cracks took place 2-3 minutes after the fire start (~700°C oven temperature, for all rock types). (iii) The propagation of micro-cracks continues also during the cooling process for gabbro and granite but not for schist, (iv) The micro-cracks in all rock types are predominantly tensile, (v) The visual cracks on the surface of the rock blocks correlate very well with the dense AE event location in the rock block. The macroscopic observations gave the following conclusions: (a) Granite: showed substantial explosive spalling, (b) Gabbro showed only surface pitting and it was only a temporary process and (c) Schist presented delamination failure along layers due to different thermal expansion between layers and low interfacial bond strength.

The results of the grain-scale numerical simulations highlighted the importance of microstructural effects in determining the mechanical response of granite and gabbro under thermal spallation conditions. The agreement with the laboratory tests illustrates that the modelling approach is able to reveal a complex fracturing process and failure mechanism. However, this kind of high resolution models are not practical for tunnel scale simulations. Therefore, a macro-mechanical continuous model was developed for future large scale simulation.

The results from the macro-mechanical model are in reasonable agreement with the important phenomena recorded or observed from the lab tests during all of the heating phases. The main shortcoming of the macro-mechanical (continuous) model is that it does not have the capacity to simulate the stress release due to initiation and propagation of remote tensile fractures.

The results from the analysis of the acoustic emission generated during the process of rock heating (uniform and local) provided valuable information on the number, timing, position, and size of micro-cracks developed in the test blocks during local and uniform heating. AE events could reveal not only the processes of initiation, development and expansion of micro-fractures inside the rock block but could also give an indication of active weakness planes /zones.

Key words: Tunnel fire, Failre propagation, Spalling, Acoustic emission, micro cracks

Sammanfattning

Majoriteten av tunnlarna i Sverige är byggda i hårt berg, t ex granit, granodiorit, gnejs och gabbro och förstärkta med bultar och sprutbetong. När sprutbetongförstärkningen är tunn eller saknas utsätts berget snabbt för höga temperaturer vid en tunnelbrand. När sprutbetongens tjocklek är större kan fortfarande berget exponeras för höga temperaturer. Men detta kräver då att ett progressivt spjälkbrott inträffar i sprutbetongen.

Målen med det rapporterade projektet var att (i) identifiera mekanismerna som leder till spjälkbrott i berg som exponeras för höga temperaturer i laboratoriemiljö, (ii) bestämma typ och omfattning på den skadezon som orsakats av en tunnelbrand av en viss ”storlek”. De studerade bergarterna var granit, gabbro och skiffer.

Projektet omfattade följande aktiviteter: (i) Studier av hur långsam upphettning påverkar kärnprovers egenskaper, (ii) Fysiska modelltester: Bergblock som upphettas (med hjälp av gaslåga) jämnt över en stor yta respektive på ett punktformigt sätt, (iii) Modelltester: Simulerad småskalig tunnelbrand och (iv) Numeriska analyser av de fysiska modellförsöken med hjälp av makromekaniska kontinuerliga modeller samt diskontinuerliga modeller i kornskala (Voronoi tesselation).

Studierna av upphettade kärnprover visade (i) Liknande trender för alla testade bergarter med avseende på variationen i mekaniska egenskaper när de upphettades till olika maximala temperaturer, (ii) Rimlig korrelation mellan förändringar i mekaniska egenskaper och förändringarna i mineralogi och mikrouppsprickning för de olika maximala temperaturer proverna utsattes för, (iii) Ett klart samband mellan mikrosprickdensiteten och temperaturen (ökad med ökad temperatur), (iv) Ett signifikant samband mellan bergarternas enaxiella tryckhållfasthet och mikrouppsprickningen (spricklängd), speciellt efter upphettning till 750°C och 1100°C. Efter att ha upphettas till 1100°C var vissa provkroppar mycket sköra och föll lätt sönder vid tryckbelastning.

Den mest generella slutsatsen som kan dras från blocktesterna med jämnt utbredd respektive punktformad upphettning är (i) Mikrouppsprickningen är påtaglig i granit och gabbro – Ett stort antal AE registrerades under både upphettnings- och avsvalningsfasen, (ii) Under jämnt utbredd upphettning initierades mikrouppsprickningen 2 – 3 minuter efter det att upphettningen påbörjades (~700°C ugnstemperatur, för alla bergartstyper), (iii) Propageringen av mikrosprickor fortsatte också under avsvalningsfasen för gabbro och granit men inte för skiffer, (iv) Mikrosprickorna i alla testade bergartstyper var av dragtyp, (v) De visuella sprickorna på blockens yta korrelerade väl med områden med hög densitet av AE händelser. De makroskopiska observationerna gav följande slutsatser: (a) Granitblocken uppvisade omfattande explosiv spjälkning, (b) Gabbro: på den upphettade ytan observerades endast ytlig spjälkning och den var bara en temporär brottmekanism och (c) Skiffern uppvisade brott i form av separation längs förskiffringens plan.

Resultaten från de numeriska modellerna i kornskala påvisade de mikrostrukturella effekternas betydelse för den mekaniska responsen hos granit och gabbro under termisk spjälkning och vikten av att ta hänsyn till detta i analyserna. Överensstämmelsen mellan dessa numeriska modeller och laboratorietesterna visar att denna typ av numeriska analyser kan användas för att upptäcka komplexa uppsprickningsprocesser och brottmekanismer. Men

denna typ av modeller med hög upplösning är inte lämpliga för analyser i tunnelskala. En makromekanisk kontinuerlig modell utvecklades därför för analyser i tunnelskala.

Resultaten från de makromekaniska modellen överensstämmer relativt väl med de viktiga fenomen som uppmätts och observerats under laboratorieförsöken under alla upphettningsstadier. Den huvudsakliga svagheten med den makromekaniska modellen är att den inte kan simulera spänningsavlastning orsakad av initiering och propagering av dragsprickor på större avstånd från värmekällan.

Den akustiska emission som genereras under upphettning (både under jämnt utbredd och punktformad) av bergblocken gav värdefull information om antal mikrosprickor, när de inträffade, deras position och storlek med avseende på energifrigörelse. AE detekterade inte bara initiering och propagering av mikrosprickor men identifierade också aktiva svaghetsplan/zoner.

Nyckelord: Tunnebrand, Brottutveckling, Spjälkning, Akustisk emission, mikrosprickor

TABLE OF CONTENTS

1 INTRODUCTION

1.1 Background

During the last ten years a number of tunnel fires with fatalities have taken place all over the world. The damages which were caused by the fires were extensive and have led to an intensive debate and initiated research about tunnel safety in Europe and in the rest of the world (Beard and Carvel, 2005).

The majority of the tunnels in Sweden are within hard rock, e.g. granite, granodiorite, gneiss, sandstone and gabbro. In these tunnels, concrete lining is not a normal support. The main support in Swedish tunnels comprises bolt and shotcrete with a thickness of maximum 20 cm (Larsson, 2006). When the shotcrete lining is thin or non-existent, the rock will quickly be exposed to high temperature caused by a tunnel fire (Boström, 2009). Rock with thicker shotcrete lining may also be exposed to fire if spalling of the shotcrete occurs.

The phenomenon of thermal spalling has been observed for some rocks under high temperature (Hettema et al., 1998; Poirier et al., 2003; Smith and Pells, 2008). Extensive research efforts have been made to understand the phenomenon of fire-induced thermal spalling of concrete. However, only limited research efforts have been made within the area of fire-induced spalling of rock (Khoury, 2000; Jansson and Boström, 2008). Some rock types show spalling behaviour but this is not generally the case (Williams et al., 1996; Zhang et al., 2010, 2011). The relationship between rock type (lithology) and the tendency to spall should be assessed. Besides the occurrence of spalling, further research is needed to determine whether spalling is just a temporary surface process or if it can be a continuous surface process throughout the fire. This requires a thorough understanding of the transient processes during spalling and calls for experiments on large samples. Only if the matters regarding occurrence and continuity are resolved, the effect of spalling on the stability of heated tunnels can be predicted.

In a previous project carried out at Luleå University of Technology (Larsson, 2006; Jonsson, 2009; Zhang et al., 2010), the behaviour of different igneous and metamorphic rock types exposed to a high temperature fire had been assessed and the influence of temperature on the mechanical properties of these rock types had been established. However, the spalling mechanism and its prediction were still not well understood.

1.2 State of the art

The impact of fire on rock material has been investigated in the area of rock made art (Tratebas et al., 2004), where culturally priceless works of ancient art are lost to fire every year. The petrological, petrophysical, and mechanical investigations have shown that the texture and mineral composition of sandstones change due to heating. The rock matrix material was assessed to be the primary reason for the changes (Hajpál, 2002, 2004). However, spalling, one of the important effects of fire in hard rock tunnels was not considered.

Thermal spalling, defined here as the process causing fracturing and removal of surface material by the action of heat (Hettema, 1996), is not identical with thermal fracture. Preston and White (1934) pointed out that a characteristic feature of a spall is that it is suddenly removed with enough violence to make an audible noise. Mechanical spalling, as a brittle fracture process, has attracted many researchers' interests and has been widely studied in rock mechanics and rock engineering (Diederichs, 2007; Edelbro, 2010). However, there are important differences between mechanical (isothermal) spalling and thermally induced spalling (Hettema, 1996):

- Thermal compressive stresses near to the surface are non-uniform and change in time.
- Differential thermal expansion results in internal stresses.
- Under the influence of temperature the mechanical properties of rocks change.
- Thermal spalling is violent, but mechanical spalling can be violent or non-violent and in some cases can be time dependent (Preston and White,1934; Diederichs, 2007).

Spalling behaviour of rock-like brittle materials subjected to temperature changes has been of interest to glass, ceramic and refractory industries mining engineering (Rauenzahn and Tester, 1989; Poirier et al., 2003), but the mechanism and its prediction are still overlooked.

Hettema et al. (1998) performed three types of laboratory experiments to determine the conditions under which spalling occurs for sedimentary rock. The results from uniform heating experiments and from linear heating rate experiments have led to the conclusion that explosive spalling is caused by saturated steam alone. Spalling due to thermal shock is probably caused by a combination of steam pressure and fracturing associated with high compressive thermal stress.

However, only a few laboratory tests aimed at the behaviour of rocks during a fire on the basis of the so-called temperature time curve in ''standard'' fires have been reported in the literature. The Technical Research Centre of Finland (Keski-Rahkonen et al., 1986) conducted two full scale tests in a 6 m wide by 5 m high tunnel in a limestone quarry in 1985. The rock surface was wet, unreinforced and unprotected. In the first test, after 25 min of fire the first ''strong hollow sound'' was heard caused by falling rock. At the end of the experiment there was a large amount of spalled rock on the floor of the tunnel, typically in the form of large ''flakes'' with a thickness of 50 mm to 150 mm. In the second test, spalling of rock occurred to a lesser extent than in the first test due to the mineral wool used for protecting the ceiling over a 5 m×5 m patch. The investigators gave no explanations of the mechanisms of spalling and they simply noted that ''*this spalling is highly hazardous for both the instrumentation and the people working in the tunnel*''. The Handbook of Tunnel Fire Safety (Beard and Carvel, 2005) also stated: ''*Practical fire trials carried out in Sweden by the Telia telephone company also showed the considerable risks due to the collapse of tunnels as a result of fire when large blocks of rock collapsed*.''

For this reason, Smith and Pells (2008) conducted a field test on a big rock cutting and assessed how exposed sandstone is likely to respond in a fire. Spalling of Hawkesbury sandstone occurred after only a few minutes of exposure to fire. The extreme temperatures given in standard fire curves are not required to cause explosive spalling. Only a few hundred degrees may be sufficient. The mechanism causing spalling appears to be primarily the generation of steam pressure. The conclusion was later confirmed by a truck fire accident in

Sydney in January, 2008. The thickness of sandstone spalled was up to 300 mm(Smith and Pells, 2009).

From the above it is reasonable to conclude that the matter of rock behaviour during and after high temperature tunnel fires is an important but poorly understood issue, especially for igneous and metamorphic hard rock. Furthermore, the following properties and conditions can be concluded to promote the tendency of rock to spall:

- mineral composition of rock,
- high surface heating rate,
- high moisture content,
- low permeability (porosity), and
- high initial compressive stress.

The mechanisms proposed to explain the explosive spalling of rock can be divided into three categories: differential thermal expansion, steam pressure and external compressive stress (Hettema, 1996). In addition, the fires can generally be grouped into two types: small and localized fire, and large and widespread fire (Hajpál, 2002).

In order to consider the effect of different fire types, site conditions and rock types on rock spalling, Luleå University of Technology (Zhang et al., 2010, 2011) has conducted a series of uniformly and locally heated tests on oven-dried and water stored igneous and metamorphic rock (granite, gabbro and schist) blocks heated by standard/hydrocarbon fire curves. The high temperature effect on spalling was also investigated by heating rock cores in an oven. The tests results showed that spalling does not occur for all rock types under slow and homogeneous temperature changes (heating rate less than 1.5°C/min) but appears under fire heating. Granite is more prone to explosive spalling than schist and gabbro during fire, especially when the rock block is water saturated. For granite, thermal spalling due to fire is controlled not only by thermal stress but also by steam pressure. The layers of the schist expand at different rates, therefore they debond during fire. Although there is thermal cracking at macroscopic scale, the gabbro shows only limited spalling on the heated surface during fire. Based on a comparison between locally and uniformly heated rock blocks, it was found that rock spalling is less intense and less extensive under locally heated conditions. Since only a small part of the surface is heated with the torch, heat can leave the block through the other block surfaces. Furthermore, the thermal properties under elevated temperatures and thermo-mechanical properties after heating for these three rocks have also been tested.

In summary, the study at LTU (Zhang et al., 2010, 2011), financially supported by Banverket, Vattenfall and SKB, was a first step towards understanding the behaviour of different rock types exposed to fire. But, some of the factors that promote the tendency of rock to spall during a tunnel fire, for example, heating rate, external compressive stress and the effect of rock support have not been investigated. The inherent mechanism on thermal spalling is still not fully understood due to the complexity of the problem and the prediction of fire-induced spalling in a real tunnel is impossible. Furthermore, some interesting questions were also raised in the previous study and need to be answered in order to give more rational design for future tunnel safety.

1.3 Objectives

Therefore, the objectives of the proposed research project are to:

- further investigate experimentally the conditions under which thermal spalling occurs and determine the mechanism causing rock spalling observed in laboratory experiments,
- determine the type and extension of damage around rock tunnels caused by fire of a certain “size”,
- determine the remedial measures required in order to make the tunnel safe and usable again

1.4 Methodology

The project first focused on further investigations of spalling conditions by laboratory tests. Second, in order to assess the relationship between rock type (lithology) and the tendency to spall, microscopic observation was used as an important tool to provide understanding of the relation between microscopic changes and the macroscopic response of rocks after heating. This was done by mapping of micro-scale properties and recording and evaluating of acoustic emissions. Finally, the development of numerical analysis software made it possible to simulate complex loading conditions such as heat-induced response of rock. Numerical models both at microscopic and macroscopic levels were established by using a geomechanical code, UDEC. Both models were calibrated using the results from model tunnel tests carried out in this project. Based on numerical modelling, the mechanism causing thermal spalling and thermal fracturing observed in laboratory experiments was investigated. A numerical modelling technique which can be used to determine the type and extension of damage around rock tunnels caused by fire of a certain size was developed.

The reported project includes:

- literature study and overview,
- laboratory core and block-based tests,
- numerical analyses of rock block tests, and
- development of design recommendations.

2 HEATING OF CORE-BASED SPECIMENS

2.1 Tested rock types

Three rock types namely gabbro, granite and schist (Figure 1), derived from within Sweden and Finland, were tested and analysed in this study. The general descriptions of the rocks are outlined followed by their respective mineral compositions presented in Table 1.

The Kuru granite is a grey, fine to medium grained rock with a massive structure and comprised mainly of quartz, feldspar (alkaki feldspar > plagioclase) and biotite The gabbro is a massive, dark grey medium grained rock. It is evenly grained and comprised mainly of plagioclase, pyroxene, olivine and biotite. The schist is a light grey, quartz-rich, fine grained rock, exhibiting strong foliation. It comprises mainly quartz, biotite and a minor amount of feldspar. The foliation texture is made up of alternating mica-rich and quartz-rich bands/layers. The thickness of the layers ranges from 1 to 10 mm.

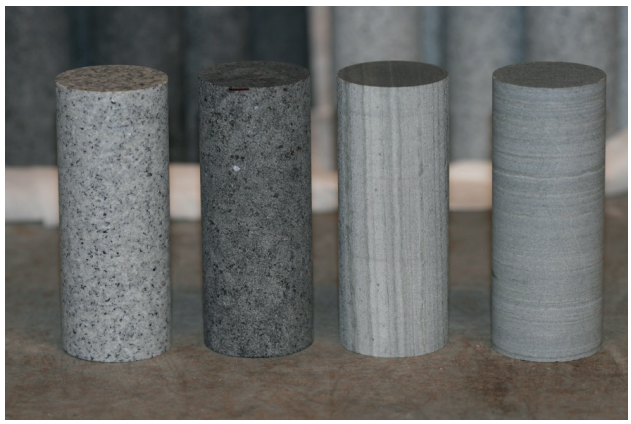

Figure 1 Rock cores of granite, gabbro and schist cored parallel to and perpendicular to foliation.

Table 1 Mineral composition of the rock material tested

	Mineral composition (vol. %)		
Mineral	Gabbro	Granite	Schist
Feldspar	55.8	59.4	6.1
Quartz	-	32	57.0
Pyroxene	27.6	-	–
Olivine	8.1	-	–
Mica	5.5	7.2	*36.9
Opaque minerals	3.0	1.4	–

*Amount of mica+other phases

The experimental procedure consisted of three parts; (i) thermal treatment (ii) mechanical tests and (iii) micro-crack and mineralogical mapping. Core-based cylindrical rock samples of the three rock types: granite, gabbro and schist were extracted from large cubic rock blocks

with dimensions 60 cm x 60 cm x 30 cm. The average diametre of the core samples was 44 mm. The uniaxial compression and Brazilian tests were conducted on both heat treated and unheated samples. After thermal treatment, thin sections were prepared from specimens of both the unheated and the heat treated rock samples for microscopic investigations. The objective was to investigate the effect of heat on the mechanical and physical properties of the rocks. The testing outline is depicted in Figure 2. The samples were divided into two testing schemes to establish and compare the effects of heating on saturated and unsaturated rock samples. The two schemes are referred to as Schemes 1 and 2, which are described below.

Scheme 1: Dry-Heat-Load – The rock samples were subjected to heat treatment in their dry state followed by mechanical tests as well as thin section preparations for microscopic investigations, after they were allowed to be gradually cooled down to room temperature.

Scheme 2: Saturate-Heat-Load – The rock samples were saturated prior to being subjected to heat treatment. The samples were saturated for 48 hours in water in a pressurized saturation chamber which ensures maximum saturation.

Because of its foliated nature, two sets of test samples, parallel to and perpendicular to the foliation planes were prepared for schist. The total number of specimens prepared, according to the thermal treatment schemes and the mechanical test types is summarized in Table 2. More details can be found in Saiang (2011).

The thermal treatment in this study was in principal a conditioning process where the rock samples were heated up to the desired temperature level, in this case: 400°C, 750°C and 1100°C. After heating they were allowed to cool gradually to room temperature before either mechanical tests were performed or thin section specimens were obtained for microscopic investigations. It was observed from a previous study by Larsson, (2006) on granite rock specimens that notable changes in the physical properties of the rock occurred as a result of heating. Beyond 1000°C some samples completely disintegrated and became unfit for further testing. Hence, 1100°C was deemed to be a sufficient maximum thermal treatment temperature in order to study the mechanical properties as well as mineral assemblage of the rock types when subjected to heat. A heating or cooling rate above 2°C /min introduces micro-cracks into the sample during heating and cooling (Simmons and Cooper, 1978). Considering this we have attempted in all our heat treatment to keep the heating and cooling rates of the rock samples below 2°C /min. The average heating rate was kept in the range of 0.8 °C /min to 1.5°C /min. With these heating rates the desired maximum temperatures were achieved within 12 hours for 400°C, 24 hours for 750°C and at most 36 hours for 1100°C. Once the desired temperature level was reached it was maintained at that level for about 1 hour before the furnace was turned off to allow the samples to cool down to room temperature. A continuous monitoring was required during each heating test. After heating, the hot rock samples were allowed to cool down gradually to room temperature and then transported directly for mechanical tests as well as further preparation for microscopic investigations. The very low heating and cooling rates used for the heat treatments possess the setback that the tests (heat treatment) are time consuming. Another setback encountered during heating is the fact that the schist rock samples tend to part along the foliation planes when they are heated making them unsuitable for mechanical loading.

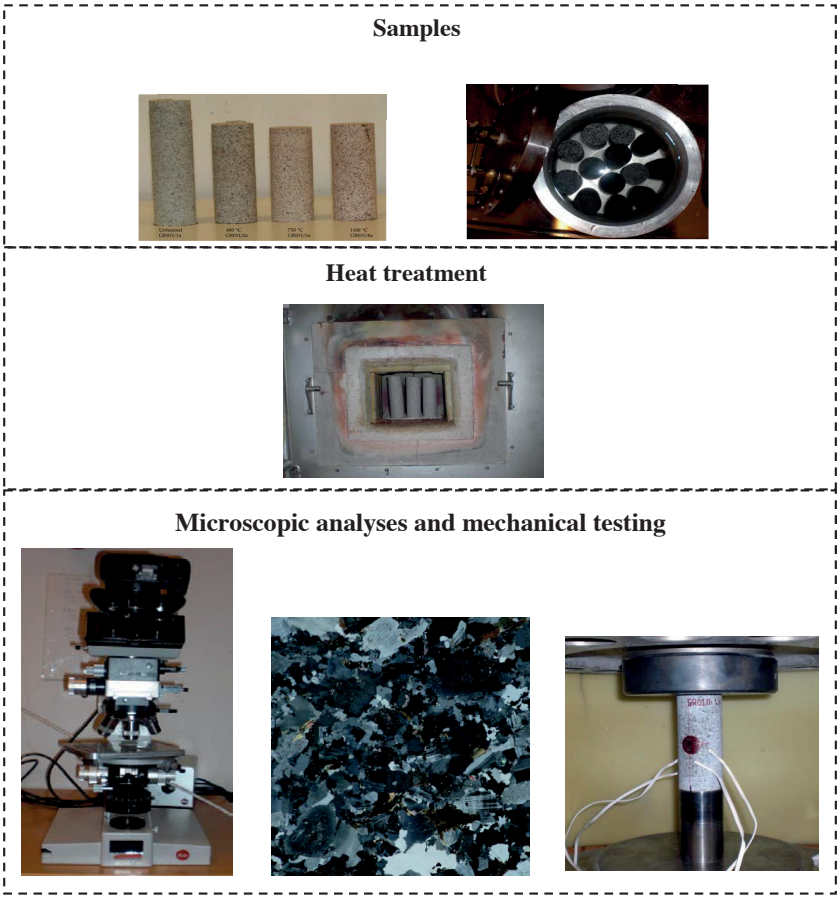

Figure 2 Schematic diagram of the methodology used in this study.

Table 2 Number of samples prepared according to test type and heat treatment temperature (°C).

Rock type	Heat treatment (°C)															
	UCS Test Samples				Brazilian Test Samples				Thin Section Samples				XRD Samples			
	0[β]	400	750	1100	0[β]	400	750	1100	0[β]	400	750	1100	0[β]	400	750	1100
Scheme 1:																
Gabbro	4	4	4	4	4	4	4	4	4	4	4	4	4	4	4	4
Granite	4	4	4	4	4	4	4	4	4	4	4	4	4	4	4	4
Schist-parallel[†]	4	4	4	4	4	4	4	4	4	4	4	4	4	4	4	4
Schist-perpendicular[Ψ]	4	4	4	4	4	4	4	4	4	4	4	4	4	4	4	4
Scheme 2																
Gabbro	4	4	4	4	4	4	4	4	–	–	–	–	–	–	–	–
Granite	4	4	4	4	4	4	4	4	–	–	–	–	–	–	–	–
Schist-parallel[†]	4	4	4	4	4	4	4	4	–	–	–	–	–	–	–	–
Schist-perpendicular[Ψ]	4	4	4	4	4	4	4	4	–	–	–	–	–	–	–	–
Sub-total	32	32	32	32	32	32	32	32	16	16	16	16	16	16	16	16
Total	**128**				**128**				**64**				**64**			

[β] Heat temperature of 0°C means that the sample is to be tested without any heat treatment, i.e. unheated.
[†] Schist samples with foliation plane parallel to the longitudinal axis
[Ψ] Schist samples with foliation plane perpendicular to the longitudinal axis

2.2 Mechanical properties of heated specimens

The compression tests were conducted using an Instron servo controlled 4.5 MN hydraulic testing machine (see Figure 3) which was equipped with Dartec electronic system for control and data acquisition. Each sample was loaded at a displacement rate of 5 µm/s. Two pairs of strain gauges were placed diametrically in the middle of the samples on identically opposite sides to measure the axial and diametrical strains (see Figure 3).

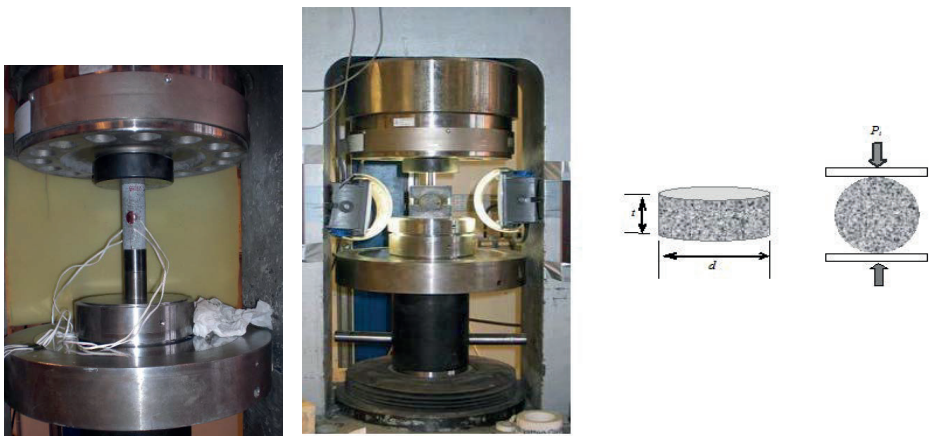

(a) (b)

Figure 3 The stiff 4.5 MN Instron compression testing machine used for (a) the UCS-tests and (b) the Brazilian tests.

In order to observe the behaviour of the mechanical properties, the interpolated averages of these parameters were obtained using the scientific software OriginPro (Originlab, 2002). Interpolated and weighted averages were calculated for the untreated sample parameters as well as for those heated up to 400°C, 750°C and 1100°C, respectively. The determined parameters for each rock type are presented in Table 3 - Table 5.

Table 3 Interpolated average values of the mechanical parameters of gabbro

Temperature (°C)	UCS (MPa)	Tensile Strength (MPa)	Young's Modulus (GPa)	Poisson's ratio	Peak axial strain (%)	Peak radial strain (%)
25†	194.3	21.1	91.9	0.26	0.22	-0.06
400	250.6	17.8	86.0	0.33	0.30	-0.11
750	201.1	10.2	50.2	0.42	0.53	-0.25
1100	88.0	4.1	18.1	0.85	0.77	-0.54

†Room temperature, which is the condition for the unheated rock specimens.

Table 4 Interpolated average values of the mechanical parameters of granite

Temperature (°C)	UCS (MPa)	Tensile Strength (MPa)	Young's Modulus (GPa)	Poisson's ratio	Peak axial strain (%)	Peak radial strain (%)
25†	231.3	16.7	65.4	0.27	0.38	-0.13
400	245.6	12.5	62.0	0.34	0.50	-0.17
750	123.4	3.4	26.7	0.52	1.11	-0.25
1100	13.9	0.8	2.3	0.94	1.71	-0.51

†Room temperature, which is the condition for the unheated rock specimens.

Table 5 Interpolated average values of the mechanical parameters of schist

Temperature (°C)	UCS (MPa)	Tensile Strength (MPa)	Young's Modulus (GPa)	Poisson's ratio	Peak axial strain (%)	Peak radial strain (%)
25†	254.0	30.1	63.3	0.26	0.50	-0.15
400	297.0	32.7	67.3	0.22	0.58	-0.10
750	229.3	23.1	34.7	0.18	1.64	-0.10
1100	74.8	6.6	9.8	0.44	2.0	-0.80

†Room temperature, which is the condition for the untreated rock specimens.

Figure 4 shows the uniaxial compressive strengths of untreated gabbro, granite and schist rock samples as well as that of rock samples that had been thermally treated at 400, 750 and 1100°C. For gabbro and schist, an obvious increase in the compressive strengths is seen for the samples that had been subjected to 400°C. A 20% increase in strength is observed for gabbro thermally treated at 400°C while for the schist loaded up to the same temperature level a 14% increase in compressive strength is observed. Granite samples thermally loaded to 400°C shows only a slight increase (6%) in compressive strength. As for the rock samples thermally treated at 400°C, gabbro shows a slightly higher compressive strength (3%) compared to the untreated samples while decrease in compressive strength is observed for granite and schist samples heated up to 750°C. The schist samples showed only a slight decrease (9 %) compared to untreated samples while a significant decrease (59 %) in compressive strength is observed for granite samples loaded up to 750°C. The sharp decrease of the compressive strength of granite persists with the increase of the thermal treatment temperature. The granite samples loaded up to 1100°C show almost a total loss of compressive strength (96% decrease) compared to the untreated granite samples. Schist samples loaded up to 1100°C show 71 % decrease in compressive strength while 55% decrease is observed for gabbro samples loaded up to 1100°C.

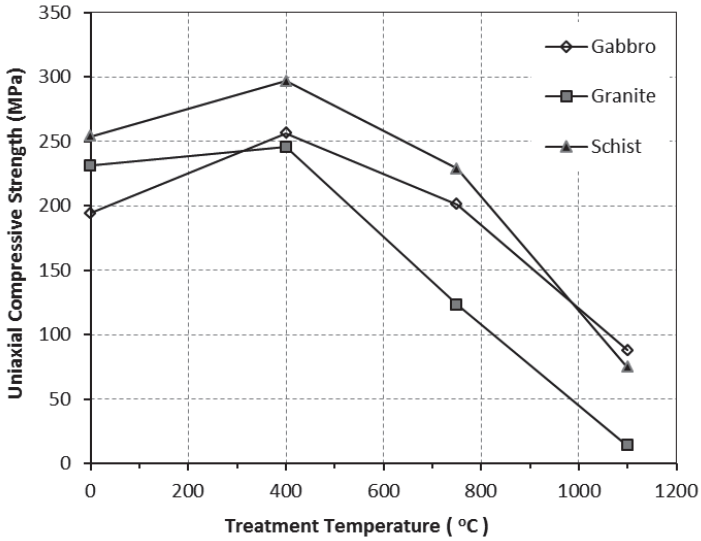

Figure 4 Uniaxial compressive strength (UCS) of gabbro, granite and schist at different thermal treatment temperature levels.

The trend of the Young's modulus was similar for the gabbro and the granite samples heated up to 400°C, 750°C and 1100°C (Figure 5). For gabbro and granite heated up to 400°C only a slight decrease is observed in the Young's modulus of both rock types, compared to the samples heated up to 750°C which show a more significant decrease. Young's modulus of gabbro and granite heated up to 400°C decreased by 6% and 5%, respectively. Granite and gabbro samples heated up to 750°C and 1100°C show more significant decrease in the Young's modulus. Schist samples heated up to 400°C show an opposite elastic behaviour to gabbro and granite. An increase of 6% in the Young's modulus is observed for the schist samples heated up to 400°C compared to the untreated schist samples. For the schist samples heated up to 750°C and 1100°C a reduction of Young's modulus is seen which was also observed in gabbro and granite heated up to the same temperature levels.

The maximum axial strain at failure for all three rock types was seen to increase with the increase of the thermal treatment temperatures (Figure 6). A constant increase in the maximum axial strain is observed for gabbro, granite and schist samples loaded to 400°C. Only gabbro continues to exhibit constant increase in the maximum axial strain after the 400°C thermal treatment temperature level. A significant increase in the axial strain at failure is observed for granite and schist samples loaded to 750°C and 1100°C. As for the maximum lateral strain at failure, only slight increases are observed for gabbro and granite samples loaded to 400°C and 750°C. For the schist samples loaded to 400°C and 750°C on the other hand, the maximum lateral strain is seen to decrease. For the rock samples loaded to 1100°C a significant increase in the maximum lateral strain at failure is observed in the schist samples. Notable increases in the maximum lateral strain at failure are observed for gabbro and granite samples thermally treated at 1100°C.

Figure 7 shows the strengths of gabbro, granite and schist thermally treated at different nominal temperatures as well as that of untreated rock samples. For gabbro and granite, a

constant decrease in tensile strength is observed for samples loaded up to 400°C. An obvious increase in tensile strength on the other hand was observed for schist samples loaded to 400°C. A decrease in tensile strength is observed for all three rock types for the rock samples loaded up to 750°C. Granite and schist show a sharper decrease in tensile strength for this treatment temperature level compared to the samples loaded up to 400°C while a constant decrease in tensile strength is observed for gabbro samples loaded up to the same temperature level. The sharp decrease in tensile strength persisted in schist samples loaded to 1100°C. For granite and gabbro samples loaded to 1100°C, a more even decrease is observed with granite samples loaded to 1100°C having almost no tensile strength.

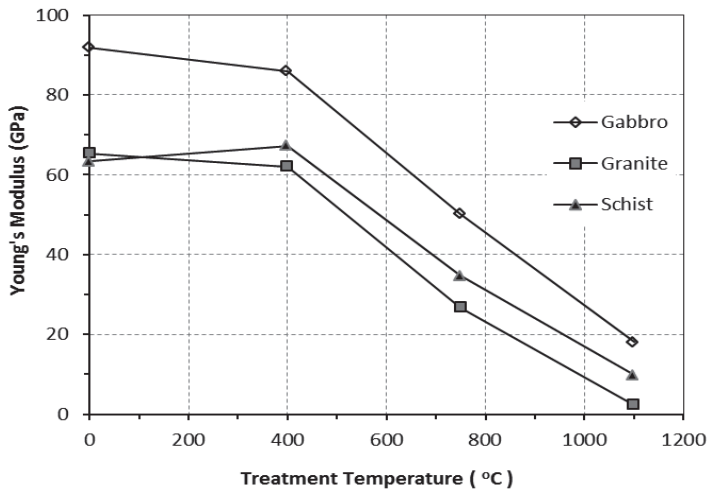

(a)

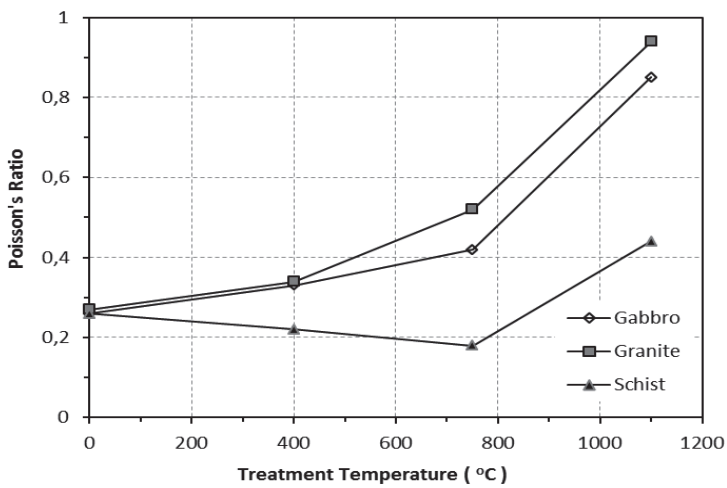

(b)

Figure 5 (a) Young's modulus of gabbro, granite and schist at different treatment temperature levels (b) Poisson's ratio of gabbro, granite and schist at different treatment temperature levels.

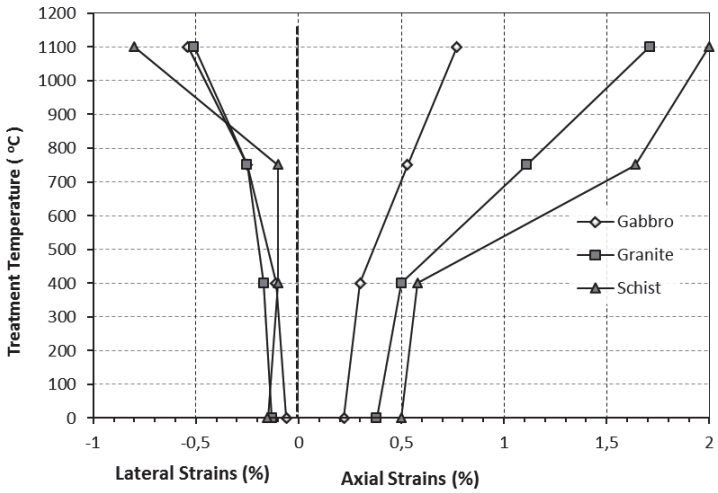

Figure 6 Maximum strains at failure during uniaxial compression tests for untreated (0°C) and thermally loaded gabbro, granite and schist samples.

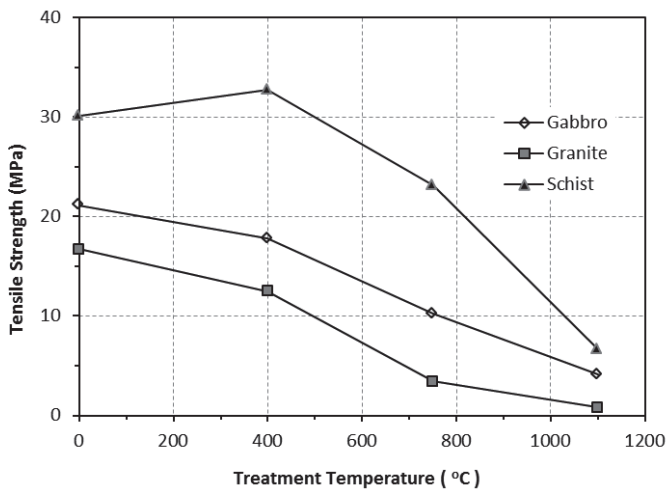

Figure 7 Tensile strength of gabbro, granite and schist at different treatment temperature levels.

2.3 Mineralogical changes due to heating

Subsequent to the thermal treatments thin sections of the thermally treated rock samples as well as untreated rock samples were made for microscopic investigation. The mineralogical analysis involved determining the chemical and mineral composition of each of the rock types subjected to 400°C, 750°C and 1100°C as well as for untreated rock samples. As shown in Figure 8, the thin section specimens were extracted from the mid-section of the rock samples.

This was particularly important for the heat treated rock samples in order to avoid biased results. Since it was observed that there was minimal difference between the mechanical properties as well as the mineralogical properties of the rocks in Schemes 1 and 2, from the mechanical tests and mineralogical analyses it was deemed sufficient to prepare samples for Scheme 1 only for further microscopic investigations.

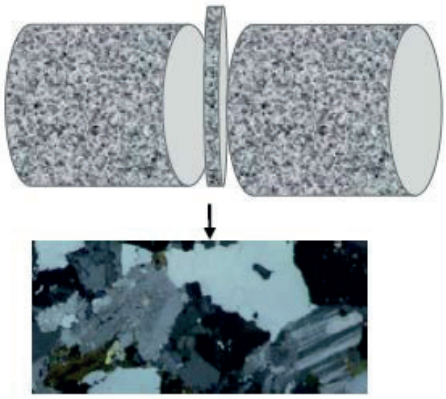

Figure 8 Illustration of how the thin section specimen was obtained from rock samples

Polarizing Microscopy and Scanning Electron Microscopy combined with Energy Dispersive Spectroscopy (SEM/EDS method) as well as petrographic image analysis were employed to perform the mineral composition analysis. Identification of the main minerals and determination of the mineral composition were carried out using polarizing microscopy combined with petrographic image analysis while SEM/EDS method was employed with particular attention on identification of the fine grained minerals and mineral phases which could not be adequately identified using polarising microscopy. SEM/EDS was also used to determine the chemical composition of the minerals and other phases.

The petrographic analysis was performed using a LEICA DMLP polarizing microscope combined with an Olympus digital camera. SEM/EDS analysis was performed using a Cambridge Cam Scan S4 instrument, with an energy dispersive analytical system (Oxford Instruments LINK ISIS 300) under a beam current 3 nA, and a 20 kV accelerating voltage. SPI Supplies 53 Minerals Standard Set #02753-AB was used for a routine quantitative calibration.

Petrographic image analysis technique which consists of manual image pre-processing, digital image analysis and data evaluation allows for digital analysis and quantification of the mineral content and other rock features such as grain shape, grain size as well as analysis of micro-cracks. Image pre-processing involves capturing of the image by means of digital photography in an optical microscope, identification of the measured objects, i.e. petrographic type of fragments, and image modification using graphic software (Corel Draw v. 12.0 or Photoshop). The image modification is a crucial point in the image pre-processing because the software used (SIGMASCAN Pro by Jandel Scientific) requires a binary image in which the object is differentiated from the background based on the intensity of a grey scale. This means that the object can be made either “lighter” or “darker” than the background. In the

preparatory stage, it is also important to add an identifier to each of the objects to indicate its petrographic nature. This identification is necessary for multiphase materials. Analysis of multiphase materials requires measurement of the appropriate number of objects, which ranges from 300 to 500 per sample. Using SIGMASCAN Pro software, the image measurement is performed by a feature-specific approach (i.e. fill measurement). In practice, the objects are measured separately. After the measurement, each object is filled with a contrast colour to avoid multiple analyses of an already-measured grain. Finally, the data obtained are analysed using a statistical software. The schematic diagram in Figure 9 illustrates the steps involved.

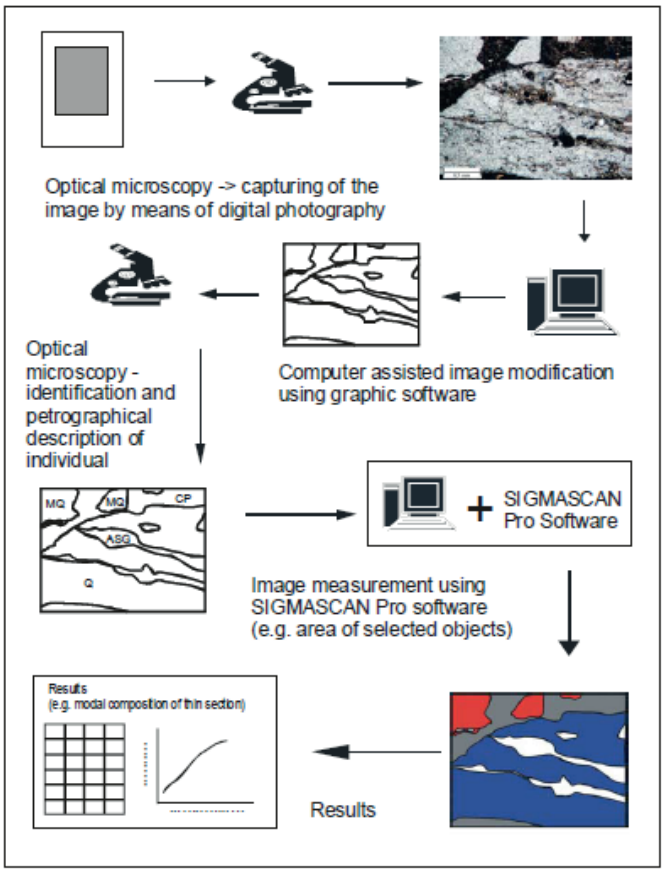

Figure 9 Image processing of thin sections (Lukschova, 2008).

Significant changes were noted in the physical properties of the rock samples as a result of the thermal treatments. Colour change of the rock samples resulting from the thermal treatment was observed for all three rock types, gabbro, granite and schist. As seen in Figure 10 the colour change of the rock samples became prevalent with the increase of thermal treatment temperatures. The rock samples thermally treated at 400 °C showed only a subtle change in colour while the colour change of the rock samples subjected to thermal treatments at 750 and 1100 °C were more apparent. Beside the colour change thermally treated rock samples

became very friable and showed greater tendency to crumble. This physical change also was more apparent with the increase of the thermal treatment temperatures and was more obvious for granite and schist than for gabbro. Schist samples also experienced de-bonding and parting along the foliation plane.

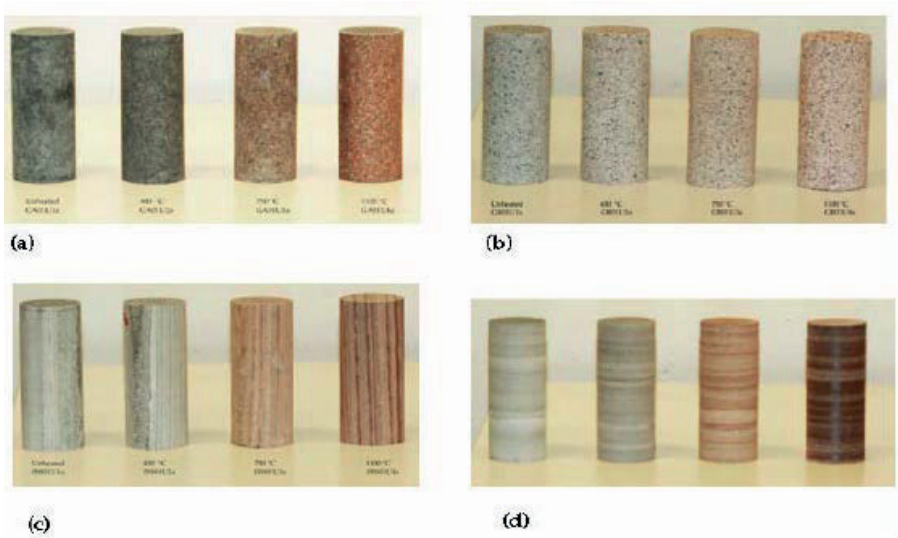

Figure 10 Test samples (a) Gabbro (b) Granite (c) Schist (parallel) (d) Schist (perpendicular). Samples from each rock type presented in the order of the lowest to the highest heat treatment temperature level from left to right, unheated, 400°C, 750°C, 1100°C.

The petrographic analysis showed notable changes in the mineral compositions for all the three rock types as a result of the thermal treatments. Presented in Table 6 andTable 9 are the mineral composition of granite, gabbro and schist in their untreated state as well as after being subjected to thermal treatment at 400°C, 750°C and 1100 °C. A group of mineral phases defined generally as opaque minerals was observed mostly in thermally treated rock samples. The amount of these opaque minerals is seen to increase with the increase of the thermal treatment temperatures, see Table 8. These are referred to as other phases (OP) in Table 6 and Table 8 and increase in amount with the increase in thermal treatment temperature levels. Figure 11 shows the above mentioned other phases (OP) observed in thermally treated rock specimens under the polarizing microscope. Closer investigation employing SEM-EDS method, as shown in Figure 12, indicated that these opaque minerals were composed mainly of oxides (ilmenite, magnetite, cuprite) and Fe-Ti-Mn (or Mg)-rich phases that were mostly mixed with mafic minerals such as pyroxene and biotite and correspond by their chemical composition to solid solution that could not be defined or classified into any particular mineral group.

Table 6 Mineral composition of gabbro with respect to the different heat treatment levels.

Minerals	Minerals in vol. %			
	Unheated	400°C	750°C	1100°C
Plagioclase	55.8	59.4	57.8	56.4
Pyroxene	27.6	27.2	26.8	21.8
Olivine	8.1	4.9	0.0	0.0*
Biotite	5.5	2.4	0.0	0.0*
Other phases	3.0	6.1	15.4	21.8
Total	100.0	100.0	100.0	100.0

*Minerals present but could not be positively identified for modal quantification

Table 7 Mineral composition of granite with respect to the different heat treatment levels.

Minerals	Mineral amount in vol. %			
	Unheated	400 °C	750°C	1100 °C
Feldspars	59.4	58.5	58.6	57.9
Quartz	31.9	32.7	32.4	32.4
Biotite	7.3	4.6	0.0*	0.0*
Other phases	1.4	4.2	9.0	9.7
Total	100.0	100.0	100.0	100.0

*Minerals present but could not be positively identified for modal quantification

Table 8 Mineral composition of schist with respect to the different heat treatment levels.

Minerals	Mineral amount in vol. %			
	Unheated	400°C	750°C	1100°C
Quartz	57.0	56.4	55.7	54.7
Feldspars	6.1	0.0*	0.0*	0.0*
Mica+ Other phases	36.9	43.6	44.3	45.3
Total	100.0	100.0	100.0	100.0

*Minerals present but could not be positively identified for modal quantification

Table 9 Changes in the amount of opaque minerals (other phases) with increasing heat treatment temperature magnitude.

Rock Type	Opaque minerals in vol. %			
	Non heated	400°C	750°C	1100°C
Gabbro	2.3	2.3	5.7	29.2
Granite	0.6	0.6	2.6	8.0

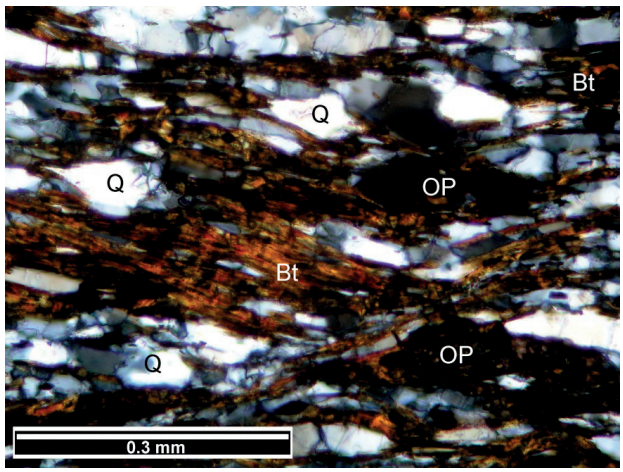

(a)

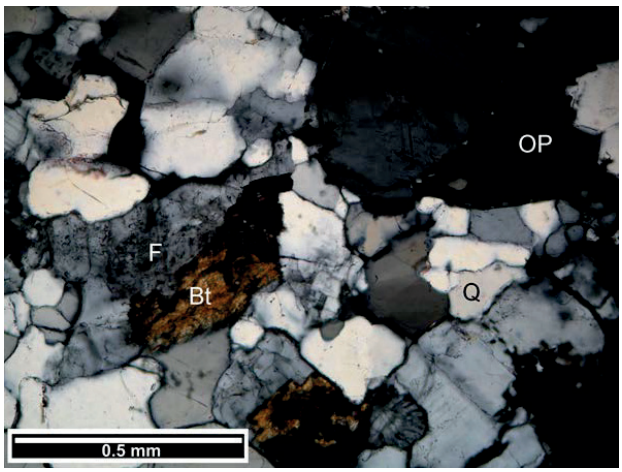

(b)

Figure 11 Other phases (OP) observed in thermally treated rock specimens by Polarising microscope, XP: (a) Schist at 1100°C. (b) Granite at 1100°C. Other minerals present, F-feldspar, Bt-biotite, Q-quartz.

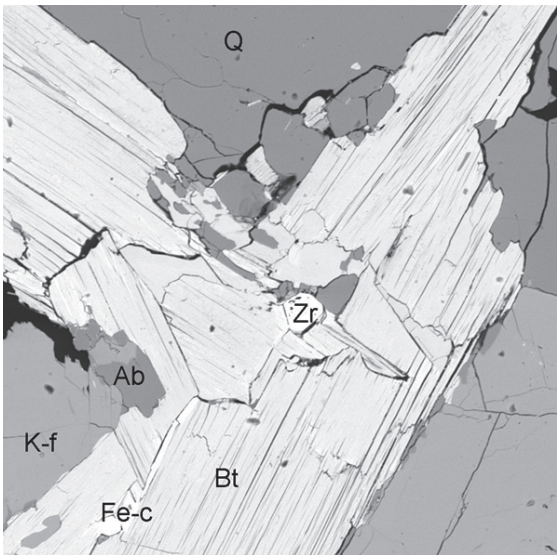

(a)

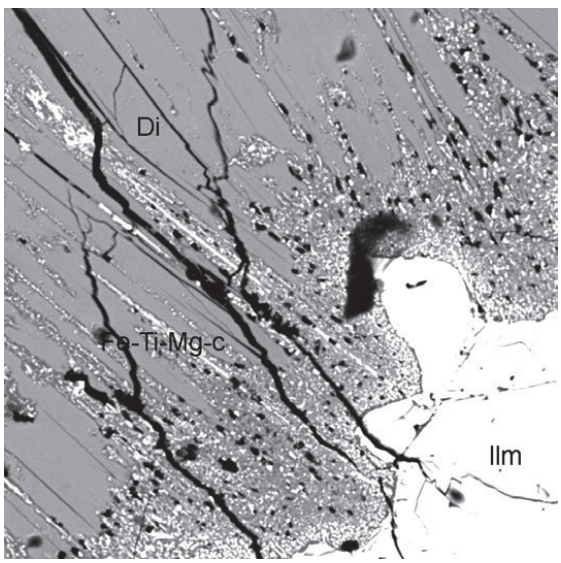

(b)

Figure 12 Opaque minerals and other phases positively identified using SEM-EDS method in thermally treated rock specimens (BSE image): (a) granite at 750°C (b). gabbro at 1100°C. Q-quartz, F-feldspar, Bt-biotite, Zr-zircon, Ilm-ilmenite, Ab-albite, Fe-c-iron-rich phase, Di-diopside, Fe-Ti-Mn-c- Fe-Ti-Mn-rich phase.

Some minerals though present could not be positively identified, for instance, biotite and olivine in gabbro, biotite in granite and feldspar in schist particularly for rock samples subjected to thermal treatment at 750°C and 1100°C. The optical properties of these minerals had been altered due to the thermal treatments which made positive identification of some grains under the polarizing microscope impossible. It was therefore deemed not possible to

accurately determine their composition using polarizing microscopy. The presence of these minerals was revealed by the chemical composition analysis obtained using the SEM/EDS method. The results of these analyses with respect to the thermal treatment temperatures are presented in Tables 10-12 for thermally treated gabbro, granite and schist respectively. The influence of heat on the mineral composition of gabbro, granite and the schist subjected to thermal treatment at 400°C, 750°C, 1100°C temperature levels were analysed using statistics and the results presented according to the rock type in the form of tables and bar charts.

Table 10 Chemical composition of minerals of thermally treated granite with respect to thermal treatment temperature

Minerals	Thermal treatment temperature	Chemical composition of minerals in wt % recalculated to sum of 100 %																					
		Na_2O	MgO	Al_2O_3	SiO_2	P_2O_5	SO_3	K_2O	CaO	TiO_2	VO	F	ZrO_2	CO_2	BaO	CrO	MnO	FeO	LaO_3	ThO_2	Ce_2O_3	Nd_2O_3	Total
Quartz	400 °C	0	0	0	100	0	0	0	0	0	0	0	0	0	0	0	0	0	0	0	0	0	100
	750 °C	0	0	0	100	0	0	0	0	0	0	0	0	0	0	0	0	0	0	0	0	0	100
	1100 °C	0	0	0	100	0	0	0	0	0	0	0	0	0	0	0	0	0	0	0	0	0	100
Plagioclase	400 °C	9.8	0	21.8	65.6	0	0	0	2.3	0	0	0	0	0	0	0	0	0	0	0	0	0	100
	750 °C	8.5	0	24	62.3	0	0	0	5.2	0	0	0	0	0	0	0	0	0	0	0	0	0	100
	1100 °C	9.7	0	22.3	64.4	0	0	0.4	3.2	0	0	0	0	0	0	0	0	0	0	0	0	0	100
K-feldspar	400 °C	0.6	0	18.6	64.4	0	0	16.2	0	0	0	0	0	0	0.2	0	0	0	0	0	0	0	100
	750 °C	0.6	0	18.6	64.7	0	0	16.1	0	0	0	0	0	0	0	0	0	0	0	0	0	0	100
	1100°C	1.2	0	18.9	64.8	0	0	15.1	0	0	0	0	0	0	0	0	0	0	0	0	0	0	100
K (Na)-feldspar	400 °C	-	-	-	-	-	-	-	-	-	-	-	-	-	-	-	-	-	-	-	-	-	
	750 °C	5.6		19.1	66.5			8.8	0	0	0	0	0	0	0	0	0	0	0	0	0	0	100
	1100 °C	3.9		21.5	62.6			10.6	0.4	0	0	0	0	0	0	0	0	0	0	0	0	0	100
Biotite	400	0.1	4.2	17.4	35.2	0	0	9.8	0	2.5	-	0	0	0	0	-	0,5	30.3	0	0	0	0	100
	750 °C	0.1	4.0	17.7	36.5	0	0	9.7	0	2.3	0	-	0	-	-	-	0.6	29.1	0	0	0	-	100
	1100 °C	2.7	3.6	17.2	36.4	0	0	4.6	1.4	2.7	0	0	0	-	-	-	0.4	31.0	0	0	0	0	100
Appatite	400 °C	0	0	0	0,3	43,1	0	0	56,6	0	0	0	0	0	0	0	0	0	0	0	0	0	100
	750 °C	-	-	-	-	-	-	-	-	-	-	-	-	-	-	-	-	-	-	-	-	-	-
	1100 °C	0.1	0.4	0.2	0.8	42.9	0	0.1	55.5	0	0	0	0	0	0	0	0	0	0	0	0	0	100
Fluorite	400 °C	0						0.4	73.7			40.6											114
	750 °C	-	-	-	-	-	-	-	-	-	-	-	-	-	-	-	-	-	-	-	-	-	-
	1100 °C	-	-	-	-	-		-	-	-	-	-	-	-	-	-	-	-	-	-	-	-	-
Calcite	400 °C	0.0	0.0	0.0	0.0	0.0	0.0	0.0	0.0	1.4	0.7	0	0	0	0	0.0	0.0	97.4	0.0		0.0	0.0	100
	750 °C	0	0.3	0.8	0.0	0.0	0.0	0.0	0.0	0.2	0.0	0	0	0	0	0.0	0.0	98.0	0.0		0.0	0.0	100
	1100 °C	-	-	-	-	-	-	-	-	-	-	-	-	-	-	-	-	-	-	-	-	-	-
Ilmenite	400 °C	0	0	0	0	0	0	0	0	51.1	0	0	0	0.4	0	0	7,3	41.2	0	0	0	0	100
	750 °C	0	0	0	0	0	0	0	0	51.0	0	0	0	0	0	0	7.4	51.0	0	0	0	0	100
	1100 °C	0	0	1,6	1,2	0,2	0	0	0	46.2				0	0	0	5.8	45.0	0	0	0	0	100
Zircon	400 °C	0	0	0	31.3	0	0	0	4.9	0	0	0	62.5	0	0	0	0	0	0	0	0	0	100
	750 °C	0	0	1.3	38.8	0	0	0	0	0	0	0	37.2	0	0	0	0.1	0.8	2.2	3.9	6.9	0	100
	1100 °C	0	0	0.4	36.5	0	0	0	0	0	0	0	49.5	0	0	0	0	0	2.2	3.9	6.9	0	100
Epidote	400 °C	-	-	-	-	-	-	-	-	-	-	-	-	-	-	-	-	-	-	-	-	-	-
	750 °C	-	-	-	-	-	-	-	-	-	-	-	-	-	-	-	-	-	-	-	-	-	-
	1100 °C	1.7	2.2	21.3	39	0	0	2.6	11.4	1.0	0	0	0	0	0	0	0	20.3	0	0	0	0	100
Ti-Fe-Mn phase	400 °C	-	-	-	-	-	-	-	-	-	-	-	-	-	-	-	-	-	-	-	-	-	-
	750 °C	0	0	0	0	0	0	0	0	59.4	0	0	0	0	0	0	7.8	32.8	0	0	0	0	100
	1100 °C	0	0	0	0	0	0	0	0	59.4	0	0	0	0	0	0	7.8	32.8	0	0	0	0	100

Table 11 Chemical composition of minerals of thermally treated gabbro with respect to thermal treatment temperature

Minerals	Thermal treatment temperature	Chemical composition of minerals in wt % recalculated to sum of 100 %																
		Na_2O	MgO	Al_3O_2	SiO_2	P_2O_5	SO_3	K_2O	CaO	TiO_2	VO	CrO	MnO	FeO	$La2O_3$	Ce_2O_3	Nd_2O_3	Total
Plagioclase	400 °C	4.9	0.0	29.6	53.8	0.0	0.0	0.0	11.7	0.0	0.0	0.0	0.0	0.0	0.0	0.0	0.0	100
	750 °C	5.3	0.1	29.1	53.9	0.0	0.0	0.1	11,2	0.0	0.0	0.0	0.0	0.3	0.0	0.0	0.0	100
	1100 °C	4.8	0	29.9	53.1	0.0	0.0	0,0	10.3	0.0	0.0	0.0	0.0	0.4	0.0	0.0	0.0	98.5
Biotite	400 °C	2.8	2.9	21.2	39.8	0.0	0.0	5.3	1.0	0.0	0.0	0.0	0.3	24.6	0.0	0.0	0.0	100
	750 °C	0.1	16.0	15.5	38.7	0.0	0.0	10.0	0.0	4.2	0.0	0.0	0.0	15.4	0.0	0.0	0.0	100
	1100 °C	0.6	14.9	14.8	43.0	0.0	0.1	9.7	0.7	3.9	0.0	0.0	0.0	12.3	0.0	0.0	0.0	100
Enstatite-ortthoferrosilite group	400 °C	0.0	20.7	1.0	52.0	0.0	0.0	0.0	0.9	0.2	0.0	0.0	0.2	25	0.0	0.0	0.0	100
	750 °C	0.0	21.9	3.0	50.8	0.0	0.0	0.3	1.0	0.4	0.0	0.0	0.4	22.5	0.0	0.0	0.0	100.3
	1100 °C	0.0	19.3	1.6	52.7	0.0	0.0	0.4	0.7	0.6	0.0	0.0	0.5	24.2	0.0	0.0	0.0	100
Olivine	400 °C	0.4	19.8	2.4	40.9	0	0	0.4	3.1	0	0	0	0.2	32.8	0	0	0	100
	750 °C	0.2	15.2	2.8	51.0	0	0	0.2	3.1	0	0	0	0.3	27.0	0.0	0.0	0.0	100
	1100 °C	-	-	-	-	-	-	-	-	-	-	-	-	-	-	-	-	-
Hornblende	400	0	12.6	6.7	47.3	0	0	0.3	2.9	0	0	0	0.3	29.9	0	0	0	100
	750	-	-	-	-	-	-	-	-	-	-	-	-	-	-	-	-	-
	1100	-	-	-	-	-	-	-	-	-	-	-	-	-	-	-	-	-
Appatite	400 °C	0.0	0.0	0.0	0.0	43.5	0.0	0.0	56.5	0.0	0.0	0.0	0.0	0.0	0.0	0.0	0.0	100
	750 °C	0.0	0.0	0.0	0.0	0.4	42.5	0.0	0.0	56.1	0.0	0.0	0.0	1.1	0.0	0.0	0.0	100.1
	1100 °C	0.0	0.0	0.0	0.0	0.0	0.0	0.0	0.0	0.0	0.0	0.0	0.0	0.0	0.0	0.0	0.0	0.0
Diopside	400 °C	0.4	13.9	2.3	51.8	0	0	0	21.9	0.7	0.1	0	0	8.9	0	0	0	100
	750 °C	0.4	13.8	1.0	52.3	0	0	0	22.6	0.1	0	0	10.2	9.7	0	0	0	100
	1100 °C	0.3	13.8	1.5	52.6	0	0	0	22.1	0	0	0	0.2	0	0	0	0	100
Magnetite	400 °C	0.0	0.0	0.0	0.0	0.0	0.0	0.0	0.0	1.4	0.7	0.0	0.0	97.4	0.0	0.0	0.0	100
	750 °C	0	0.3	0.8	0.0	0.0	0.0	0.0	0.0	0.2	0.0	0.0	0.0	98.0	0.0	0.0	0.0	100
	1100 °C	-	-	-	-	-	-	-	-	-	-	-	-	-	-	-	-	-
Ilmenite	400 °C	0	0.6	0.3	0	0	0	0	0	50.8	0	0	0.5	47.8	0	0	0	100
	750 °C	0	0.3	0	0	0	0	0	0	26.9	0	0	47.7	24.5	0	0	0	100
	1100 °C	0	0.8	0	0	0	0	0	0	56.3	0	0	0.4	45.5	0	0	0	100
K-feldspar	400 °C	-	-	-	-	-	-	-	-	-	-	-	-	-	-	-	-	-
	750 °C	1,9	0	18.7	64.2	0	0	15.2	0	0	0	0	0	0	0	0	0	100
	1100 °C	-	-	-	-	-	-	-	-	-	-	-	-	-	-	-	-	-
Pyrite	400 °C	-	-	-	-	-	-	-	-	-	-	-	-	-	-	--	-	-
	750 °C	0	0	0	0	0	54.0	0	0	0	0	0	0	40.8	0	5.2	0	100
	1100 °C	-	-	-	-	-	-	-	-	-	-	-	-	-	-	-	-	-

Table 12 Chemical composition of minerals of thermally treated schist with respect to thermal treatment temperature

Minerals	Thermal treatment temperature	Chemical composition of minerals in wt % recalculated to sum of 100 %																
		Na_2O	MgO	Al_3O_2	SiO_2	P_2O_5	ZrO_2	K_2O	CaO	TiO_2	CuO	BaO	MnO	FeO	$La2O_3$	Ce_2O_3	Nd_2O_3	Total
Albite	400 °C	11.3	0.0	20.0	68.4	0.0	-	0.0	0.3	0.0	0.0	0.0	0.0	0.0	0.0	0.0	0.0	100
	750 °C	11.4	0.0	19.6	68.6	0.0	-	0.0	0.2	0.0	0.0	0.0	0.0	0.3	0.0	0.0	0.0	100
	1100 °C	-	-	-	-	-	-	-	-	-	-	-	-	-	-	-	-	-
Biotite3	400 °C	0.1	9.3	20.1	47.6	-	-	10.2	0.8	1.0	-	-	0.3	11.0	-	-	-	100.4
	750 °C	0.2	3.0	25.8	50.1	-	-	-	-	0.6	0.4	-	-	7.8	-	-	-	100
	1100 °C	3.6	3.4	27.5	51.9	-	-	5.6	0.7	0.3	-	-	-	7.0	-	-	-	100
Epidote	400 °C			23.3	38.3			0.1	24.3				0.4	13.5	-	-	-	100
	750 °C	-	-	22.8	38.2	-	-	-	22.8	-	-	-	0.5	14.2	-	-	-	100
	1100 °C	0.5	-	26.1	38.7	-	-	0.1	-	-	-	-	0.1	11.5	-	-	-	100
K-feldsar	400 °C	0.3	-	17.2	67.0			15.4		0.1	-	-	-	-	-	-	-	100
	750 °C	0.2	-	18.4	65.5			16.5				0.2	-	-	-	-	-	100
	1100 °C	-	-	-	-	-	-	-	-	-	-	-	-	-	-	-	-	-
Magnetite	400	-	-	-	-	-	-	-	-	6.2	-	-	-	93.8	-	-	-	100
	750		0.5	-	0.3	-	-	-	-	4.6	-	-	-	94.9	-	-	-	100
	1100	-	-	-	-	-	-	-	0.3	4.6	-	-	-	95.1	-	-	-	100
Sphene	400 °C	-	-	2.0	31.0	-	-	-	29.1	37.1	-	-	-	0.8	-	-	-	100
	750 °C	-	-	1.6	30.9	-	-	0.1	28.8	37.0	-	-	-	1.6	-	-	-	100
	1100 °C	-	-	1.5	30.9	-	-	-	29.4	37.5	-	-	-	1.1	-	-	-	100
Zircon	400 °C	-	-	-	32.4		65.2	-	-	-	-	-	-	-	2.4	-	-	100
	750 °C	-	-	-	-	-	-	-	-	-	-	-	-	-	-	-	-	-
	1100 °C	-	-	-	-	-	-	-	-	-	-	-	-	-	-	-	-	-
Cuprite	400 °C	-	-	-	-	-	-	-	-	-	-	-	-	-	-	-	-	-
	750 °C	-	-	0.5	0.8	-	-	0.1	-	-	97.5	-	-	1.1	-	-	-	100
	1100 °C	1.0	-	-	-	-	-	-	-	-	95.1	-	-	2.8	-	-	-	100

2.3.1 GABBRO

The main mineralogical changes observed in gabbro as a result of being subjected to temperature increase include the alterations of mica, olivine and pyroxene. Figure 13 shows the alteration of pyroxene due to thermal treatment in gabbro that had been subjected to thermal treatment at 750°C. Olivine and mica minerals significantly decreased in amount after thermal treatment at 400°C, Table 13. After thermal treatment at 750°C, mica and olivine mineral could not be positively identified in gabbro using the polarizing microscope due to the alterations in their optical properties resulting from the thermal treatments. This is also the case after thermal treatment at 1100°C. Unlike the olivine and mica, pyroxene did not show any significant change at 400°C temperature level but showed a marked decrease as a result of thermal treatment at 1100°C. Parallel to the changes in the content of olivine, mica and pyroxene a step-wise increase was observed in the content of other phases. These mineral phases defined as other phases could not be positively identified using the polarizing microscope. They were, therefore, loosely classified as opaque minerals. Using the SEM/EDS method, the other phases were identified to compose mainly of ilmenite and magnetite. The increase in content of these other phases suggest that these mineral phases are a result of the transformation and/or phase transition of the olivine and mica which after heat treatment at 750°C appeared to be altered and diminished in quantity in thermally treated gabbro. A Fe-Ti-Mg rich phase is identified in gabbro after heat treatment at 1100°C. This Fe-Ti-Mg rich phase was observed to originate from pyroxene close to the ilmentie and/or magnetite phases.

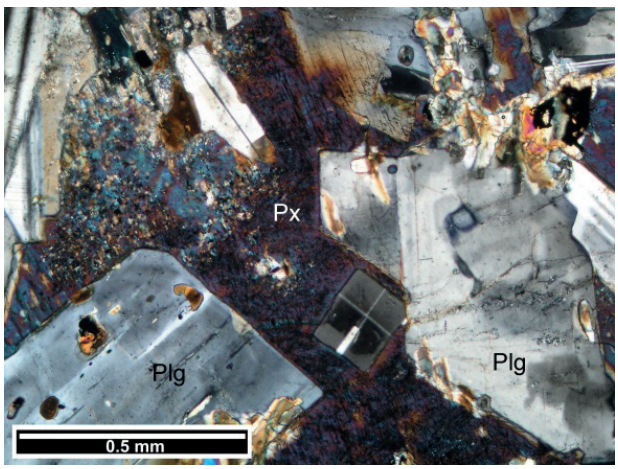

Figure 13 Pyroxene alteration observed in gabbro sample thermally treated at 750°C. Polarising microscope, XP.

Table 13 Mineral composition of gabbro showing the changes in the amount of the constituent minerals with respects to different heat treatment temperatures levels.

Minerals	Mineral content in vol. % at different temperature levels				Comments	
	Unheated	400°C	750°C	1100°C		
Feldspar	55.8	59.4	57.8	56.4	400°C	3.5 vol. %
					750°C	2.0 vol. %
					1100°C	0.6 vol. %
Pyroxene	27.6	27.2	26.8	21.8	400°C	-0.5 vol. %
					750°C	-0.9 vol. %
					1100°C	-5.8 vol. %
Olivine	8.1	4.9	0*	0*	400°C	-3.2 vol. %.
					750°C	-8.1 vol. %
					1100°C	No olivine observed
Mica	5.5	2.4	0*	0*	400°C	-3.1 vol.%
					750°C	-5.5 vol. %
					1100°C	No mica observed
Other phases (Opaque mineral)	3.0	6.1	15.4	21.8	400°C	3.2 vol. %
					750°C	12.43 vol. %.
					1100°C	18.8 vol. %

*Mineral present but could not be positively identified using the polarizing microscope.

2.3.2 GRANITE

The granite is in its unheated state composed mainly of feldspars (alkali feldspar > plagioclase), quartz and biotite. When subjected to thermal treatments the mineralogical changes in granite showed similar trends to that observed in gabbro with the marked changes being the alterations of the mica mineral. Fluorite and calcite were observed in accessory amounts in granite thermally treated at 400°C. Ti-Fe-Mg phase corresponding by its chemical composition to solid solution instead of mineral is observed in granite subjected to thermal treatment at 750°C. For granite heated to 1100°C, K feldspar and biotite which had minor amounts of Na_2O included are observed. Also allanite, epidote and aluminocerrite were observed in accessory amounts only in granite thermally treated at 1100°C. The content of feldspar and quartz, the dominant minerals, showed only slight changes with the increase of the treatment temperature and without any regular pattern so it was not obvious if these changes were directly related to temperature increase. The mica mineral on the other hand showed significant decrease in amount as a result of the temperature increase indicating the decrease as a direct influence of the increase in treatment temperatures. As observed in gabbro there was a marked decrease in the amount of mica at the 400°C temperature level. After treatment at 750°C and 1100°C the mica minerals were strongly altered and as such could not be positively identified. Similar to the gabbro observations there was a parallel step-wise increase in the content of the other phases with the increasing temperature levels. The other phases present in granite composed mainly of apatite, zircon, ilmenite Fe-oxide (magnetite), fluorite, calcite and Ti-Fe-Mn- rich phase corresponding by their chemical composition to solid solution that could not be classified into any particular mineral group.

Table 14 shows the mineralogical composition of granite and the changes in the mineral content of the constituting minerals which occurred as a result of the rock samples being subjected to heat treatment at different temperature levels. This table shows that, the content

of the dominant minerals feldspar and quartz slightly varied with the increase of the thermal treatment temperatures. The marked mineralogical changes observed in granite with response to the increase in the heat treatment temperature level include the decrease in the amount of the mica mineral.

Table 14 Mineral composition of granite showing the changes in the amount of the constituent minerals with respects to different heat treatment temperatures levels.

Minerals	Mineral content in vol. % at different temperature levels				Comments	
	Unheated	400°C	750°C	1100°C		
Feldspar	59.4	58.5	58.6	57.9	400°C	-1.0 vol. %
					750°C	-0.2 vol. %
					1100°C	-1.5 vol. %
Quartz	31.9	32.7	32.4	32.4	400°C	0.8 vol. %
					750°C	0.4 vol. %
					1100°C	-1.5 vol. %
Mica	7.2	4.6	0	0	400°C	-2.6 vol. %.
					750°C	-7.2 vol. %
					1100°C	No mica observed
Other phases (Opaque mineral)	3.0	6.1	15.4	21.8	400°C	2.7 vol. %
					750°C	7.6 vol. %.
					1100°C	8.3 vol. %

2.3.3 SCHIST

The mineral composition of the schist and the mineralogical changes it had undergone with the increase of the thermal treatment temperature levels is presented in Table 15. All constituting minerals showed only slight variations in their mineral content with the increase of the thermal treatment temperatures. The marked mineralogical changes were observed in feldspar at 400°C where the feldspar minerals observed in the mineral at its unheated (original) state is transformed to an extent that at 400°C, 750°C and 1100°C they were not observed anymore.

Table 15 Mineral composition of schist showing the changes in the amount of the constituent minerals with respects to different heat treatment temperatures levels.

Minerals	Mineral content in vol. % at different temperature levels				Comments	
	Unheated	400°C	750°C	1100°C		
Feldspar	6.1				400°C	-6.1 vol. %
Quartz	57.0	56.4	55.7	54.7	400°C	Negligible change
					750°C	Negligible change
					1100°C	-2.3 vol. %
Mica + Other phases	36.9	43.6	44.3	45.3	400°C	6.7 vol. %.
					750°C	7.4 vol. %
					1100°C	8.3 vol. %

The mineralogical composition of gabbro, granite and schist in their unheated state, and after being subjected to the heat treatment at temperature levels of 400°C, 750°C and 1100°C are presented in Table 16.

Table 16 Mineralogical composition of gabbro, granite and schist in natural (untreated) state after being subjected to heat treatment at 400°C, 750°C and 1100°C temperature levels.

Mineral	Thermal treatment			
	Unheated	400°C	750°C	1100°C
Gabbro				
Feldspar	55.8	59.4	57.9	56.4
Pyroxene	27.6	27.2	26.7	21.8
Olivine	8.1	4.9	0	0
Mica	5.5	2.4	0	0
Other phases	3.0	6.1	15.4	21.8
Granite				
Feldspar	59.4	58.5	58.6	57.9
Quartz	31.9	32.7	32.4	32.4
Mica	7.3	4.6	-	-
Other phases	1.4	4.2	9.0	9.7
Schist				
Quartz	57.0	56.4	55.7	54.7
Feldspar	6.1	-	-	-
Mica+other phases	36.9	43.6	44.3	45.3

2.4 Micro-cracking induced by heating

The micro-crack analysis was performed in a similar manner as the mineral composition analyses. The specific length of micro-cracks was calculated as the length of the micro-cracks divided by area was analyzed in the thin sections. The measurement was based on the combination of polarising microscopy and petrographic image analysis. The measurement consisted of five different steps:

- **Image digitizing** refers to the step in which selected areas of the thin sections were photo documented.
- **Image acquisition** represents the step where a suitable area is selected. The size of the area is dependent on the grain size and the number of cracks in the thin section. 300 but preferentially 600 micro-cracks were analyzed per thin section.
- **Image pre-processing** includes a step in which images are graphically modified with the goal to increase the contrast between the micro-cracks and the background. The contrast and the brightness of the digital images were modified using Corel Photo Paint software.
- **Measurement** refers to the step where the image analyses software. SIGMASCAN Pro5, Jandel Scientific, USA was employed. The length of the micro-cracks and the dimensions of the selected areas were measured. The process of image analyses is semi-automatic. Thus the difference between the micro-cracks measured and their characterization was controlled by the operator.

- During data analysis, the length of micro-cracks was summed-up and divided by the total measured area. The specific length of the micro-cracks (in mm/mm^2) characterizes the degree of micro-cracking.

An evaluation of micro-crack distribution in the rock samples revealed changes concerning the degree of micro-cracking at different treatment temperature levels. The degree of micro-cracking is dependent on (1) type of mineral, (2) rock type and (3) the thermal treatment temperature. The micro-crack analyses performed included identifying the micro-crack types and calculating the specific length of the micro-cracks in the major minerals and in the rock specimen as a whole. The micro-cracks were divided into two main types, intra-crystalline and inter-crystalline micro-cracks, Figure 14. Presented in Table 17 is a subjective classification of the presence of the two types of micro-cracks in the untreated rock samples as well as rock samples subjected to thermal treatments at the different temperature levels for all three rock types studied. The specific length of the micro-cracks which characterizes the degree of micro-cracking is calculated as the total length of micro-cracks divided by the total area analysed in the thin section. It does not express the average value calculated from the specific length of micro-cracks of individual grains. The specific length of micro-cracks (SLM) is measured in individual grains as well as in the whole thin section. The micro-cracks present in the other phases (OP) were not analysed because the grain sizes of the other phases were below the resolution limit of the polarizing microscope. Identification of the micro-cracks was possible only using the SEM/EDS method. It was therefore impossible to quantify the micro-cracks in the other phases due to the very small grain size.

Table 17 Subjective classification of the presence of intracrystalline and intercrystalline micro-cracks.

Rock type	Unheated	400°C	750°C	1100°C
Gabbro				
Intercrystalline	na	rare	common	common
Intracrystalline	common	common	common	common
Granite				
Intercrystalline	na	rare	common	common
Intracrystalline	rare	common	common	common
Schist				
Intercrystalline	na	na	rare	common
Intracrystalline	rare	rare	common	common

na- not analysed

(a)

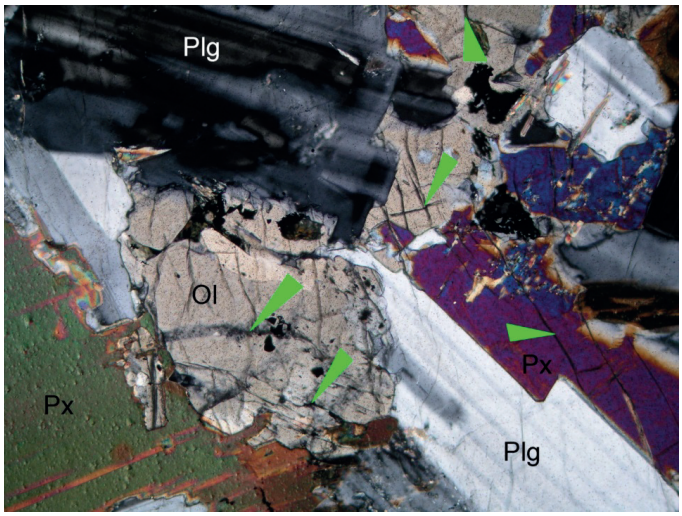

(b)

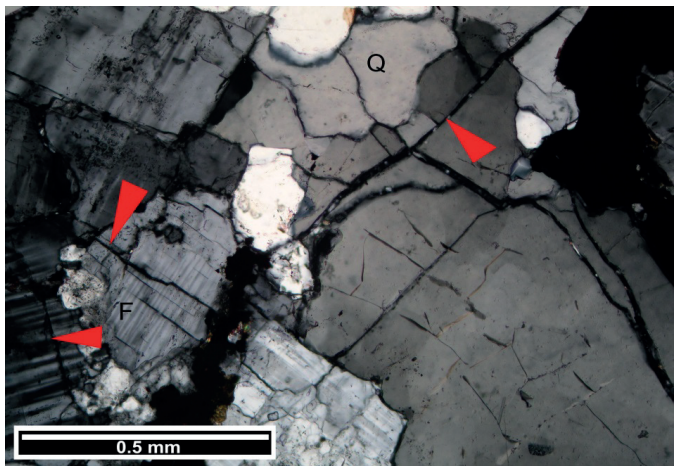

Figure 14 Micro-cracks observed in rock specimens. (a) Intracrystalline micro-cracks (indicated by green arrows) cutting olivine (Ol) pyroxene (Px) and plagioclase (Plg) observed in untreated gabbro sample. (b) Intercrystalline micro-cracks (indicated by red arrows) cutting alkali-feldspar (F) and quartz (Q) observed in granite sample thermally treated at 1100°C. Polarizing microscope, XP

2.4.1 GABBRO

The specific micro-crack lengths of gabbro depicting the degree of micro-cracking in untreated and thermally treated rock samples were analysed and the results are shown in Table 18. Micro-cracks exist in the untreated gabbro sample and with the increase of the thermal treatment temperatures the degree of micro-cracking in thermally treated gabbro samples was seen to increase. The distribution of micro-cracks in the minerals of gabbro, i.e. feldspar, olivine, mica and pyroxene were investigated separately for rock samples thermally treated at different temperature levels, (400°C, 750°C and 1100°C) as well as for the

untreated sample. The olivine grains have the highest degree of micro-cracking followed by pyroxene, feldspar and mica. The micro-crack distribution analysis was not performed for the other phases present because they were of a size far too small to be identified and analysed using the polarizing microscope (100 times magnification). To illustrate the micro-crack contribution from the constituent minerals the ratio of specific micro-crack lengths to the mineral content was plotted as shown in Figure 15. This plot shows that the olivine minerals had the highest micro-crack ratios, followed by pyroxene and mica, while feldspar, the dominant mineral in gabbro, has the least micro-crack ratio. A substantial increase in the degree of micro-cracking is observed in all of the constituting minerals with the increase of the thermal treatment temperatures. Only the feldspar and pyroxene minerals allowed the possibility of micro-crack analysis to be performed for all the temperature levels. It was not possible to determine the micro-crack distribution in olivine and mica in rock specimens of gabbro subjected to thermal treatments at 750°C and 1100°C since olivine and mica in these thermally treated specimens could not be positively identified using polarizing microscopy. The micro-crack ratio is calculated as the specific micro-crack length of the mineral divided by the volume percentage of the mineral.

Table 18 Specific length of the micro-cracks (in mm/mm^2) in gabbro

Minerals	Specific length of micro cracks (mm/mm^2)			
	Unheated	400 °C	750 °C	1100 °C
Plagioclase	8.7	14.4	21.9	22.4
Pyroxene	11.6	18.7	20.2	51.6
Olivine	25.5	32.6	-	-
Biotite	1.5	5.2	-	-
Other phases	NA	NA	NA	NA

N/A : Not analysed- micro-crack distribution analyses were not performed either because the minerals were not observed (using the polarizing microscope) in gabbro at these temperature levels or because the mineral phases could not be adequately identified using the polarizing microscope magnification used.

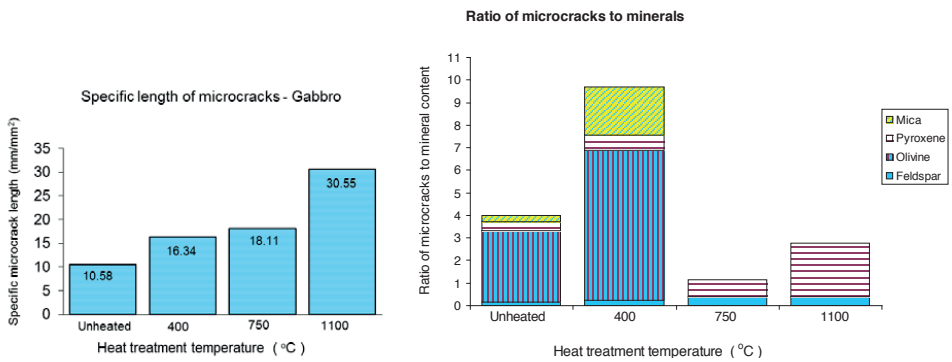

a) b)

Figure 15 a) Specific micro-crack length in gabbro samples after heat treatment at 400°C, 750°C and 1100°C and b) Ratio of specific micro-crack lengths to mineral content of the constituting minerals of gabbro after heat treatment at 400°C, 750°C and 1100°C.

2.4.2 GRANITE

The results of micro-crack distribution within the comprising minerals of the granite specimens are presented in Table 19. Figure 16 shows the distribution of micro-cracks in the granite rock specimen (thin section) as a whole for the untreated rock samples as well as for thermally treated rock samples. Feldspar and quartz, the dominant minerals in granite show similar patterns in the development and distribution of micro-cracks with the increasing temperature levels. Like gabbro, the micro-crack distribution pattern of the constituting minerals were investigated separately for the granite samples thermally treated at different temperature levels as well as for the untreated granite. Figure 14(b) shows the ratio of the micro-cracks to the amount of comprising minerals. Biotite (mica) mineral had the highest micro-crack ratio followed by feldspar and quartz for the untreated granite sample and for the granite thermally treated at 400°C.

Table 19 Specific length of micro-cracks in granite

Minerals	Specific length of micro craks (mm/mm^2)			
	Unheated	400°C	750°C	1100°C
Plagioclase	8.7	14.4	21.9	22.4
Pyroxene	11.6	18.7	20.2	51.6
Olivine	25.5	32.6	-	-
Biotite	1.5	5.2	-	-
Other phases	NA	NA	NA	NA

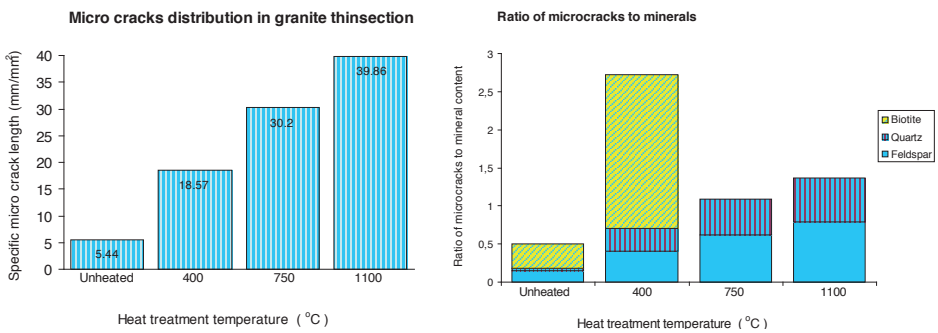

a) b)

Figure 16 a) Specific micro-crack length in granite after heat treatment at 400°C, 750°C and 1100°C and b) Ratio of specific micro-crack lengths to mineral grains of granite at different heat treatment temperatures.

2.4.3 SCHIST

Results of micro-crack analyses of schist samples subjected to thermal treatments at the different temperatures are presented in Table 20 and Figure 17. Micro-crack distributions of the constituting minerals were investigated as well as that of the rock sample as a whole. The micro-cracks analysis was not performed for the mineral phase defined as the other phases as the mineral grains of this phase were below the resolution limit of the polarizing microscope.

Table 20 Specific length of micro-cracks in schist

Minerals	Specific length of micro-cracks (mm/mm^2)			
	Unheated	400°C	750°C	1100°C
Quartz	0.0*	7.2	24.3	33.2
Feldspar	0.0*	-		
Biotite + other phases	0.0*	NA	NA	NA

*Amount of micro-cracks is below 0.01 mm/mm^2

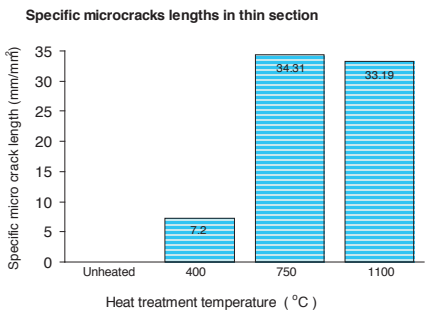

Figure 17 Specific micro-crack length in schist.

The micro-crack analyses of the three rock types after thermal treatments at the different temperature levels i.e., unheated, 400°C, 750°C and 1100°C are summarized and presented in Table 21, Figure 18 and Figure 19.

Table 21 Specific crack lengths measured under a polarizing microscope.

Mineral	Micro-crack distribution (mm/mm^2)			
	Unheated	400 °C	750 °C	1100 °C
Gabbro				
Feldspar	8.7	14.4	21.9	22.4
Pyroxene	11.6	18.7	26.7	51.6
Olivine	25.5	32.6	-	-
Mica	1.5	5.2	-	-
Other phases	N/A	N/A	N/A	N/A
Granite				
Feldspar	8.6	23.9	36.6	45.4
Quartz	1.2	9.5	15.12	18.72
Mica	1.5	5.2	-	-
Other phases	-	-	-	-
Schist				
Quartz	0*	7.2	24.3	33.2
Feldspar	0*	-	-	-
Mica+other phases	0*	-	-	-

*Amount of micro-cracks below 0.01 mm/mm^2 ; NA- Not analysed.

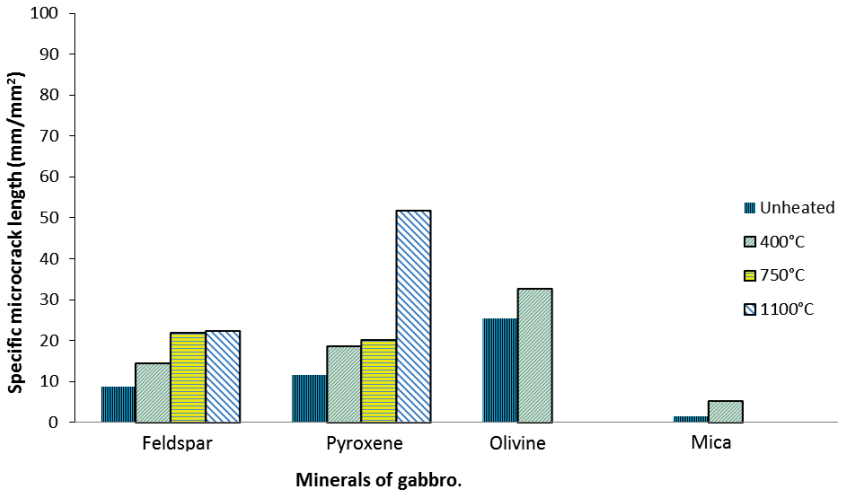

Figure 18 Summary of micro-crack distribution in the minerals of gabbro samples subjected to thermal treatments at the different temperature levels.

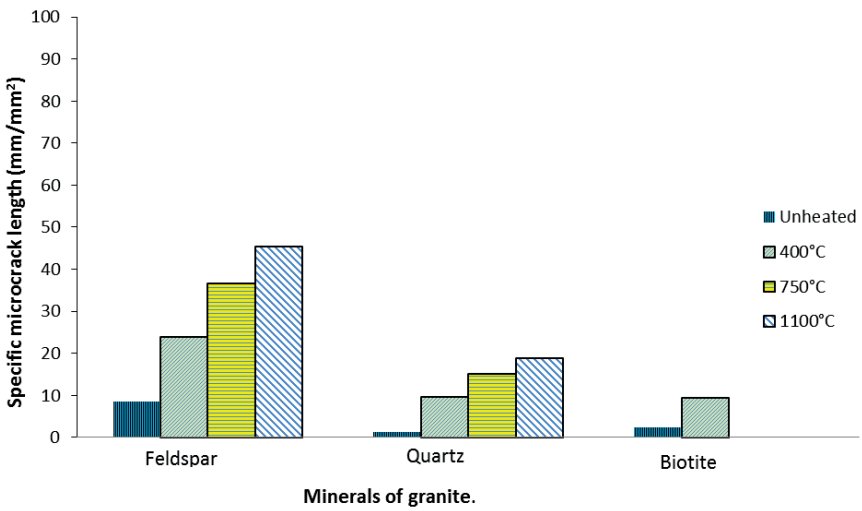

Figure 19 Summary of micro-crack distribution in the minerals of granite samples subjected to thermal treatments at the different temperature levels.

3 BLOCK TESTS

3.1 Rock blocks' preparation

The size of the granite, gabbro and schist blocks was 600 mm × 500 mm × 300 mm. To investigate the influence of water saturation on spalling, both oven-dried and water-stored rock blocks were prepared. The oven-dried rock blocks were dried in an oven using a very slow heating rate (increasing around 10ºC per hour) until 105ºC. The water-stored blocks were prepared by placing then in a container and storing them under water for 17, 85 and 180 days before being uniformly heated, locally heated and model tunnel tests respectively. The water content was measured indirectly by measuring the mass variation of a group of rock cores which had been stored under the same water condition as the rock blocks. In fact, the water content did not change with the stored time after 2 weeks due to the low porosity of rocks. The water content of the water stored rock blocks and porosity of rocks are listed in Table 22. All the tested rock blocks and their test conditions are listed in Table 23.

Table 22 Porosity of rocks and water content for water stored rock blocks.

Rock types	Gabbro	Granite	Schist
Porosity	0.42 %	0.61 %	0.40 %
Water content	0.07 %	0.20 %	0.14 %

Table 23 Rock types and their test conditions.

Test conditions			Gabbro	Granite	Schist
Uniformly heated tests	Oven-dried	With thermocouples	A4	G3	S3
	Water-stored	With thermocouples	A3	G2	S1
		Without thermocouples	A1	G1	S2
Locally heated tests	Oven-dried	With thermocouples	A7	G7	S7
	Water-stored	With thermocouples	A5	G4	S4
Model tunnel tests	Oven-dried	Without bi-axial stress		G8	
		Bi-axial stress	A8	G7	S7
	Water-stored	Bi-axial stress	A9	G9	S9

3.2 Fire curves

In recent years a great deal of research has taken place internationally to ascertain the types of fire which could occur in tunnel and underground spaces. This research has taken place in both real, disused tunnels and laboratory conditions. As a consequence of the data obtained from these tests, a series of temperature-time curves for the various exposures have been developed, see Figure 20 (Promat, 2014).

3.2.1 CELLULOSIC (ISO 834) CURVE

Standard fire tests to which specimens of constructions are subjected are based on the use of the Cellulosic temperature-time curve, as defined in various national standards, e.g. ISO 834, BS 476: part 20, DIN 4102, AS 1530 etc. Although there are other types of fire test curves e.g. BS 7436, the curve as detailed below for this exposure is the lowest one used in normal practice. This curve is based on the burning rate of the materials found in general building

materials and contents. The temperature development of the Cellulosic fire curve (ISO-834) is described by the following equation:

$T = 20 + 345\log(8t + 1)$ [°C],

where t is the heating time in minutes**.**

3.2.2 HYDROCARBON

Although the Cellulosic curve has been in use for many years, it soon became apparent that the burning rates for certain materials e.g. petrol gas, chemicals, were well in excess of the rate at which for instance, timber would burn. As such, there was a need for an alternative exposure for the purpose of carrying out tests on structures and materials used within the petrochemical industry, and thus the hydrocarbon curve was developed. The hydrocarbon curve is applicable where small petroleum fires might occur, i.e. car fuel tanks, petrol or oil tankers, certain chemical tankers etc. In fact, although the hydrocarbon curve is based on a standardised type of fire, there are numerous types of fire associated with petrochemical fuels. The temperature development of the Hydrocarbon (HC) fire curve is described by the following equation:

$T = 20 + 1080(1 - 0.325e^{-0.167t} - 0.675e^{-2.5t})$ [°C],

where t is the heating time in minutes.

3.2.3 RABT CURVE

The RABT curve was developed in Germany as a result of a series of test programs such as the Eureka project. In the RABT curve, the temperature rise is very rapid up to 1200°C within 5 minutes. The duration of the 1200°C exposure is shorter than other curves with the temperature drop off starting to occur after 30 minutes for car fires. The drop off for train fires only starts after 60 minutes. A 110 minutes cooling period is applied to both fire curves.

3.2.4 RWS (RIJKSWATERSTAAT) CURVE

The RWS curve was developed by the Rijkswaterstaat, Ministry of Transportation in the Netherlands. This curve is based on the assumption that in a worst case scenario, a 50 m^3 fuel, oil or petrol tanker fire with a fire load of 300 MW could occur, lasting up to 120 minutes. The RWS curve was based on the results of testing carried out by TNO in the Netherlands in 1979. In the present project the standard fire curve in accordance with EN 1363-1 and the HC curve in accordance with EN 1363-2 were used.

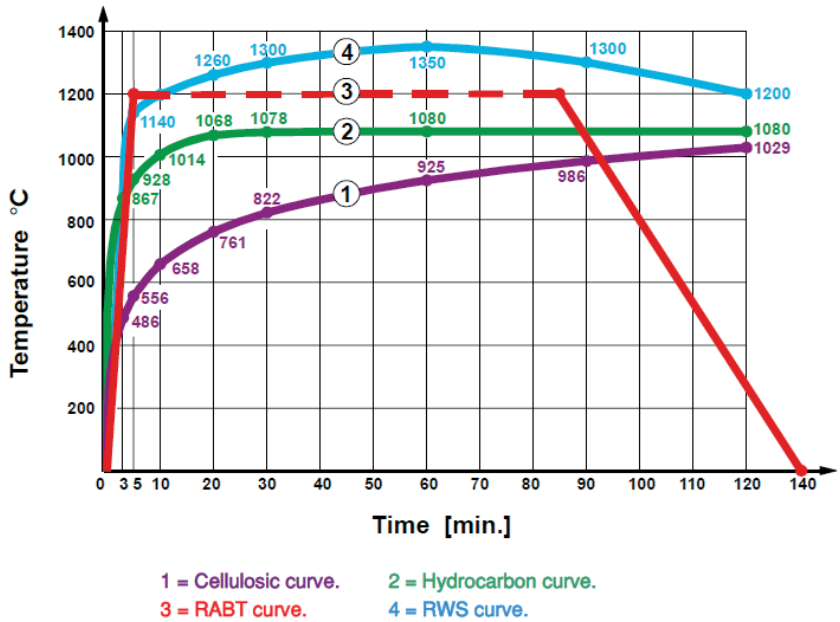

Figure 20 Different types of fire curves (Promat, 2014).

3.3 Uniform heating tests

A small furnace was used in the uniform heating test series conducted at SP Technical Research Institute of Sweden, Borås. The opening of the furnace, i.e. the fire exposed surface of the rock blocks, had the dimensions of 500 mm by 400 mm. The blocks were always placed horizontally on the top of the furnace and the fire exposure was always one-sided (600 mm by 500 mm). The furnace with a rock block is shown in Figure 21. The schematic diagram of the test set-up is shown in Figure 22.

The temperature in the furnace was controlled by a 1 mm shielded type K thermocouple. Although the gas temperatures during a fire were designed to follow the hydrocarbon (HC) temperature-time curve, see Figure 23, it was found impossible after several minutes heating due to inadequate heat input in the furnace. However, the rapid start in the HC curve was still achieved, which seems to be important when considering spalling. The temperature inside the tested rock blocks were also measured by type K thermocouples in four drilled holes. The drilled holes had an average diametre of 10.5 mm and they were drilled in a rhombic pattern (150×130 mm^2) around the centre of the block. The bottoms of the holes were at 20 mm, 40 mm, 80 mm, and 160 mm, respectively, from the heated surface. The holes were completely filled with fine quartz sand (with the average diametre of 0.2 mm).

The fire tests were run for 25 minutes except for two cases, and thereafter the burners were shut down. Hence the effect of the cooling phase, or fire-extinction were not examined. The heating duration was limited to 25 minutes because thermal spalling has been observed and reported within 25 minutes heating, e.g. Keski-Rahkonen et al. (1986), Smith and Pells (2008). Also, by using short heating duration damage to the furnace due to collapse of tested

rock blocks was prevented. The mass of spalling material inside the furnace due to fire exposure was weighed in order to make a rough quantification of the degree of spalling.

The initiation and propagation of surface fractures during and after the heating was recorded by a camera and a video camera. The acoustic emission system was used to monitor the process of fracturing and spalling inside the block. The AE sensors were installed on the surface opposite to the one exposed to heating, see Figure 21.

Figure 21 Rock block (granite) placed on the furnace.

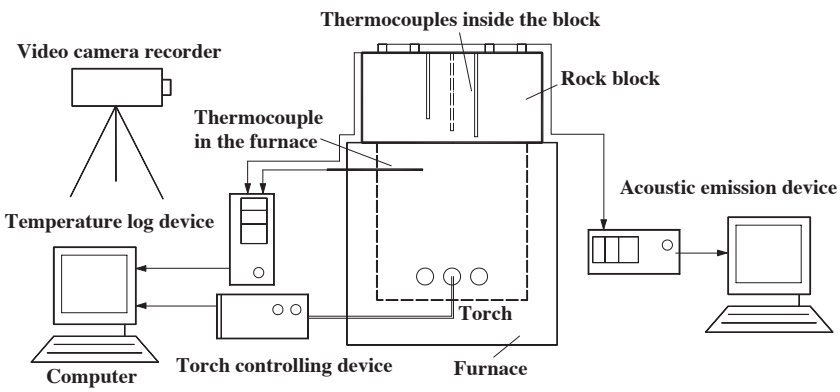

Figure 22 The schematic diagram of the set-up for the uniformly heating tests.

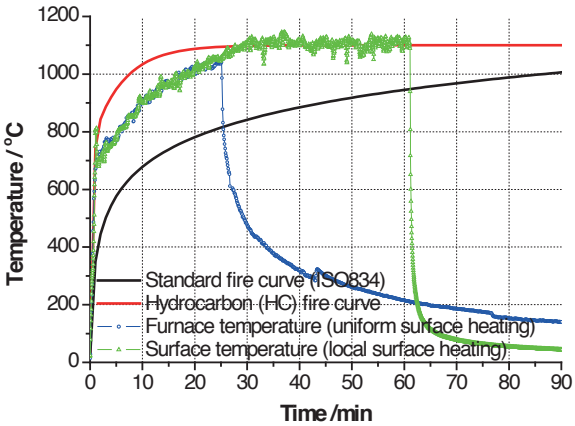

Figure 23 Comparison between the fire curves and the measured temperature-time curves.

3.4 Locally heating tests

The photograph of the test set-up for local surface heating test is presented in Figure 24. To control the temperature and make it follow the temperature-time curve used in uniform heating tests, a blow torch was fixed on a moving device. Therefore, the temperature on the heated surface could be adjusted in virtue of a type K thermometre with a diametre of 1.5 mm. The temperature-time curve achieved during operating of the blowtorch was approximated to the fire curve used in the furnace tests (see Figure 23). After it reached 1100 ºC, the temperature was kept consistent with the hydrocarbon fire curve (HC) for 60 minutes. The rock block was wrapped in rockwool to prevent heat exchange between the rock block and the surrounding environment. The temperature inside the tested rock blocks was measured in the same way as in the furnace test. An electronic balance with a piece of plate was placed below the block to measure the weight of spallation material.

The initiation and propagation of surface fractures during and after the heating were recorded by a camera and a video camera. The acoustic emission system was used to monitor the process of fracturing and spalling inside the block. The AE sensors were installed on the surface opposite to the one exposed to heating, see Figure 24.

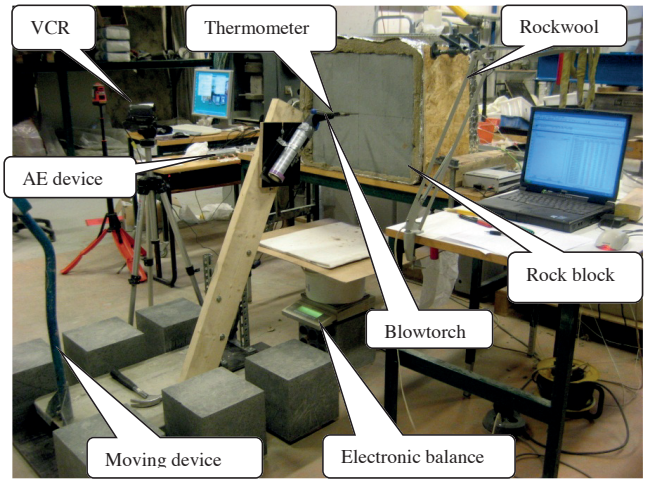

Figure 24 The photograph of the set-up for local heating tests (side view).

3.5 Model tunnel tests

In order to simulate a real tunnel boundary effect, a 75 mm borehole was drilled through the centre of the tested rock blocks to resemble a tunnel. The biaxial compressive load was supplied by two hydraulic jacks by means of the reaction force provided from a stiff frame with dimensions 1900 mm × 1900 mm × 300 mm. The load was applied on the surfaces of the blocks through a semi-circular hinge to keep the load normal to the block's surface. The designed load was 500 kN on four sides of the rock blocks. The test set-up is shown in Figure 25 (a).

The temperature around the opening boundary was measured by three AWG20 shielded type K thermocouples which were attached to the hole boundary at different distances from the front free surface of the block. The fire tests were designed to follow the hydrocarbon (HC) temperature-time curve. The burner was placed at a desirable location in order to reach the highest temperature. During testing, the real temperature-time curves inside the hole boundary were monitored with three thermocouples placed at 5, 10 and 15 cm from the front free surface and compared with the HC curve. To keep the monitored temperature the same as the HC curve, the release rate of propane was controlled manually during testing. It was found impossible to follow the HC curve after several minutes of heating due to incomplete combustion inside the hole boundary, but the rapid start in the HC curve was achieved, see Figure 26. The temperatures inside the tested rock blocks were also measured by eight type K thermocouples in three drilled holes. The holes had an average diametre of 10 mm and were drilled perpendicular to the hole axis at different distances from the external boundary of the block. The holes were completely filled with cement. The pattern of the installed thermocouples is shown in Figure 25 (b).

In the full scale test and small scale test, the spalling was observed after 20-25 minutes heating. To avoid collapse of the rock blocks into the oven, the heating duration in previous

studies at SP Technical Research Institute of Sweden was set to 25 minutes. Therefore, in order to compare spalling depth and other characteristics of the thermal behaviour of rocks, the heating duration in these tests was limited to 25 minutes as well. While conducting the tests a video camera recorded the initiation and propagation of the surface fractures. The acoustic emission (AE) system was used to provide real time evidence of crack initiation and spalling inside the block. The AE sensors were installed on the front and back surfaces of the blocks.

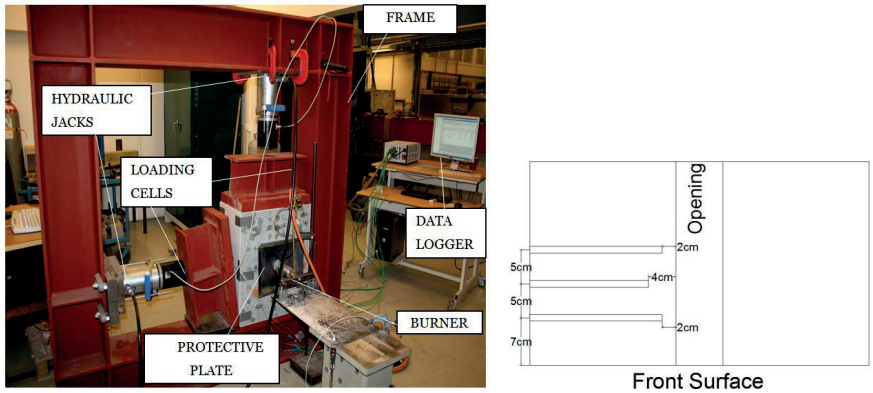

(a) Test set-up (b) Drilling pattern of thermocouple holes

Figure 25 Layout of test set-up and thermocouple holes.

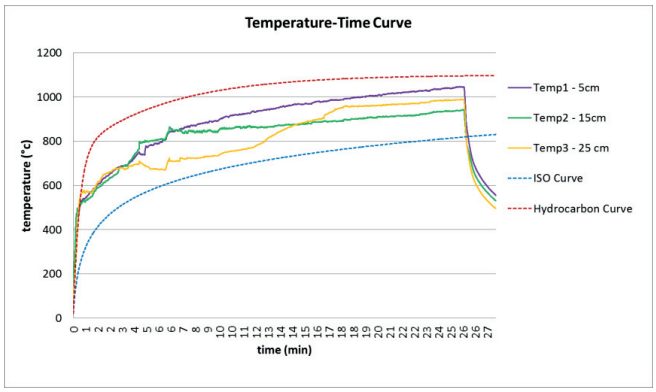

Figure 26 Comparison between the fire curves and the measured temperature-time curves at different locations on hole boundary of granite block (G9).

4 DAMAGE INDUCED BY THE BLOCK TESTS

4.1 Observations

4.1.1 UNIFORM HEATING TESTS

Granite block: The oven-dried granite block started to spall after about 8 minutes of heating and the spalling was accompanied with dull explosive sounds. Some flat chips of various sizes were produced. During heating, the thermal fractures appeared on the surrounding free surfaces of the blocks and propagated from the bottom (exposed to the fire) to the top surface. The maximum spalled piece of the spalling material in the furnace was around 40 mm wide and 3 mm thick. Spalling was more intensive for the water-stored granite block (G1) than for the oven-dried granite block (G3). The mass of the spalling material in the furnace and the spalling depth is presented in Table 24 and Table 25. The presented data indicates that the water-stored granite block presents more explosive spalling than the oven-dried block. Furthermore, to investigate the influence of heating duration, one water-stored block (G2) was heated only for 6.8 minutes, but there was still explosive spalling during the first several minutes. The mass of spalling material was also greater than that of the oven-dried block (G3), see Table 24.

Gabbro block: The thermal fractures also appeared on the surrounding free surfaces of the blocks and propagated from the bottom to the top surface for both oven-dried and water-stored gabbro blocks. Only small pieces flew off the fire-exposed surface regardless of whether the blocks were oven-dried or water stored. The mass of the spalling material is presented in Table 24. In order to investigate whether the explosive spalling would occur with increasing heating duration, one water-stored block (A3) was heated for about 90 minutes. The mass of the spalling material in this test was approximately two times that of the other water-stored block (heated only 25 minutes), the damage was still surface pitting rather than explosive spalling.

Schist block: Unlike granite and gabbro, there was obvious differential lateral expansion perpendicular to the heating direction for schist, which resulted in sliding between the layers and further delaminating along the layers, see Figure 27. The thickness of the delaminated pieces was measured and the measured thickness is presented in Table 25. It is not clear whether water-stored blocks have a larger delamination thickness than that of the oven-dried one. For layered schist, the delamination thickness seemed to be controlled by the original thickness of the layers.

Table 24 Comparison of mass of spalling materials in furnace*.

Rock types	Oven-dried (with thermocouples)	Water-stored (with thermocouples)	Water-stored (without thermocouples)
Gabbro	A4 (1.45 g)	A3** (9.66 g)	A1 (4.50 g)
Granite	G3 (17.16 g)	G2*** (1080.64 g)	G1 (2466.12 g)

* Schist was delaminated along the interfaces, therefore the material inside the furnace was not weighed, but the thickness was measured instead in Table 27. ** Gabbro A3 was exposed to heating for about 90 minutes. *** Granite G2 was exposed to heating for 6.8 minutes.

Table 25 Comparison of spalling depth (granite) and delamination thickness (schist).

Rock types	Oven-dried (with thermocouples)	Water-stored (with thermocouples)	Water-stored (without thermocouples)
Granite	G3 (2-15 mm)*	G2 (0.5-5 mm)	G1 (3-20 mm)
Schist	S3 (24-25 mm)	S1 (27-30 mm)	S2 (20-25 mm)

* The maximum value is obtained after scaling.

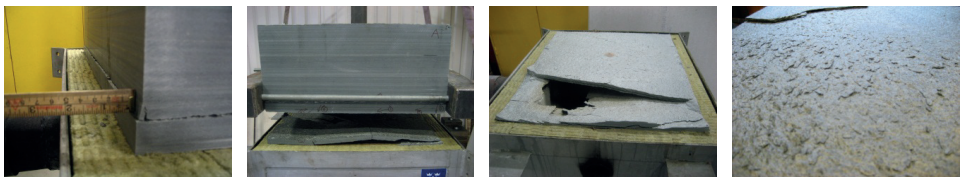

a) b) c) d)

Figure 27 Sliding and delaminating of schist block during and after heating.

4.1.2 LOCAL HEATING TESTS

Granite block: The oven-dried granite block started to spall after 4 minutes of heating (see Figure 28(a)). With the increase of the temperature, many flat chips were generated and some of them were melted and transformed into particles (see Figure 28(b)). The size of the spalling chip was small compared to the ones in the furnace tests and the maximum spalling chip was around 2 cm in diameter (see Figure 28(c)). When the local heating was completed, a cone-shaped pit with a depth of 18 mm had been formed where the torch flame hit the rock surface. The superficial spalling shape was like a circle with an average diameter 40 mm shown in Figure 29(a). The locally heated test on water-stored granite block resulted also in spalling but with less spallation compared to the oven-dried block, as shown in Figure 29(a) and (e). The weight of the spallation material is shown in Table 26. After the blocks were heated and naturally cooled, no thermal fractures appeared on neither oven-dried nor water-stored blocks surface.

Gabbro block: During heating, thermal fractures appeared on the heated surface and propagated radially from the heat source to the boundary for oven-dried as well as water-stored gabbro blocks, see Figure 29(b) and (f). Unlike granite, only small pieces were detached from the block surface during heating. The spallation material collected after the locally heated test was much less than that collected after the test on the granite blocks, see Table 26. This was true for oven-dried as well as water-stored blocks.

Schist block: During heating, no thermal fractures were formed on the heated schist block surface. However, chips were formed on the heated surface but they were thinner than for the granite blocks, see Figure 29(c) and (g). In comparison with granite, the mass of spallation material of schist collected before scaling was much less but the size of the chips was larger, see Table 26 and Figure 29. It can be seen after scaling from Figure 29(d) and (h) that the chips detached from the schist matrix mainly delaminated along its inner layer and thus produced larger flakes.

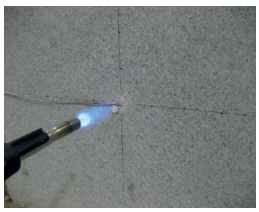
a) Spalling initiation

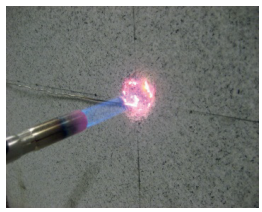
b) A cone-shaped cave formation


c) Spallation material

Figure 28 Photographs of surface spalling process for granite.

Table 26 Comparison of mass of spalling materials under local surface heating.

Rock conditions	Granite*	Gabbro	Schist*
Oven-dried	G7 (13.80-14.96 g)	A7 (2.34 g)	S7 (2.37-12.16 g)
Water-stored	G4 (6.73-11.67 g)	A5 (1.05 g)	S4 (1.41-14.02 g)

* The minimum and maximum value is obtained before and after scaling respectively.


a) Granite (G7)


b) Gabbro (A7)


c) Schist (S7)

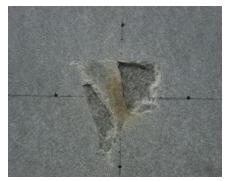
d) Schist (S7) after scaling

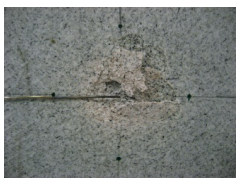
e) Granite (G4)


f) Gabbro (A5)


Schist (S4)

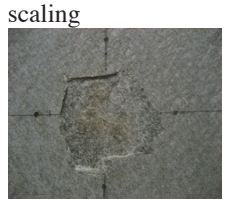
h) Schist (S4) after scaling

Figure 29 Comparison of exposure surface among three rocks under local heating (a)-(d) for oven-dried blocks; (e)-(h) for water-stored blocks.

4.1.3 MODEL TUNNEL TESTS

Granite blocks: The oven-dried confined granite block (G7) started to spall after 4 minutes of heating and pieces of spall material were ejected from the opening boundary, see Figure 30. The first thermal (macro) fracture on the surface was observed after 11 minutes of heating. Increasing temperature generated many flat chips of various sizes inside and outside of the opening. Likewise, the thermal fractures appeared on the front and back free surfaces of the block and most of them propagated from points near the hole boundary, see Figure 31. The maximum axial dimension of the chips was around 20 mm. The water-stored confined granite

block (G9) resulted in more intensive spalling than that of the oven-dried granite block (G7), see Figure 30. Spalling started after 3 minutes of heating. The thermal fractures were initiated on both free surfaces after 4 minutes of heating. The size of the chip was larger than that for the oven-dried granite block and the maximum dimension of the spalling chips was around 46 mm. During the test a few water stains appeared on the surfaces. Furthermore, some ejections were observed on the free surfaces after 4 minutes of heating. The circular cross-section of the opening was deformed to an oblong-shape after the tests for both water-stored and oven-dried granite under confinement, due to different spalling depths. The depth of spalling and mass of spalling material are presented in Table 27. The oven-dried unconfined granite block (G8) showed a somewhat different behaviour during the test, see Figure 30. Unlike the tested confined granite blocks only small chips were detached from the hole boundary. The first thermal fracture appeared on the back surface after only 2 minutes of heating. After 4 minutes of heating, part of the block was split off and moved around 2 cm relative to the main block due to the initiation, propagation of thermal fractures and sudden energy release. Some thermal fractures with different alignments were generated simultaneously which acted in plane along the opening axis. Snapping sounds were heard frequently during the test.

Gabbro blocks: Surface pitting initiated for the oven-dried confined gabbro block (A8) after 6 minutes of heating (Figure 30). However, the chips were not detached from the opening boundary. Thermal fractures appeared on both free surfaces after 13 minutes of heating and propagated radially (Figure 31). The water-stored confined gabbro block (A9) suffered superficial spalling after 3 minutes of heating and thermal fractures were initiated after 6 minutes of heating (Figure 30). While conducting the test, water stains appeared on both free surfaces frequently and small particles were detached from the opening boundary. After conducting the tests for both oven-dried and water-stored blocks, the colour of the samples became slightly lighter surrounding the opening within a distance of about 30 mm due to fire-induced mineral changes. The collected material after the test was substantially less than that collected from the granite blocks, see Table 27.

Schist blocks: During heating, no thermal spalling occurred on the heated opening of the oven-dried or the water-stored schist blocks, see Figure 30. The schist layers were positioned perpendicular to the opening axis and parallel to the free surfaces. Thermal fractures also appeared on both free surfaces and propagated radially, see Figure 31. Fractures occurred along the interfaces of the layers after tests, see Figure 32.

Table 27 Conditions and observations of spalling.

Rock type*	Depth of spalling	Mass of spalling	Maximum dimension of chips
Granite (OD, UC)	29 mm	1386 g	20 mm
Granite (WS, UC)	33 mm	1654 g	46 mm
Granite (OD, WC)	5.3 mm	14 g	18 mm
Gabbro (OD, UC)	1 mm	Not measured**	Not measured**
Gabbro (WS, UC)	2.6 mm	19 g	52 mm
Schist (OD, UC)	No spalling		
Schist (WS, UC)	No spalling		

*WS: Water-Stored, OD: Oven-Dried, UC: Under Confinement, WC: Without Confinement.
**The chips were still attached on the opening boundary after the test.

a) Granite (G7) (OD, UC)

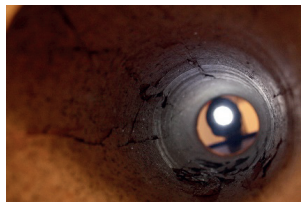

b) Granite G9 (WS, UC)

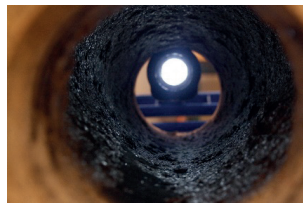

c) Granite G8 (OD, WC)

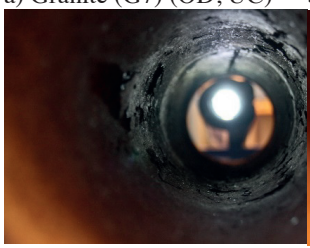

d) Gabbro A8 (OD, UC)

e) Gabbro A9 (WS, UC)

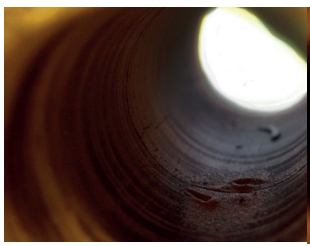

f) Schist S7 (OD, UC)

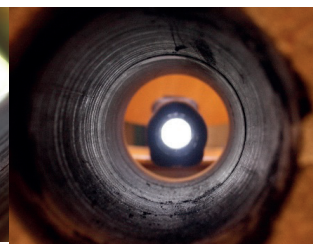

g) Schist S8 (WS, UC)

Figure 30 Photographs of opening boundary after heating.

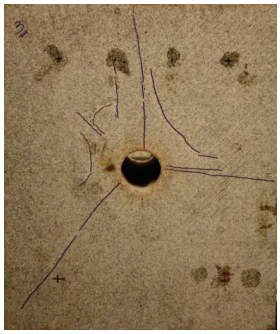

a) Granite (G7) (OD, UC)

b) Granite G9 (WS, UC)

c) Granite G8 (OD, WC)

d) Gabbro A8 (OD, UC)

e) Gabbro A9 (WS, UC)

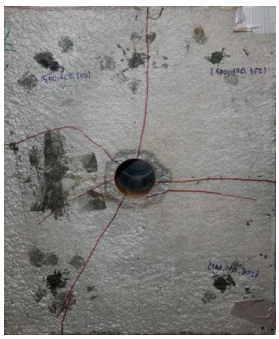

f) Schist S7 (OD, UC)

g) Schist S8 (WS, UC)

Figure 31 Comparison of thermal (macro) fractures on the front surface of all blocks after heating.

a) Schist S7 (OD, UC)

b) Schist S8 (WS, UC)

Figure 32 Fractures along the layer interfaces of schist after heating.

4.2 Acoustic emission

Acoustic emission (AE) is an elastic stress wave generated by the rapid release of energy within a material when it undergoes deformation. The energy of the AE is mostly within the frequency range 1 kHz to 1 MHz. The AE is usually due to defect-related phenomena and is produced by the sudden internal stress redistribution of the materials caused by crack initiation and growth, crack opening and dislocation movement. The rapid growth of micro-cracks, a phenomenon associated with fracture, produces acoustic emissions. These acoustic emissions propagate from the source, throughout the material and can be detected by an AE sensor placed on the surface. The sensor converts the mechanical stress wave into an electrical signal which can be recorded (Figure 33). In this way the information about the existence and location of possible sources can be obtained. AE is mostly used for detecting and locating defects as they occur, across the entire block of material (e.g. rock mass) and AE monitoring can provide significant information about the early changes in physical and mechanical properties in the rock.

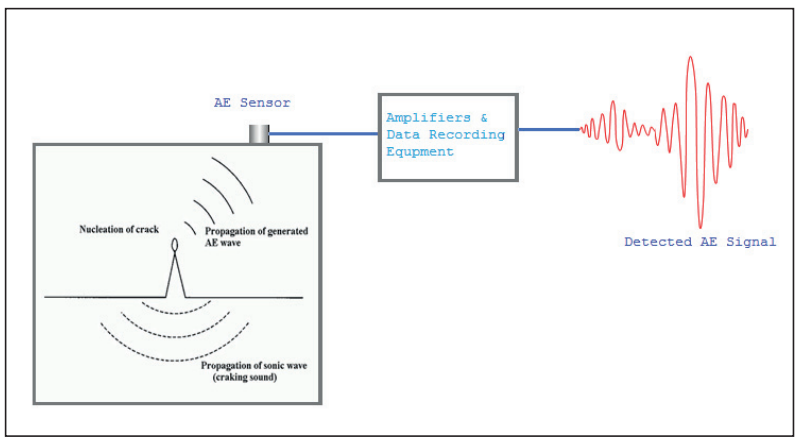

Figure 33 Principle of Acoustic Emission

In this project, a number of laboratory measurements have been carried out to monitor the initiation and propagation of fire induced fracturing in three rock types, e.g. granite, gabbro

and schist, typical for Swedish tunnels. Laboratory measurements have been conducted under uniform heating and local heating conditions in unconfined conditions.

4.1.4 INTRODUCTION/BACKGROUND

The fire in the tunnel produces heat, which then transfers to the surrounding rock mass. Due to different thermal properties of the minerals in the rock, when a rock is exposed to high temperature, unequal expansion of the component minerals takes place due to different thermal properties of the minerals in the rock. This creates thermal stresses and develops micro-cracks (either opening of existing ones or developing of new ones) which convert into macro-cracks on further heating. Characteristic for tunnel fires is that they develop violently and rapidly, and can reach a temperature of 1000 °C in five minutes. This may cause serious deformation in rock which increases the risk of collapse.

When the macro-cracks are formed and emerge at the surface, some part of the heated rock can break away. Thermally induced micro-cracking in the rock gives rise to changes in its physical properties and mechanical behaviour. The initiation and the development of thermally induced micro-cracks in three types of rocks e.g. blocks of granite; gabbro and schist were studied by continuously monitoring the acoustic emissions and temperature.

The changes in the physical properties of rocks as a function of thermal cracking is a subject of great interest in different sectors such as safe design of nuclear and toxic waste repositories and underground structures. These changes may have adverse consequences on the integrity of the rock mass. For example, stability of the tunnel structure is a key issue when concerning fire. The effect of temperature on rock properties has been widely studied on laboratory-scale specimens. Although numerous experimental programs have been conducted on the mechanical behaviour of thermally loaded rocks, the evolution of micro-cracks with respect to temperature is still not completely understood. Furthermore, most of the previous research focused on granitic rock, gabbro and to a lesser extent, on limestone at temperatures up to 600°C. A number of researchers (Heuze, 1983; Homand and Troalen, 1984; Hommand-Etienne and Houpert, 1989; Duclos and Paquet, 1991; Jansen et al. 1993) have investigated the development of thermal cracks by continuously monitoring AE generated during thermal cycles in granite specimens. They showed that, at high temperatures, micro-cracks open and coalesce to form a macroscopic fracture. The literature review showed that the rock behaviour during and after high temperature in tunnel fires is an important but poorly understood issue, especially for hard crystalline rock such as gabbro, granite and schist. Furthermore, several properties, e.g grainsize, inhomogeneity, mineral composition, porosity, rock strength, fracture toughness etc. and conditions which promote the tendency of rock to fail have still not been well investigated at very high temperatures.

The advantage of using a laboratory environment to study the process of cracking is that the thermal load is created in a controlled temperature. On the other side there are problems with the design of the experiments. For example, the rock blocks are in unconfined conditions, which is not the case with the rock mass in tunnel structure. There are also some problems with the interpretation of the AE signals because the open surfaces around the laboratory specimens cause reflections and ultimately distortion of the waveforms. As a result, laboratory data are not completely representative of data from full-size structures. The results of such laboratory experiments can be used to analyse the sources of the generated elastic waves (acoustic emission - AE) due to micro-cracking and to study the propagation of micro-cracks and ultimately creating macro-cracks and the failure of rock. This work focuses on

study and evaluation of AE activities, with a few different parameters: number of the events, source location, source radius, magnitude and energy, and the energy ratio of S- to P-waves - E_s/E_p.

4.1.5 LABORATORY TEST DESIGN FOR AE

The rock blocks of granite, gabbro and schist were subjected to heating up to 1100°C following the typical HC fire curve. The rock types and the conditions for the fire test are presented in Table 28. The temperature was measured continuously inside the heated blocks at different distances from the heat. The typical fire curves (ISO-834 and hydrocarbon curve) and the measured temperature curves during uniform and local heating at the source of the heat are presented in Figure 34.

Table 28 Summary of the rock block number, type, dry or saturated, duration and type of heating for the test blocks with AE monitoring.

Rock type	Uniform heating			Local heating	
	Saturated/Duration (min)		Dry/Duration (min)	Saturated/ Duration (min)	Dry/ Duration (min)
Gabbro	A1/25	A3/90	A4/25	A5/60	A7/60
Granite	G1/25	G2/ 7	G3/25	G4/60	G7/60
Schist	S1/25	S2/25	S3/25	S4/60	S7/60

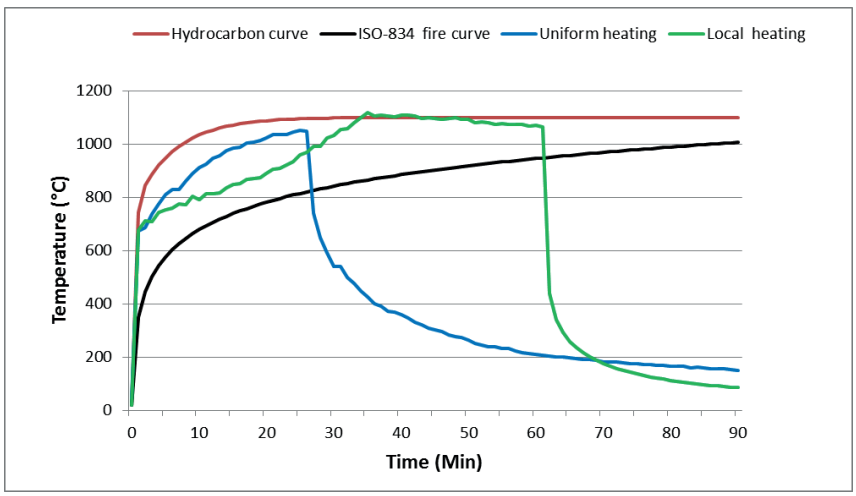

Figure 34 Typical fire curves (ISO-834 and hydrocarbon curve) and some typical measured temperatures during uniform and local heating tests at the source of the heat.

The heating of the blocks continued between 7 and 90 minutes. The AE was recorded on all blocks during the heating and cooling up to 60 minutes, except for block A3 when the processes were monitored for 90 minutes.

4.1.6 DATA ACQUISITION

The AE was continuously monitored during all fire tests using a Hyperion Ultrasonic System manufactured by the Engineering Seismology Group (ESG, Canada). The sensors were single-component piezoelectric type, manufactured by Physical Acoustics Corporation (R6α model). They have a resonant frequency of 55 kHz and operate in the frequency range 35-100 kHz and in a wide temperature range -65 ºC to 175ºC. The sensors were mounted at eight different locations on the top surface of the test blocks using silicon high vacuum grease as a coupling material (Figure 35Figure 4.3). The sensors were kept in the position by metal brackets and a piece of insulation material. Prior to AE monitoring of each rock block, the data acquisition system, was triggered to ensure that the system is working correctly and to check the background noise. A pencil lead test was also carried out to ensure sensors were all working properly and the coupling of the sensor to the specimen was good. Once the system was found to be operating correctly, fire (heating) tests were performed on the rock blocks.

The recorded signals from the sensors were amplified by a 40 dB fixed gain and then digitized. A sampling frequency of 10 MHz was chosen for this study. The digitized signals were then stored in the computer for further analysis. The ESG UltrACQ data acquisition system was used for the real-time monitoring of the AE events. To avoid unnecessary recording of noise the threshold trigger value was set to 5 out of 8 channels (sensors).

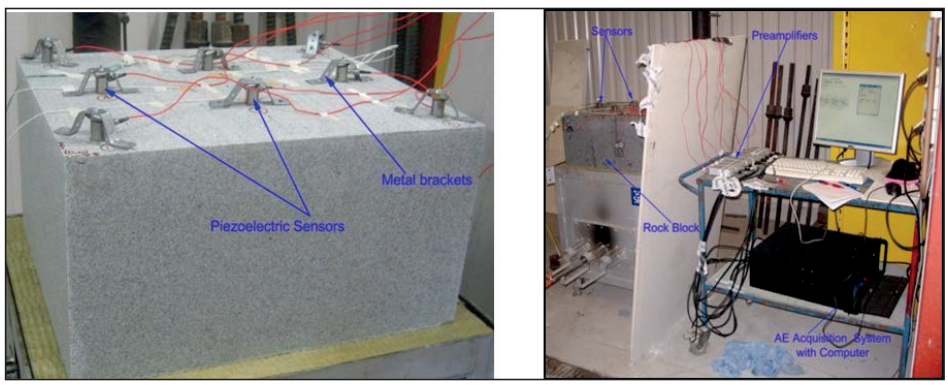

Figure 35 Laboratory set up for AE monitoring during heating tests.

4.1.7 DATA PROCESSING AND PARAMETER ESTIMATION

AE data was processed and analyzed using the software “WaveVis” from ESG. This software allows the user to pick the arrival times of P- and S-waves and to calculate a number of source parameters of the AE events. Initially, the locations of AE events were determined from automatically picked arrival times of P-waves and S-waves. Since this automatic picking did not give satisfactory results all arrival times were picked manually to increase their accuracy.

Detected AE waves can be used to obtain a variety of AE parameters and these parameters can be used to study the fracture processes. The source parameters of the AE events calculated in this study are: source location (hypocentre), origin time, magnitude, energy, and E_s/E_p ratio. Before the source parameters were calculated an average velocity was estimated for each rock type (at room temperature and during the tests).

Velocity model

Acoustic wave velocities depend on the mechanical properties of the material, or the elastic properties, which in turn depend on the physical characteristics, such as the mineralogical composition, porosity, anisotropy, the presence of cracks, etc. The mechanical properties depend also on the temperature.

During the heating experiments the rock blocks were exposed to different temperatures in different areas of the block up to 1100°C. The elastic properties of the blocks during the tests change and depend on the temperature as well as the micro- and macro-crack density, e.g., they depend on the time and the position within the block. The acoustic wave velocities change in a wide range during the experiments. The available data did not allow us to know very accurately the complex pattern of the velocity in time and space. A literature review was conducted to find a correlation between the temperature and the velocities of P- and S-waves for different rock types. Only a few studies relevant to our temperature range and rock types were found. For example, Keshavarz et al. (2010) studied the change in elastic wave velocities with progressive increase in the temperature up to1000ºC for gabbro. They found a significant decrease in the seismic wave velocities with a temperature increase from room temperature up to 1000ºC. The P-wave velocity changed from 6700 m/s to 1200 m/s and the S-wave velocity from 4200 m/s to 900 m/s.

For this study a procedure was developed and followed to estimate an average velocity during the experiments for each rock type. The velocities of the P-waves were measured on small core samples with transducers with frequency 1 MHz following a standard procedure (Table 29). The measured velocities at room temperature are the maximum possible velocities for each rock type. The S-wave velocity was calculated assuming Poisson's ratio of 0.25.

A procedure was developed to find average (optimum) velocities for P- and S-waves for the whole block and during the whole experiment. For this aim the source locations of the AE events were calculated for different constant velocities starting with the maximum velocity The distribution of location errors and the number of events with solutions and zero depth were compared. Usually if the software cannot find a suitable solution for the location, the location is set to be at the upper boundary of the block (at the sensor level) or no solution is defined. The velocity with the smallest average error of all solutions for the AE events and smallest number of events with poor (zero depth) locations was defined to be the optimum ('best') velocity. The 'best' seismic velocities were found to be: V_p =2500 m/s and V_s =1667 m/s (for gabbro and schist), and V_p = 2250 and V_s =1500 (granite). These velocities were used for the further processing of acoustic emissions events of all tested rock blocks of the corresponding type.

Table 29 Average velocities calculated from the standard laboratory measurement for the three different rock types at room temperature and 'best' average velocity during the uniform heating tests.

Rock Type	V_p (m/s)	V_s (m/s)	V_p (m/s)	V_s (m/s)
	Room temp.		'Best' Average	
Gabbro	3903 ±275	2649±265	2500	1667
Granite	4174 ±165	2513 ±176	2250	1500
Schist	4195 ±234	2373 ±199	2500	1667

AE events location

Source (hypocentre) location is the point in space where the cracking during the AE events starts and the origin time is the time when it occurs. The accuracy and reliability of the source locations are influenced by various factors: the accuracy of the arrival times, the spatial sensor configuration, the location algorithm and the accuracy of the velocities of seismic wave. The arrival time picking is one of the most important factors. Manual picking ensures the best quality of the data.

The source location was calculated using manually picked P- and some S-wave arrival time data by a simplex algorithm (Nelder and Mead, 1965). The simplex technique with a good estimate of the input parametres (initial trial event location) locates the source rapidly and with a high degree of reliability. The common location algorithms assume a homogeneous and isotropic material, i.e. a constant wave propagation velocity for the whole structure and all directions. That is why we needed to estimate an average velocity. More precise locations can be calculated using 3D velocity model but ESG software cannot be used for this case.

Magnitude

The uniaxial magnitude (uMag) was estimated with the WaveVis software. The value is calculated using the unclipped (good) peak amplitudes of a single component trace recorded by each sensor. A correction for the source-sensor distance is made using the formula:

$$uMag = Alog(R \cdot ppv) + B \qquad (4.1)$$

where ppv is the peak particle velocity in mm/s, R is the distance from source (hypocentre) to the sensor in mm, A and B are coefficients with default values $A = 1.51$ and $B = 1.24$ in the WaveVis software. The magnitude for each event is calculated as the average from all sensor magnitudes. The coefficients in Equation (4.1) are set at the default value in the software. They depend on the attenuation of the S-wave. The defaults were used

Energy

The energy by WaveVis software is calculated from the integral of the energy flux J_c separately for P and S- waves using the following formula (ESG, 2010):

$$E_c = \frac{4\pi\rho R^2 J_c}{F_c^2}\langle F_c^{-2}\rangle \qquad (4.2)$$

where ρ is the density of the source material in the medium in kg/m^3, R is the hypocentral distance in mm, F_c denotes the average radiation pattern coefficient (for P-wave or S-wave) and c is the seismic wave velocity (for P-wave or S-wave). The total seismic energy obtained is the sum of the energy of the P- and S-waves.

Source radius

Source radius is the radius of the equivalent circular surface over which slip occurred during a seismic event. The radius usually is calculated for the most common source models: Brune's (1970) kinematic model and Madariaga's (1976) quasi-dynamic model. In this study the source radius is calculated assuming the Madariaga's model, as it was shown to provide more realistic source radius estimates. The source radius r_0 is calculated from the corner frequency

(f_c) of the recorded spectrum of P- or S-waves (corrected for attenuation) using the following equation

$$r_0 = \frac{K_c \beta}{2\pi f_c} \quad (4.3)$$

where K is a constant, which depends on the selected model (2.01 for P-waves, and 1.32 for S-waves, for Madariaga's model), and β is the S-wave velocity.

E_s/E_p ratio

The ratio of S-wave to P-wave energy can be used as an indication of the source mechanism, responsible for the generation of seismic events. In the literature there are different correlations between this ratio and the type of the focal mechanism. For example, according to Cai et al. (1998) if $E_s/E_p < 10$, that implies a cracking process involving tensile failure and if $E_s/E_p > 20$ – then it is a shear failure dominated process. Another recent study by Kwiatek and Ben-Zion (2013) analyzed the E_s/E_p ratio of 539 microseismic events with local magnitude from -5.23 to -2.41(similar to AE magnitude of this test) in Mponeng Deep Gold Mine (South Africa). The result suggested that significant number of events with relatively low E_s/E_p, less than 5 were with pure tensile failure. We use this latter criterion to define the type of the events.

4.1.8 AE DURING UNIFORM HEATING

AE was recorded during the heating and cooling process (to room temperature) in uniform heating tests. The AE data were then processed, and AE parameters were calculated and analyzed to investigate the distribution and development of AE activities in all rock blocks. The results for the number of the AE events, magnitudes, the E_s/E_p ratio, and the source radius are presented for all blocks in Figure 36, and Figure 40 to Figure 42 for comparison.

Gabbro

Two blocks: A1 (saturated gabbro) and A4 (dry gabbro) were heated for 25 minutes while block A3 (saturated gabbro) was heated for 90 minutes. The temperature curve for the oven was the same for all three blocks for the first 25 minutes. The recorded total number of AE events during an hour for blocks A1 and A3 (saturated and dry gabbro) was very different: 1599 and 3148, respectively. The total number of AE events in block A3 was 5162, more than 3 times that number in block A1. For the first 25 minutes the total number in block A3 was 1942, slightly higher than the total number for block A1. The total number of the events in block A3 was the highest from all tested blocks.

The AE activity started slowly in all three blocks at the beginning of the heating and after 10-14 minutes (~800°) the rate increased sharply reaching a maximum around 15-18 minutes (~900°) from the beginning. (The temperature mentioned here and everywhere else in this chapter is the oven temperature. The real temperature in the block is much lower and it depends on the distance from the heated surface. The maximum number of events in blocks A1 and A3 (both saturated) was reached at almost the same time but there was a difference in the rate (number of the events per minute) – around 100 events/minute for block A1 and around 150 events/minute for block A3. The blocks were prepared and heated in the same

way for the first 25 minutes. The difference in the number of events can be a result of local variations in heterogeneities or the initial micro-cracks in the blocks.

The comparison between the percentage of the events during heating and cooling for blocks A1 and A4 (saturated and dry) gabbro showed that in case of A1 about 78% AE events were generated during heating and 22% of AE were recorded during cooling, and in the case of A4, about 59 % of AE events were recorded during heating and 41 % during the cooling process (Figure 36). It can be noticed that after the cooling started the rate of the AE per minute initially decreased in both blocks but almost immediately the rate in block A4 started to increase again until minute 30-32 when there was a secondary peak. In contrast, the activity in block A1 slowly decreased during the cooling process.

In block A3 (saturated gabbro) where the heating continued for 90 minutes there was a secondary peak in the AE activity around 45 minutes(~1100°) from the beginning, and another one after the cooling started (~90 minutes ~900°).

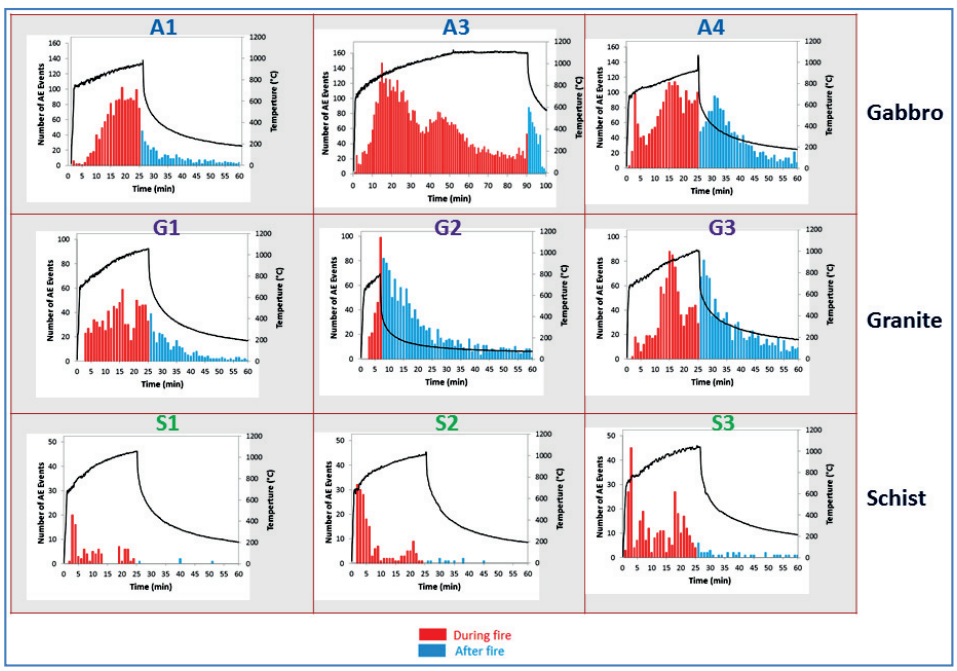

Figure 36 AE rate (number per minute) recorded during uniform heating (red) and cooling (blue) in all blocks. The furnace temperature is shown as a black line.

The AE locations for gabbro (top row on Figure 37) show clearly concentration along certain lines for A1 and A3 (saturated) blocks while for block A4 (dry) the locations are like a cloud in the centre of the block with some clustering but without clear alignment. A good correlation was found between the AE location alignments and the macro-cracks at the heat-exposed surface for saturated gabbro (A3) under uniform heating for 90 minutes (Figure 38) but not all clusters of AE events correlate with macro-cracks. Possibly there were internal macro-cracks which were not visible on the surface.

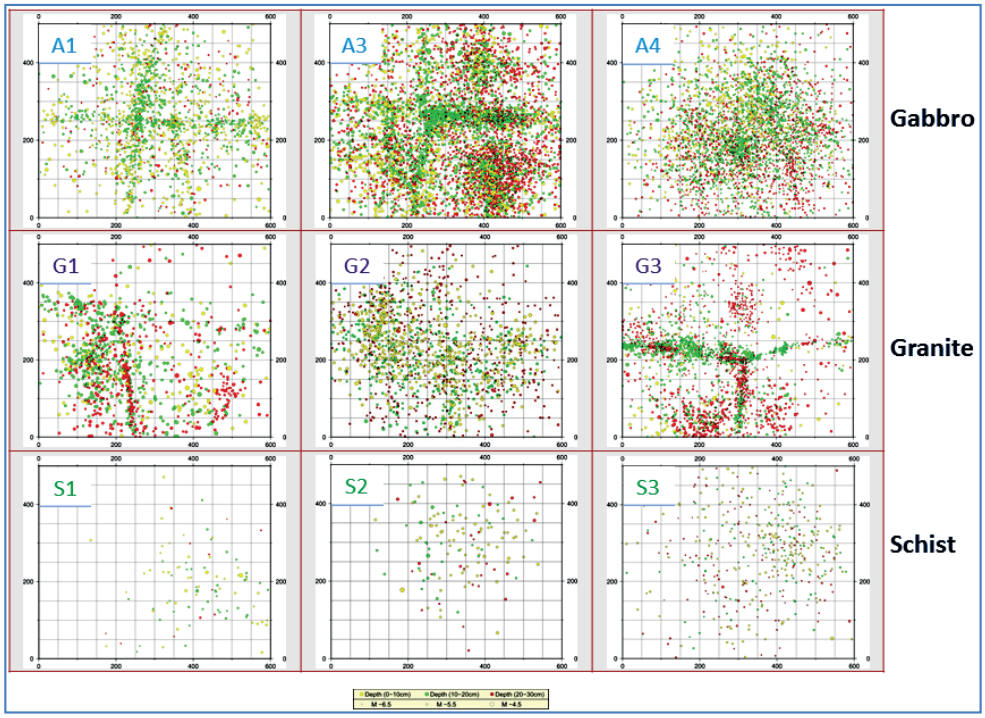

Figure 37 AE locations during uniform heating in all blocks. The size of the circles depends on the magnitude and the colour – on the depth (the distance from the heating surface.

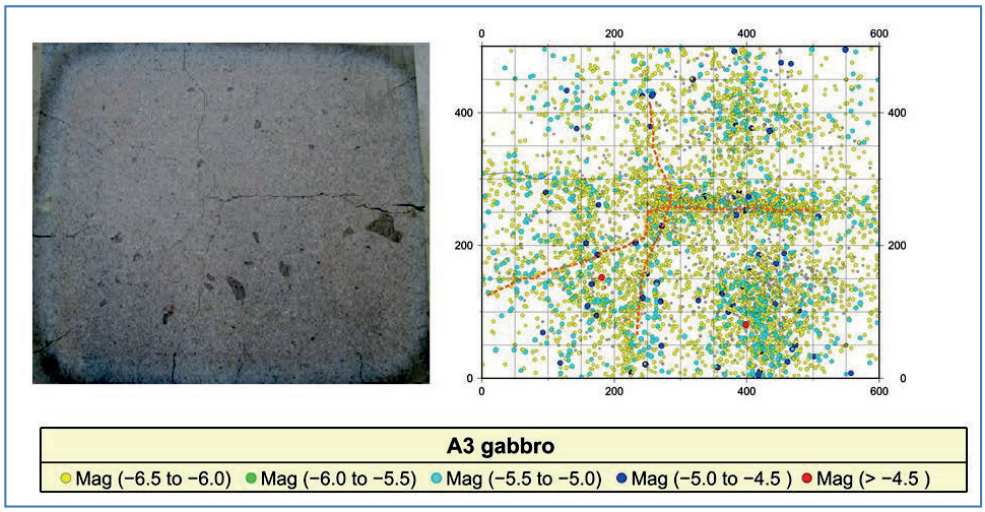

Figure 38 Photo of the surface exposed to heating (left) and AE locations in saturated gabbro (A3) under uniform heating (right). The colour of the circles represents the magnitude (see the legend).The dashed red line corresponds to the major macro-cracks observed on the surface.

The magnitudes of the AE events in all gabbro blocks range from -6.5 to -4.3. There was no substantial difference in the maximum magnitudes between saturated and dry blocks or between the blocks heated for 25 or 90 minutes. The magnitudes increase towards the heated surface of the block and the largest events were recorded at the closest proximity to the heated surface (Figure 39).

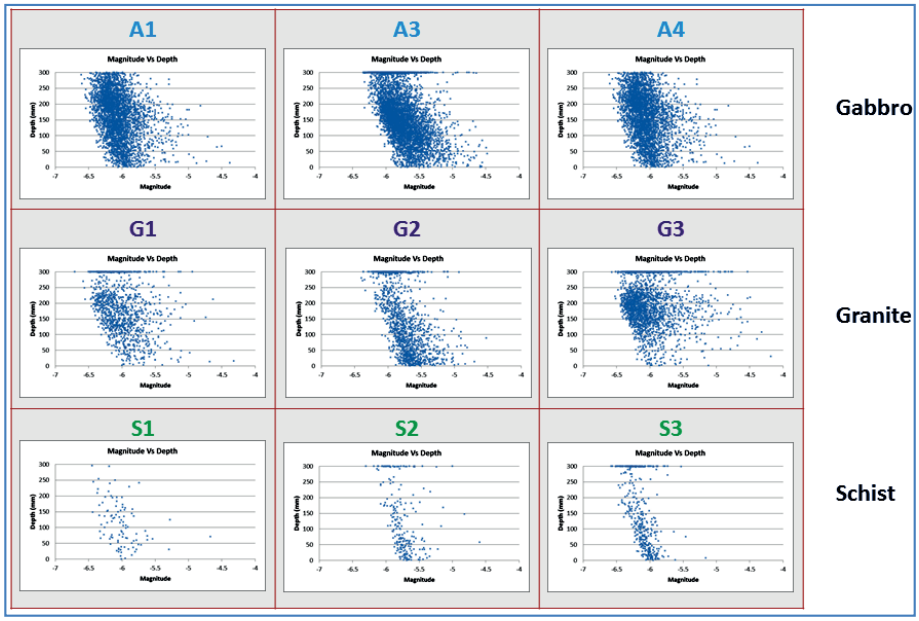

Figure 39 Magnitude distributions with depth (distance to the heated surface) for all tested rock blocks under uniform heating.

The S- to P-wave energy ratio (E_s/E_p) is below 10 in all gabbro blocks. Most of the events have E_s/E_p ratio less than 5 showing pure tensile failure type (Figure 40). There are still a few events with E_s/E_p ratio larger than 5, up to 10, which indicates that there were also cracks formed as a result of a shear failure. There were less of these events in block A1 (saturated gabbro) compared to block A4 (dry gabbro). The number of these events in block A3 was also larger compared to block A1 (both saturated gabbro, heated for different duration).

The source radius for all gabbro blocks varies between 0.3 and 0.8 mm, although there are a few AE events with source radius larger than 0.8 mm (Figure 41). The estimated length of the cracks should be calculated as double the radius or ~ 0.6 to 1.6 mm.

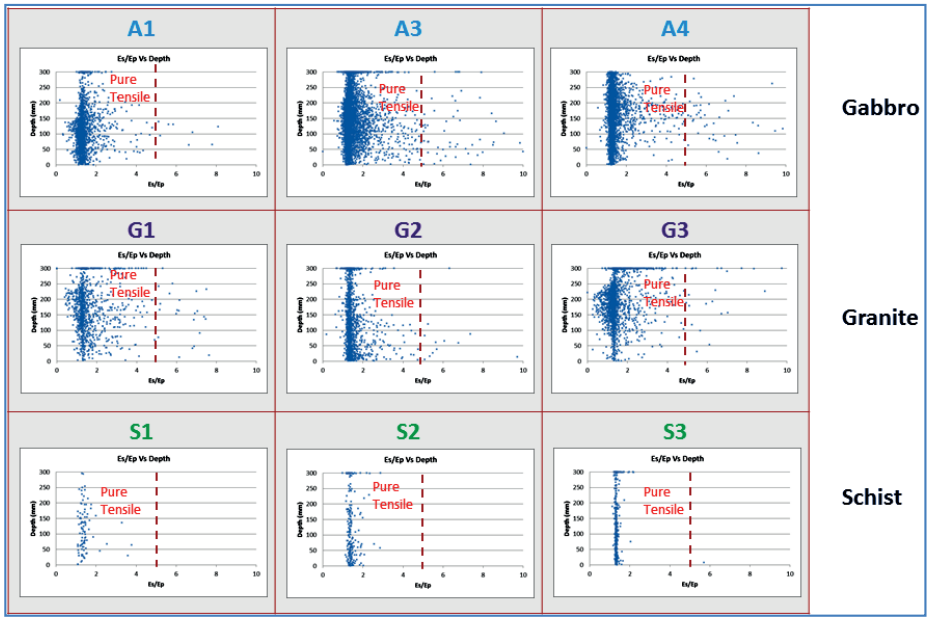

Figure 40 E_s/E_p ratios as a function of the depth (distance to the heated surface) for all tested rock blocks under uniform heating.

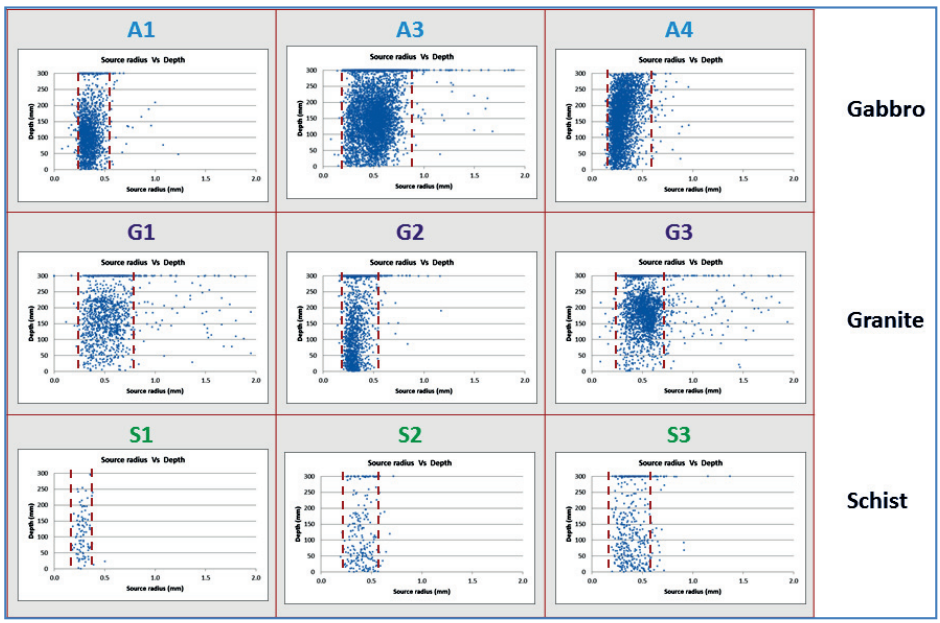

Figure 41 Radii of the AE sources as a function of the depth (distance to the heated surface) for all rock blocks under uniform heating.

The cumulative energy graph can be used for study of the development of the AE with time and rock fracturing respectively. The cumulative energy of AE for gabbro blocks under uniform heating is presented in Figure 42. Changes in the cumulative energy slope were observed in all blocks with some variations between them. The first change in the slope of the graph is observed approximately 10-14 minutes after the heating started. After this the slope changed in a different way in different blocks. There is no clear correlation between the rate changes in the AE activity and the changes in the cumulative energy slope. One of the reasons for this could be that the larger number of AE events does not always mean larger energy as the events could be all small. Areas with different slope of the cumulative energy were defined for each block. They will be studied further from a rock mechanical point of view.

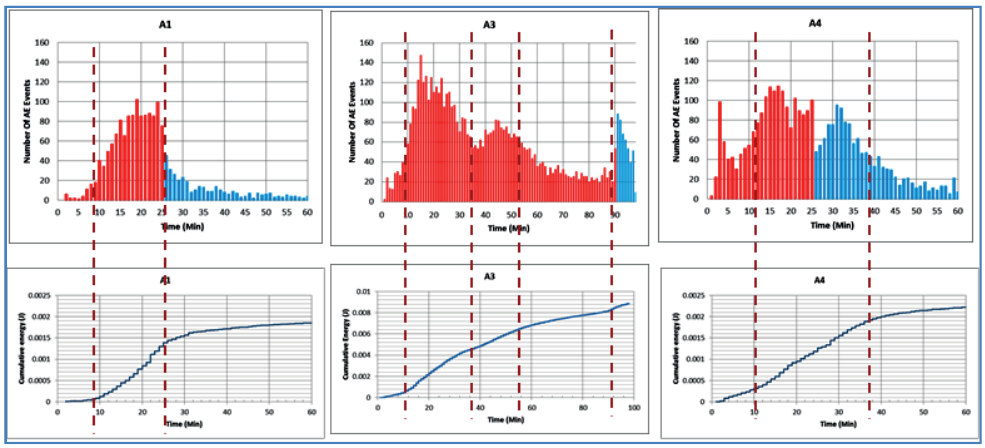

Figure 42 AE number and Cumulative AE energy for gabbro blocks. The dashed vertical lines mark the time when changes in cumulative energy slope were observed.

Granite

Two blocks: G1 (saturated granite) and G3 (dry granite) were heated for 25 minutes while block G2 (saturated granite) was heated for 7 minutes keeping the same temperature curve as the other two blocks for 7 minutes. The recorded total number of AE events during an hour for block G1 (saturated granite) was much smaller (1105 events) compared with G3 (dry granite) (1778 events). The total number of AE events in block G2 was 1382, more than AE number in block G1 even though the block was heated only for 7 minutes, a much shorter time than 25 minutes for block G1.

The AE activity started almost abruptly 2-3 minutes after the beginning of the heating in blocks G1 and G2 (saturated granite) when the oven temperature reached ~700°C. For block G3 the AE increased slower up to 12 minutes and then abruptly increased (at temperature ~800°C). The maximum rate in the AE activity was reached in about 15 minutes (for block G1 and G3) when the temperature was close to 1000°C and then it started to decrease. For block G2 the heating continued only for 7 minutes and the maximum was observed in that time.

The maximum number of events in blocks G1 (saturated) and G3 (dry) was reached almost at the same time but there was a difference in the number of the events – around 60

events/minute for block G1 and around 90 events/minute for block G3. Hence, for the block of dry granite (G3) the maximum number of events was much higher than for the block with saturated granite (G1). On the other hand the other saturated granite block (G2) had a maximum number of events around 100 only 7 minutes from the beginning of the heating. This was a sudden increase in the AE rate, around three times higher than the rate in block G1 (also saturated granite) at the same time.

The AE activity slowly decreased during the cooling in both saturated blocks (G1 and G2). In dry granite (G3) there was a secondary peak in the activity immediately after the cooling started and then the activity decreased with the temperature decreasing.

The comparison between the percentage of the events during heating and cooling for blocks G1 and G3 (saturated and dry granite) showed that in case of G1 about 74% AE events were generated during heating and 26% of AE were generated during cooling, and in case of G3, about 50 % of AE events were recorded during heating and 50 % during the cooling process (Figure 36).

The AE locations for granite (second row on Figure 37) show clearly concentration along certain lines for G1 and G3 blocks while for block G2 the locations are like a cloud in the centre of the block without clear alignment. A good correlation was found between the AE locations and the macro-cracks at the top surface for dry granite (G3) under uniform heating (Figure 43). There are still some clusters of AE events that do not correlate with the visible macro-cracks and there are macro-cracks that do not correlate with alignment of AE locations.

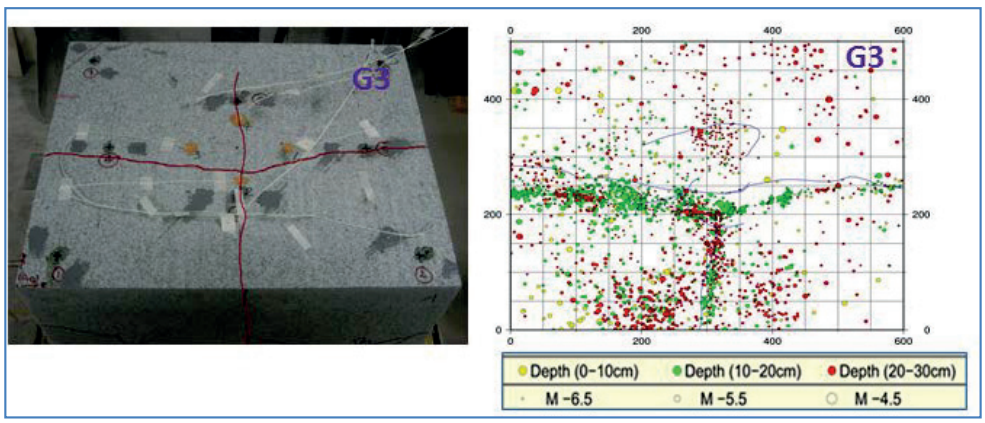

Figure 43 Photo of the top surface (left) and AE locations for dry granite (G3) (right) under uniform heating. The colour of the circles represents the distance from the heated surface (depth) and the size represents the magnitude (see the legend). The macro-cracks on the photo are enhanced and shown as red lines.

The magnitudes of the AE events in all granite blocks range from -6.7 to -4.2. The largest AE events (up to -4.2) from all types of rock were observed in granite. There was no substantial difference in the maximum magnitudes between saturated and dry blocks or for the blocks heated for 25 or only 7 minutes. The magnitudes increase towards the heated surface of the block and the largest events are recorded at the closest proximity to the heated surface (Figure 39).

The S- to P-wave energy ratio (E_s/E_p) is below 10 in all granite blocks. Most of the events have E_s/E_p ratio less than 5 showing pure tensile failure type (Figure 40). There are still a few events with E_s/E_p ratio larger than 5, and up to 10, which indicates that there were also cracks formed as a result of a shear failure. There were less of these events in block G2 (saturated granite) heated for only 7 minutes then in the other two blocks.

The source radius for all granite blocks varies between 0.2 and 20 mm (Figure 41). The estimated crack length which is double the radius is between 0.4 and 40 mm. The source radius distributions for G1 and G3 blocks (saturated and dry granite) are very similar. For block G2 the radii were smaller than 0.6 mm with a few exceptions (up to 12 mm).

Schist

Three blocks: S1 and S2 (saturated schist) and S3 (dry schist) were heated for 25 minutes. The recorded total number of AE events during an hour for all blocks was: 99, 191 and 366, respectively. A smaller number of AE events were recorded in saturated schist than in dry schist. The AE activity started sharply at the beginning of the heating, after 2 minutes (~700°) and the rate increased sharply with reaching a maximum around 2-3 minutes (~750°) from the beginning. The maximum rate in blocks S1 and S2 (both saturated) and S3 (dry) was reached almost at the same time – around 20 events/minute for block S1, and around 30 events/minute for block S2, and – around 45 events/minute for block S3. A secondary maximum in the AE emission activity was observed in dry schist (G3) around 20 minutes from the beginning (temperature ~1000°).

The total number of events in block S3 (dry schist) during heating was much higher (289 events) than the total number of events in both blocks of saturated schist (95 and 181). The comparison between the percentage of the events during heating and cooling showed that only a small portion of the total number of AE events was recorded during cooling. In average around 92 % of the AE events for all schist blocks were generated during heating (Figure 36).

The AE locations for all schist blocks (bottom row on Figure 37) form a cloud without any clear alignment.

The magnitudes of the AE events in all schist blocks range from -6.4 to -4.6. There was no substantial difference in the maximum magnitudes among the blocks but the magnitudes for saturated schist (S1 and S2) are slightly higher than for dry schist (S3). The magnitudes increase slightly towards the heated surface of the block and the largest events are recorded at the close proximity to the heated surface (Figure 39).

The S- to P-wave energy ratio (E_s/E_p) is below 5 in all the schist blocks showing pure tensile failure type (Figure 40). For almost all events the ratio is between 1 and 2.

The source radius for all schist blocks varies between 0.2 and 0.9 mm (corresponding to crack length 0.4 to 1.8 mm), although there are only a few AE events with source radius larger than 0.6 mm (crack length 1.2 mm) (Figure 41).

4.1.9 AE DURING LOCAL HEATING

Laboratory experiments were conducted also by heating a small area with a torch. The heating continued for 60 minutes following the local heating curve Figure 34. The same types of rock were subjected to heating as for the uniform heating: gabbro, granite and schist. The AE events recorded during local heating and the naturally cooling process (till room temperature) were analysed to investigate the distribution and propagation of AE activities. Eight AE sensors were installed on the upper surface of the blocks. Only the hypocenter locations of the AE events were calculated for these tests, in a similar way as for the uniform heating tests. The velocities of the seismic waves used for calculation of the hypocenter locations were: Vp = 2500m/s and Vs = 1667 m/s for gabbro and schist, and Vp = 2250 m/s and Vs = 1500 m/s for granite. The other parameters of the AE events were not analysed in detail as for the case of uniform heating. The number of the phones that recorded the events (which is given as colour on the location maps) can be considered proportional to the size (magnitude or energy) of the event because the larger the event the more sensors including the more distant ones that will record it. The results for the location of the AE events for gabbro, granite and schist blocks are presented in Figures 4.12, 4.14 and 4.15 respectively.

Gabbro

The AE locations show clearly concentration along certain lines for both A7 (dry) and A5 (saturated) gabbro blocks. A good correlation was found between the AE locations and the macro-cracks at the heat-exposed surface for A7 (dry gabbro) and A5 (saturated gabbro) under local heating (Figure 44).

The development of the macro-cracks (their initiation and propagation) for the case of saturated gabbro (A5) was studied by a set of location maps of the AE events for every consecutive 5 minutes (from 5 to 60 minutes) (Figure 45).The AE events clustered initially around the centre of the block (around the heated area) then spread slowly towards one edge of the block (for up to 45 minutes) after which spread in the opposite direction. A dense population of aligned AE location formed as a result in the middle of the block from one edge of the block to the other.

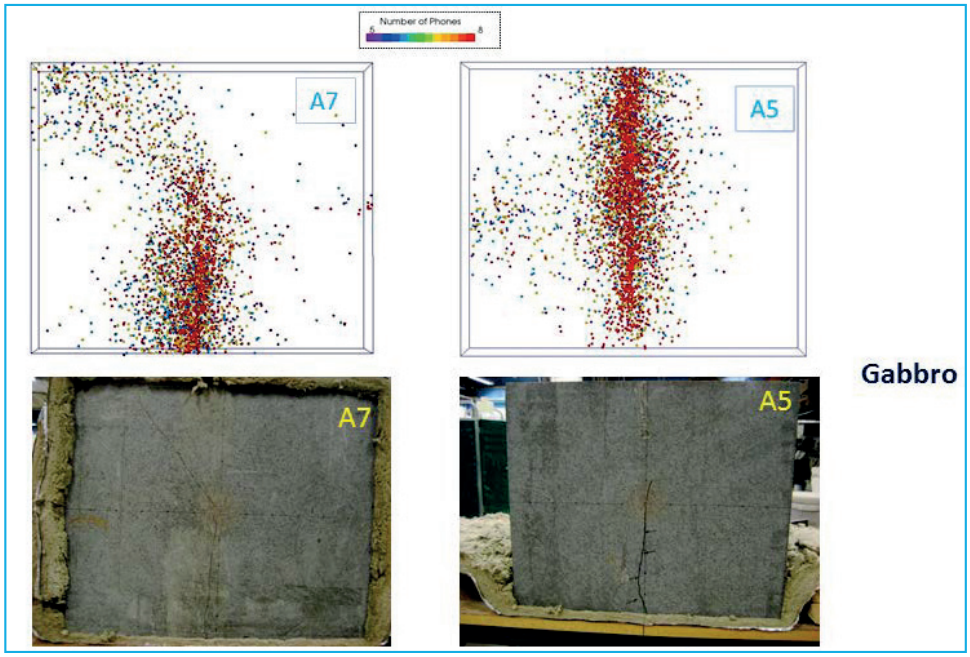

Figure 44 AE events location for dry gabbro (A7) (left) and saturated gabbro (A5) (right) and photos of fire exposed surface (below) under local heating. The colour in AE location represents the number of sensors used for the location. Usually the larger is the number of the sensors that recorded the event, the larger is their magnitude.

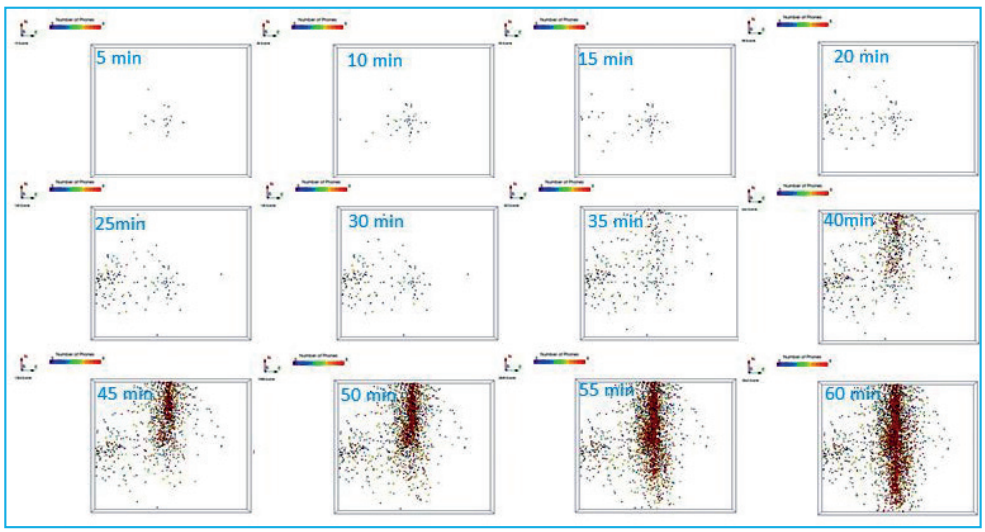

Figure 45 Initiation and propagation of macro-cracks in saturated gabbro (A5) under local heating (AE snapshots every 5 minutes up to 60 minutes).

Granite

The location of AE events showed clustering of AE events in the centre of block, in the area heated by the torch flame, for both G7 (dry) and G4 (saturated) granite (Figure 46). The area formed in the first 25 minutes and spread slightly for the next 35 minutes. Higher AE activity was observed in dry granite (G7) compared to saturated granite (G4). The central and most dense part of the AE clusters is consistent with the damage area on the heated surfaces. No cracks were formed in granite blocks.

Schist

Fewer events were located in both saturated (S4) and dry (S7) schist compared to gabbro and granite (Figure 47). Not very dense wide cluster of AE events formed in the central part of the blocks in S4 (saturated schist). The damage zone on the surface corresponds approximately to the centre of the cluster. Spread cloud of events formed in block S7 (dry schist) without any concentration of the events. There is no concentration of the AE events around the damage zone on the surface.

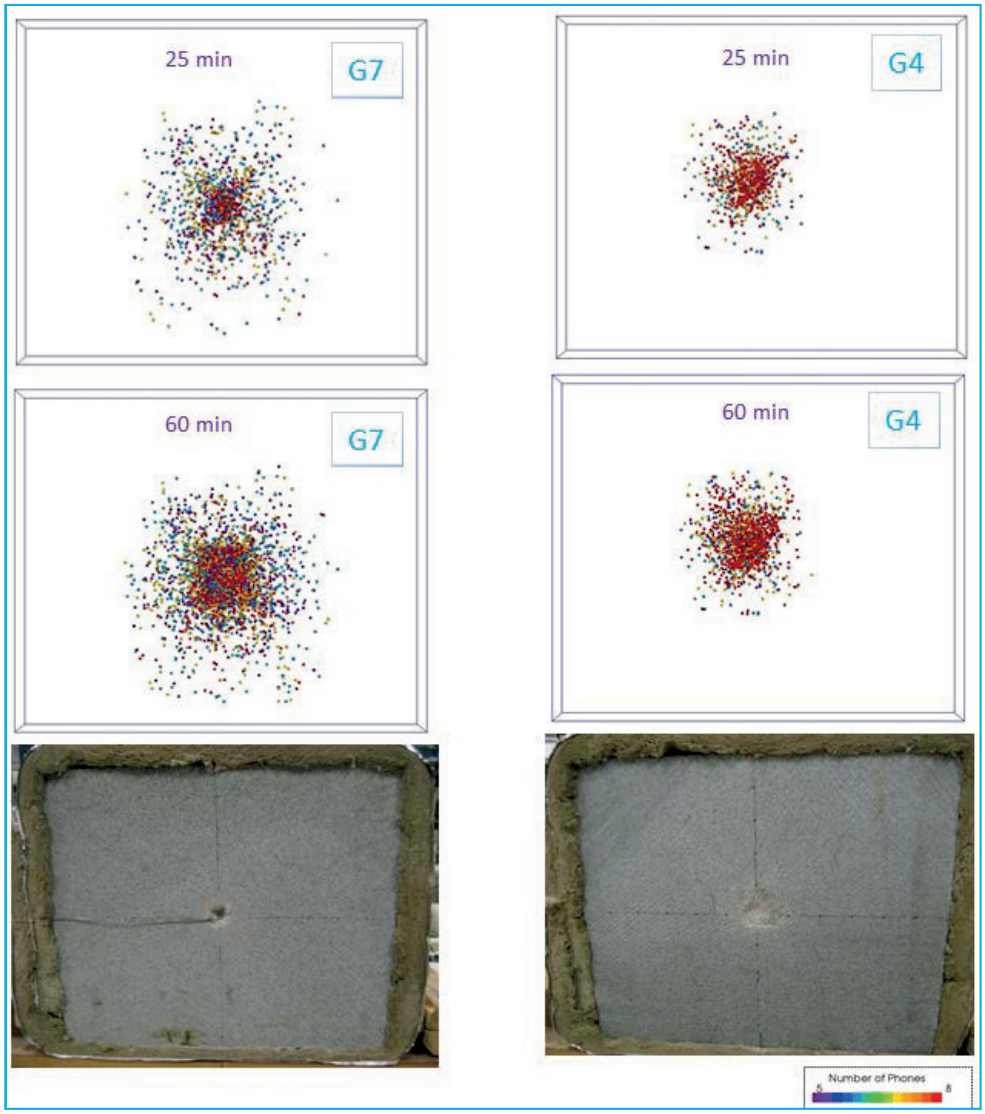

Figure 46 AE event locations for dry granite (G7 (left) and saturated granite (G4) (right) for 25 and 60 minutes after the heating started (top and middle rows) and photos of heat-exposed surface (bottom) under local heating. The colour in AE location represents the number of sensors used for the location. Usually the larger the number of the sensors that recorded the event, the larger their magnitude.

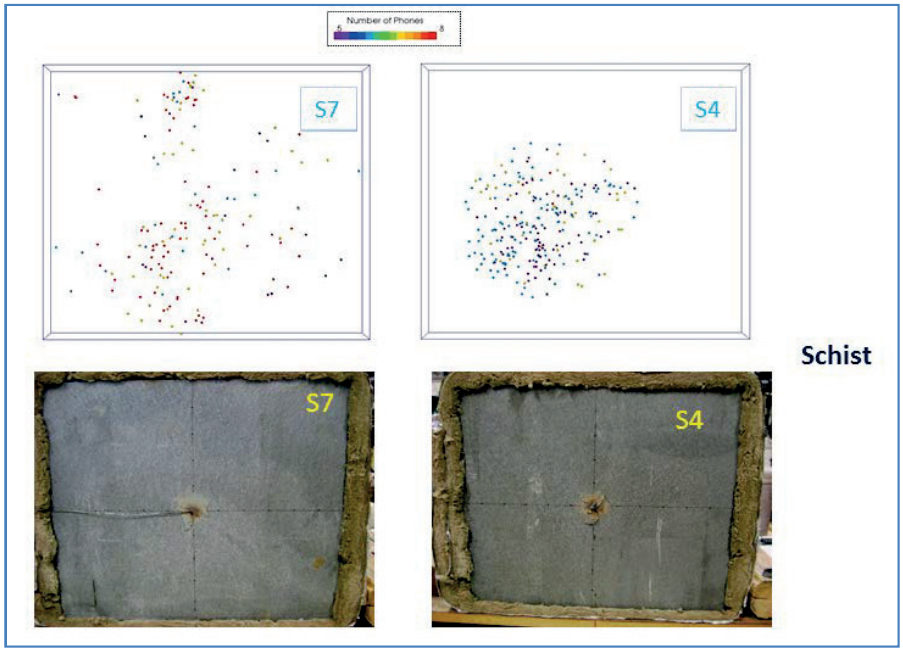

Figure 47 AE events location for dry schist (S7) and saturated schist (S4) (top) and photo of fire exposed surface (bottom) under local heating. The colour in AE location represents the number of sensors used for the location. Usually the larger the number of the sensors that recorded the event, the larger their magnitude.

5 NUMERICAL ANALYSIS

The mechanism of thermal spalling has been described by many researchers since the 1930s (Preston and White, 1934). Due to the rock's low thermal conductivity, heating produces large temperature gradients and associated compressive stresses close to the surface. Any cracks/flaws with an orientation parallel to the heated boundary are subject to propagation due to a zero or very low radial stress. The extension of the critical cracks/flaws attempts to arch up due to heating, thus promoting buckling of the extended flaws, and the spall eventually bends up. However, models of spall production remain largely empirical in nature or adopt simplifying assumptions that ignore microstructural heterogeneity. Furthermore, as can be seen from the laboratory test results, different rocks show quite different behaviour during heating. The reason for this is still not clear but the mineralogy and rock texture of different rocks seem to play significant roles on it. Since fire-induced spalling of rock has been identified as a growing concern in tunnel and mine safety, extension and depth of spalling prediction caused by fire of a certain size becomes crucial for engineering design and remedial measurement.

Therefore, the objectives of numerical analyses are to: i) determine the mechanism causing thermal spalling and thermal fracturing observed in laboratory experiments, and ii) develop a modelling technique which can be used to determine the type and extension of damage around rock tunnels caused by fire of a certain "size".

5.1 Methodology

Since the numerical modelling should be capable of explaining the mechanism of thermal spalling at grain scale and predicting the extension and depth of spalling for a real tunnel, the numerical analyses have been carried out at two different scales using a commercially available code UDEC 5.0 (Itasca, 2013). Two different numerical modelling approaches was were used:

- Micromechanical modelling (Discontinuous model): Numerical model at microscopic level was established based on the microscopic thin section observations. Different thermal and mechanical properties of minerals were considered. The temperature distribution, thermal stress and thermal fracture were examined and further validated by model tunnel tests.
- Macromechanical modelling (Continuous model): Numerical model at macroscopic level was established. A continuum damage constitutive model (stiffness and strength weakening) at macro-scale to simulate fire induced spalling was developed and implemented into the UDEC code. The temperature distribution and spalling of the rock block were simulated and validated in virtue of model tunnel tests.

As a first step of the numerical modelling only the model tunnel tests for granite and gabbro blocks were analysed. Schist block contains layers and the mineral composition of the layers has not been well investigated, therefore the numerical modelling for schist was not considered in this numerical analysis.

5.2 Discontinuous model

5.2.1 MODEL DESCRIPTION

The model presented in this section was conducted using the geomechanical code, UDEC (5.0), developed by Itasca. UDEC is able to simulate materials under extremely large deformations and discontinuous opening and sliding between discrete blocks. Moreover, as it employs Voronoi tessellation generator to create randomly sized polygonal blocks, it is useful to simulate fracture propagation between polygonal blocks; "fracturing" occurs when the joint strength between the Voronoi blocks is exceeded (Itasca, 2013). This modelling capability is necessary, as spalls are disk-like in shape; often one or-more grain-diametres in extent with thicknesses around a single grain diametre. The size of the Voronoi block used to simulate rock-forming grain in the model is 3 mm.

Only ¼ of the physical model tunnel was simulated in the numerical model due to the symmetry of the model tunnel. The geometry of the numerical model is shown in Figure 48. Rolling boundaries were applied at the left and lower sides of the model to restrict the displacement in the horizontal and vertical directions respectively. Stress boundaries were applied at the right and upper sides of the model with the value of 2.778 MPa (in compression) in the horizontal direction and with the value of 3.333 MPa (in compression) in the vertical direction respectively to simulate the confinement applied on the model tunnel test. Convective heat transfer boundaries were applied on model tunnel surface (an arc segment) as well as upper and right sides of the model. On the tunnel surface, the convective heat transfer coefficient of air was set as 30 $W/m^2 \cdot K$ to simulate the forced convection as the fire was ignited by using gas with certain blow-off air speed. On the upper and right sides of the model, the convective heat transfer coefficient of air was set as 10 $W/m^2 \cdot K$ to simulate the free convection.

The model's features include:

- 2D grain-based discontinuous model (heterogeneous behaviour is considered)
- Different mineral behaviour (quartz, feldspar/plagioclase, pyroxene, mica /muscovite)
  - Stochastic distribution of minerals
  - Temperature-dependent thermal properties of minerals
- Thermal-mechanical coupling
  - The coupling occurs in one direction only — i.e., the temperature may result in stress changes, but mechanical changes in the body resulting from force application do not result in temperature change.
- Real temperature-time curve (Step function was programmed in order to simulate a continuous development of temperature with time)
- No evaporation of free moisture (Only dry rock block was simulated)

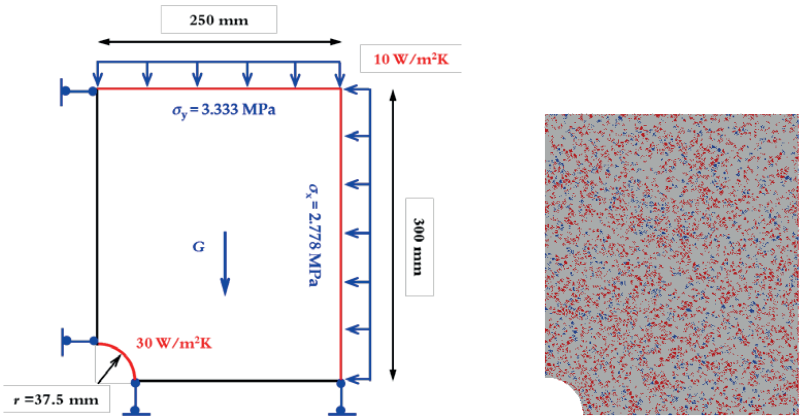

(a) (b)

Figure 48 Model geometry (discontinuous model). Blue lines indicate the displacement boundary and stress boundary condition; red lines indicate the convective heat transfer boundary condition.

5.2.2 PARAMETERS

The petrographic modal analysis for the rocks has been conducted by Saiang (2011) and the mineral composition of rock samples is presented in Table 1. By analysing the mechanical and thermal properties of each mineral, some minerals with similar properties were merged in order to simplify the model and highlight the difference between rocks. The modified mineral composition is presented in Table 30. As can be seen from Table 30, each rock only contains three main minerals, but additional mineral types can also be introduced in the numerical model if it is needed. Mechanical parameters for the individual minerals are taken from Mavko et al. (2003), while the temperature dependent thermal properties (thermal conductivities, heat capacities and thermal expansion coefficients) are based on values reported in Robertson (1988) and Ahrens (1995). The mechanical and thermal properties of different minerals at room temperature are listed in Table 31 and the thermal properties as a function of temperature are plotted in Figure 49 and Figure 50.

The embedded FISH programing in UDEC enables the users to define new variables and functions. By using FISH programing, minerals are randomly assigned and distributed in the model. The random number was drawn from uniform distribution between 0.0 and 1.0. The distinct material properties were assigned to each grain correspondingly. The mineral distribution in granite and gabbro numerical models is shown in Figure 51.

Table 30 Mineral composition of rocks (modified from Saiang (2011)).

Rock type	Quartz	Feldspar (plagioclase)	Pyroxene	Mica
Gabbro	-	55.8	27.6+8.1	5.5+3.0
Granite	32.0	59.4	-	7.2+1.4

Table 31 Mechanical and thermal properties of different minerals at room temperature.

	Quartz	Feldspar (plagioclase)	Pyroxene	Mica (Muscovite)
Density (kg/m^3)	2.65	2.63	3.26	2.79
Bulk modulus (GPa)	37.0	75.6	94.1	42.9
Shear modulus (GPa)	44.0	25.6	57.0	22.2
Thermal conductivity (W/m·K)	7.78	1.70	4.46	2.28
Specific heat (J/kg·K)	750	794	755	800
Linear thermal expansion coefficient (10^{-6}/°C)	8.095	3.528	9.267	11.790

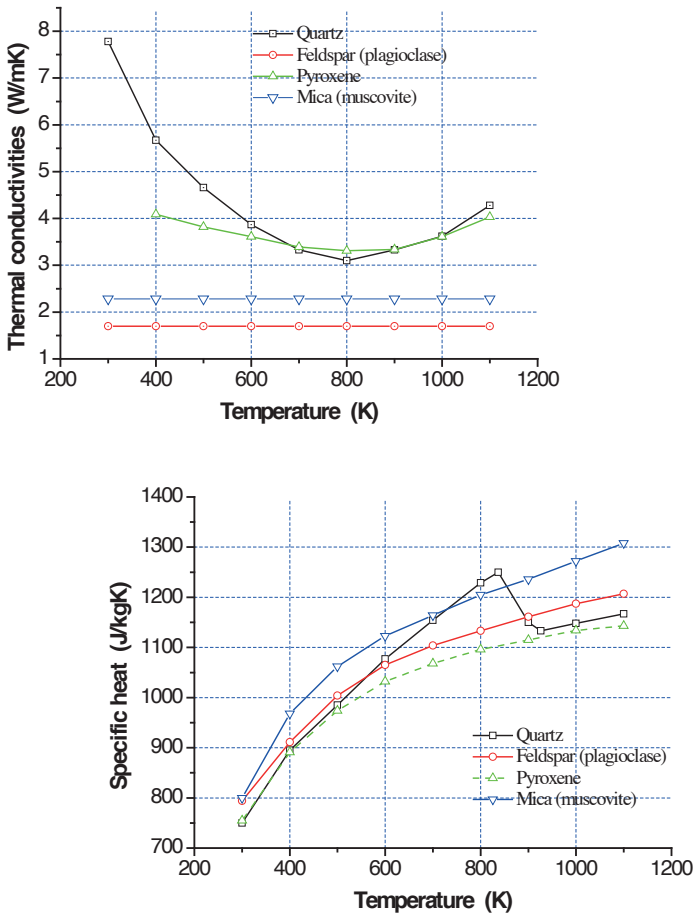

Figure 49 Thermal conductivity and volumetric specific heat as a function of temperature for different minerals.

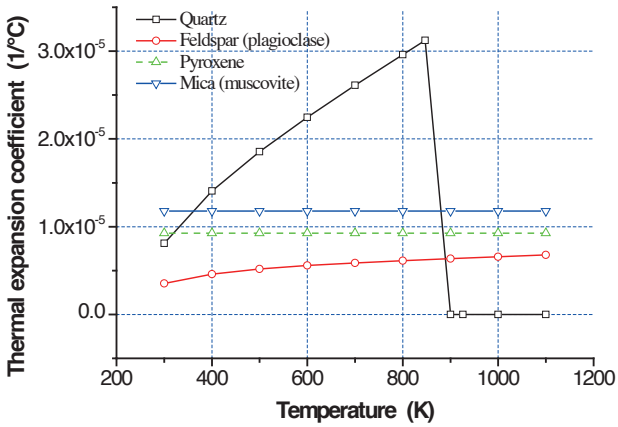

Figure 50 Linear thermal expansion coefficient as a function of temperature for different minerals.

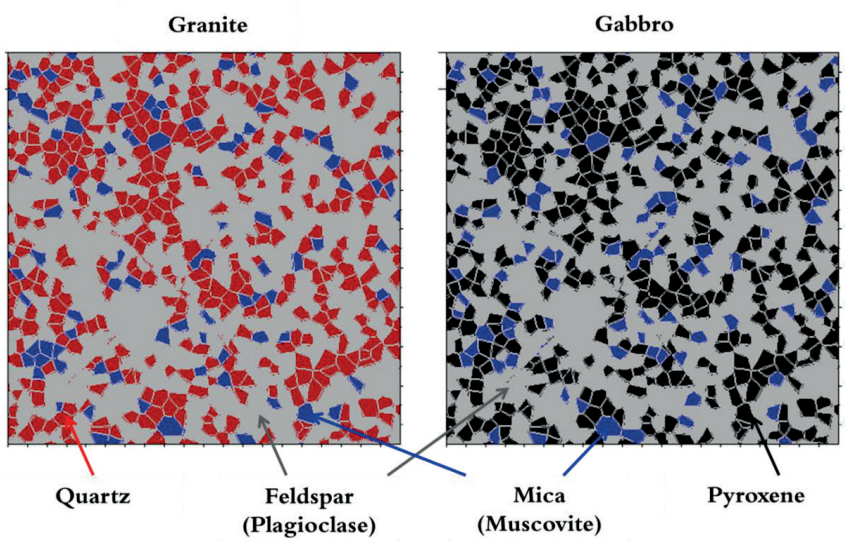

Figure 51 Mineral distribution in two numerical models.

5.3 Modelling procedure

The numerical model was calibrated through the model tunnel tests described in section 3.5. The modelling procedure is listed as follows.

- Model set-up
- Apply gravity and run the model until equilibrium is achieved
- Apply stresses on external boundaries and step to equilibrate mechanically
- Take thermal time steps
  - Change temperature of the air on the tunnel surface
  - Adjust thermal properties (thermal conductivity and specific heat) of different minerals according to their temperature
- Step to equilibrate mechanically
  - Adjust thermal expansion coefficients of different minerals according to their temperature
- Repeat steps 4 and 5 until sufficient time has been reached

5.3.1 RESULTS

Progressive damage process

The grain-based micromechanical model is capable of investigating the development of thermal induced fracturing by tracking the tensile and shear failure that occurred along the Voronoi block interface. The quantitative analyses of the micro-scale (grain scale) fracturing within the model provide insights into the damage process. This damage process is illustrated through a dry gabbro block under confined condition. Figure 52 to Figure 56 show the development of the temperature distribution and fracture propagation with time development. The sequence of plots shows the evolution from a fracture free pattern to fracturing along tangential direction of the opening surface and subsequent remote radial tensile fracturing development. By referring to Lan et al. (2013), the progressive damage process was divided into four stages: i) initial nucleation; (ii) initiation of the process zone; iii) progressive fracturing and iv) formation of stable geometry.

Stage I (Figure 52): This stage shows the distribution of grain-scale tensile fractures that occurred near the tunnel surface within a narrow region. The fracture initiates sparsely where thermally induced tensile stress is higher than the interface strength between grains. Since each grain represents a mineral and minerals with different modulus are randomly distributed in the model, this material heterogeneity brings heterogeneous stresses in the model during heating. Near the tunnel boundary, the temperature and temperature gradient are higher, which causes higher stresses and further fracturing.

Stage II (Figure 53): As the heating time increases, maximum temperature and temperature gradient becomes higher around the tunnel boundary. New grain-scale fractures initiate and some of them start to coalesce with previous created fractures and then form a large fractured zone. Dilation of these small scale fractures results in the formation of partially detached thin chips that are typically as thick as the grain size. The fractured zone associated with the

formation of these thin chips releases their stresses and transfers the superfluous stresses into the grains at deep locations. Since the tangential stress is tensile at deep locations, remote tensile fractures start to initiate.

Stage III (Figure 54): This stage is characterised by a high density of tensile and shear fracturing. The fracture interaction becomes stronger due to increased temperature and further increased stress magnitude. The high density of fractures in the process zone leads to an increase in the formation of thicker and longer slabs. Also, the remote tensile fractures become longer and propagate radially towards the model boundary. It is noted that the remote tensile fracture along the diagonal direction propagates much quicker than the others.

Stage IV (Figure 55 and Figure 56): During this stage, the development of fractures becomes very slow. Even the temperature still increases, the temperature gradient has slowed down. As can be seen from Figure 26, after 5 min's heating, the heating rate of the fire curves reduces significantly. It means the temperature increment along the tunnel boundary has reduced and it hence affects the temperature distribution within the numerical model. Furthermore, with the temperature increases, the thermal conductivity of minerals becomes lower and specific heat of minerals becomes higher, which means that there is less heat transfer from the heating boundary to the material inside due to the existing fractured zone. The fractures' distribution near the tunnel boundary becomes stable and the remote fracture along the diagonal direction reaches the model boundary. It is also noted that after the diagonal fracture has reached the model boundary, some other remote tensile fractures propagate quicker to the model boundary, especially the ones along vertical direction.

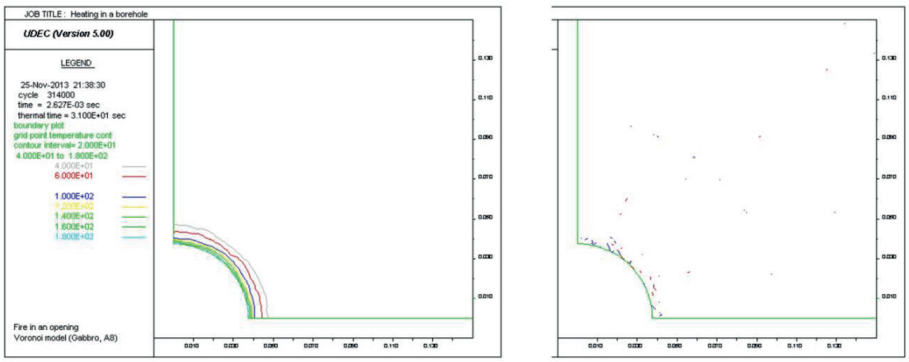

Figure 52 Temperature and fracture distribution at thermal time t =31 ms.

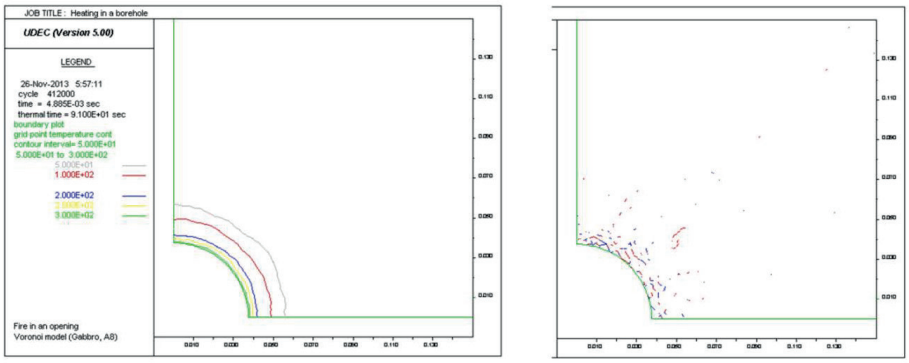

Figure 53 Temperature and fracture distribution at thermal time t =91 ms.

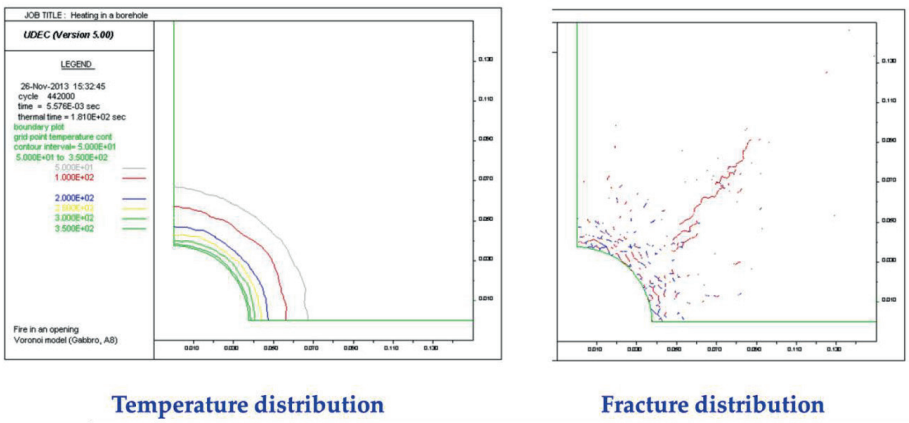

Figure 54 Temperature and fracture distribution at thermal time t =181 ms.

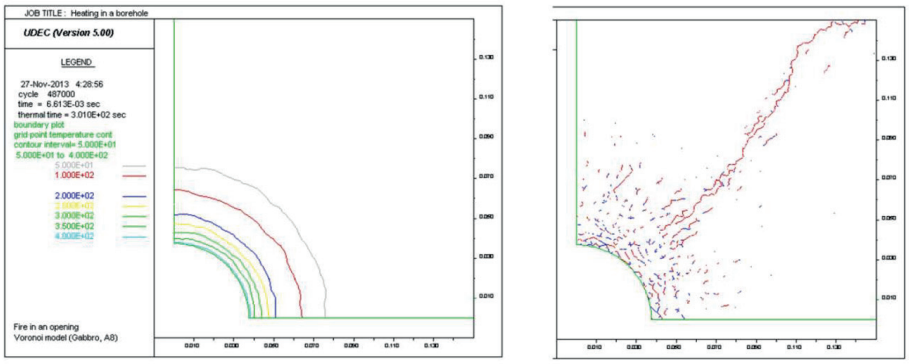

Figure 55 Temperature and fracture distribution at thermal time t =301 ms.

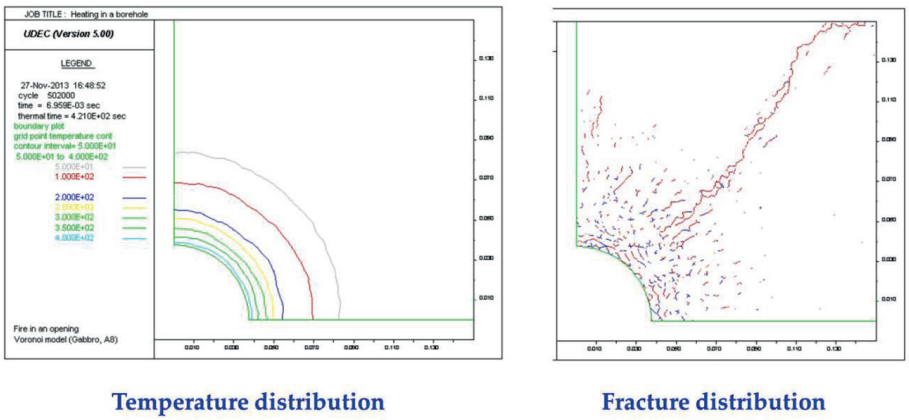

Figure 56 Temperature and fracture distribution at thermal time t =421 ms.

Effect of boundary condition

Figure 57 shows the numerical results of granite blocks both from free and confined boundary conditions. It is clear from the comparison in Figure 57 that the remote tensile fractures have been prohibited under confined boundary condition and the fractures are mainly concentrated near the tunnel boundary which has promoted more spalling events. These findings are very helpful to explain the difference observed from oven-dried granite blocks in the laboratory tests, see Table 27 and Figure 30. As can be seen in Table 27 and Figure 30, the oven-dried unconfined granite block (G8) showed only small chips detached from the opening boundary and much less spalling material than that from the confined granite block (G7).

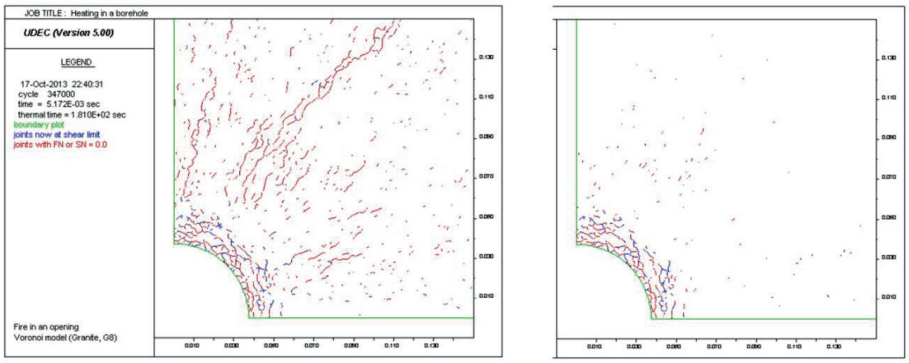

Figure 57 Comparison of fracture distribution under free and confined boundary conditions (Granites, oven-dried, t =181 ms).

5.4 Continuous model

5.4.1 MODEL DESCRIPTION

The continuous model presented in this section was also conducted using the geomechanical code, UDEC (5.0), developed by Itasca. The geometry of the numerical model is shown in Figure 48(a). The boundary conditions of the continuous model were the same as the discontinuous model, which was described in section 5.2.1. The model's features include

- 2D continuous model (Rock material is treated as homogeneous)
- Temperature-dependent thermal properties of rock
- Temperature-dependent mechanical properties (deformation and strength) of rock
- Thermal-mechanical coupling
- Dynamic thermal boundary condition
- Real temperature-time curve (Step function was programmed in order to simulate a continuous development of temperature with time)
- No evaporation of free moisture (Only dry rock block was simulated)

It should be noted that the dynamic thermal boundary condition was introduced in the continuous model in order to simulate the thermal boundary change on tunnel surface with respect to spalling. The dynamic thermal boundary condition was applied when the spalling failure criterion was satisfied at any zone. Then, the maximum temperature of the grid point of the zone was recorded by FISH function and the temperature of all grid points belonging to the zone was assigned the maximum value.

5.4.2 PARAMETERS

The thermal conductivity, thermal diffusivity and specific heat capacity of the rocks were determined as a function of temperature at temperature levels 20, 100, 300, 500 and 650°C by SP (Adl-Zarrabi, 2009). The measurements were performed with a TPS sensor of type 4922 with a radius of 14 mm. The measurement was repeated three times at each temperature level. The thermal expansion were determined at 100, 400, 600, 750 and 1050ºC with a set-up developed at SP for determination of thermal expansion of non-homogenous samples. The parameters of different rocks as a function of temperature are shown in Figure 58 and Figure 59. The parameters of granite and gabbro at room temperature are listed in Table 32.

The uniaxial compression test and Brazilian indirect tensile tests on rock samples at room temperature and after being heated at 400, 750 and 1100°C had been conducted by Saiang (2011). The Young's modulus, Poisson's ratio, UCS and tensile strength of different rocks were obtained by Saiang (2011).

Observations of brittle failure indicate that the brittle failure process involves the initiation, growth, and accumulation of micro-cracks. Continuum models with traditional failure criteria (e.g. Hoek–Brown or Mohr–Coulomb) based on the simultaneous mobilization of cohesive and frictional strength components have not been successful in predicting the extent and depth of brittle failure. Cohesion weakening and frictional strengthening (CWFS) model as function of rock damage or plastic strain has shown its advantage in simulating brittle failure of rock (Hajiabdolmajid et al., 2002). Zhang et al. (2009) established a micromechanical model which can capture the bond breakage and frictional resistance mobilization and the evolutionary law of cohesive and frictional strength components with their reversible strains was determined using the model. As can be seen from Figure 60, the evolution of cohesive strength and frictional strength with irreversible (plastic) strain is very complex. Martin and Christiansson (2009) proposed a simplified methodology as follows to simulate mechanical spalling by using traditional Mohr-Coulomb failure criterion and suitable peak and residual strength parameters in numerical models.

This criterion uses a Mohr–Coulomb failure envelope with the peak friction angle (ϕ_p) set to zero, to indicate that the strength of the rock is entirely cohesive and the peak cohesion (c_p) of the rock set to 1/2 the spalling rock mass strength. Once spalling occurs and the slabs form, the strength of the broken rock slabs is mainly frictional and hence the residual cohesion (c_r) is set to a nominal 5 MPa reflecting the small strain nature of the problem, and the residual friction angle (ϕ_r) is set to 45° (see Figure 61). The peak tensile strength goes to zero once spalling initiates.

In our analysis, the simplified methodology was chosen but only peak strength parameters were used (see values in brackets in Table 32). In order to consider the scale effect of rock strength, an amplification factor of 1.6 was used for determining the mechanical parameters in the numerical modelling, see values in Table 32. The parameters and derived parameters as a function of temperature are shown in Figure 62 and Figure 63. The parameters of granite and gabbro at room temperature are listed in Table 32.

Table 32 Mechanical and thermal properties of two rocks at room temperature

Rock type	Granite	Gabbro
Density (kg/m3)	2.60	2.93
Bulk modulus (GPa)	47.4	63.8
Shear modulus (GPa)	25.7	36.5
Thermal conductivity (W/m·K)	3.82	2.55
Specific heat (J/kg·K)	827	962
Linear thermal expansion coefficient (10^{-6}/°C)	0.576	0.670
Cohesion (MPa)	185.1 (115.7)	155.2 (97.0)
Tensile strength (MPa)	26.7 (16.7)	33.8 (21.1)
Friction angle (°)	0	0

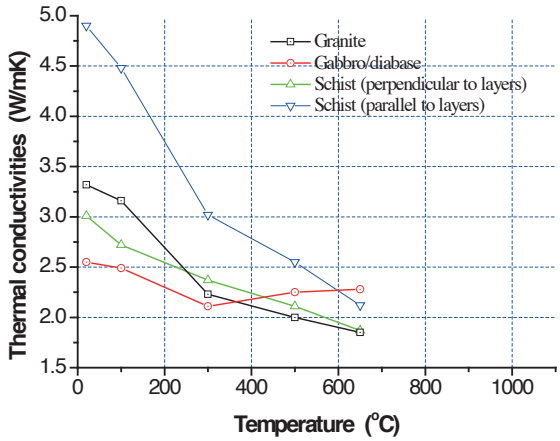

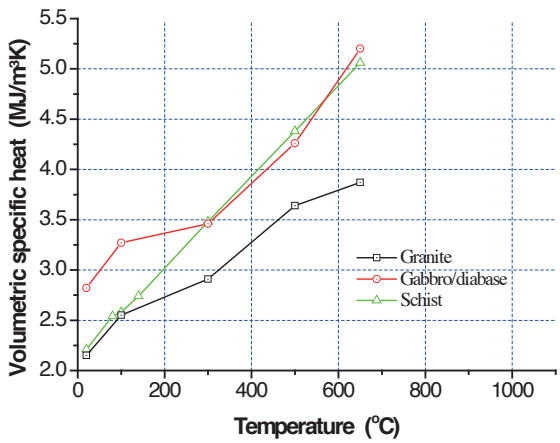

Figure 58 Thermal conductivity, volumetric specific heat as a function of temperature for different rocks.

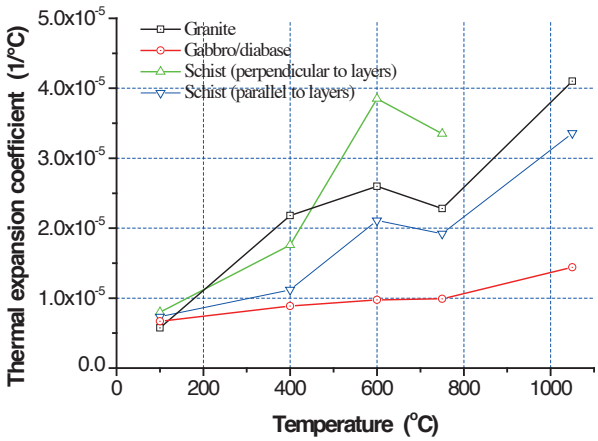

Figure 59 Linear thermal expansion coefficient as a function of temperature for different rocks.

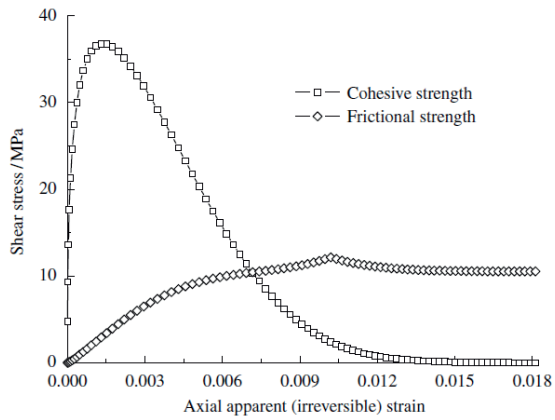

Figure 60 Evolution of cohesive strength and frictional strength with irreversible (plastic) strain (Zhang et al., 2009).

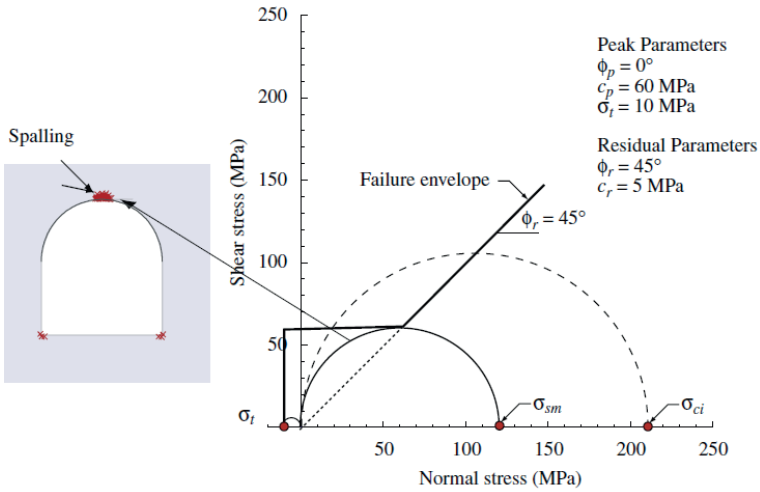

Figure 61 The spalling-failure criterion (Martin and Christiansson, 2009).

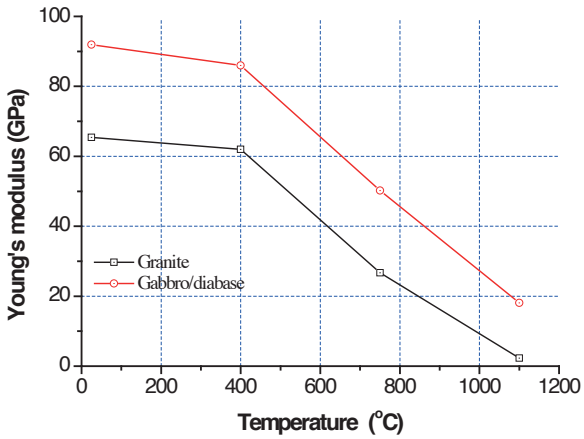

Figure 62 Young's modulus as a function of temperature of two rocks.

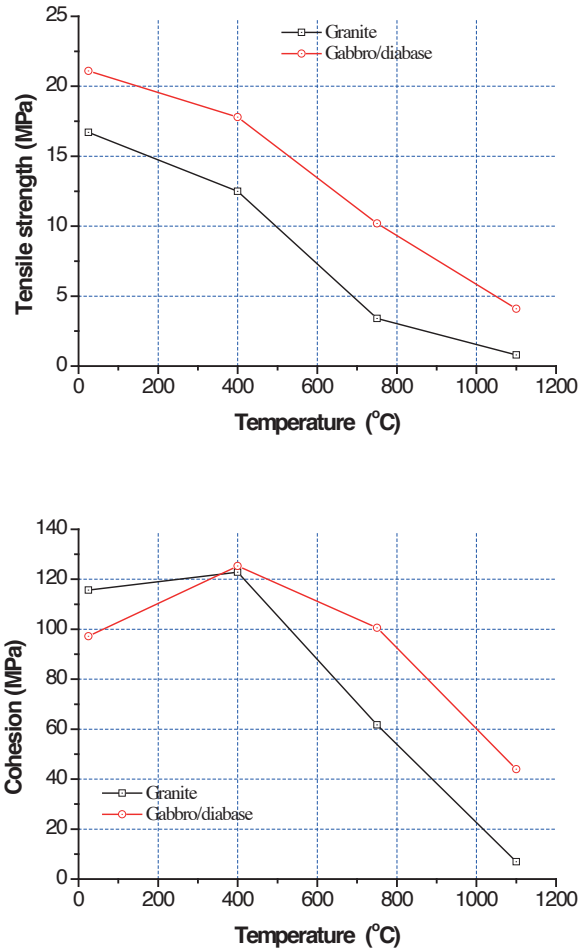

Figure 63 Tensile strength and cohesion as a function of temperature of two rocks.

5.4.3 MODELLING PROCEDURE

The numerical model was calibrated through the model tunnel tests described in section 3.5. The modelling procedure is listed as follows.

- Model set-up
- Apply gravity and step to equilibrate mechanically
- Apply stresses on external boundaries and step to equilibrate mechanically
- Take thermal time steps
  - Change temperature of the air on the tunnel surface

  - Adjust thermal properties (thermal conductivity and specific heat) according to the temperature
  - Adjust the temperature in a failed zone
- Step to equilibrate mechanically
  - Adjust thermal expansion coefficient according to the temperature
  - Adjust bulk and shear modulus according to the temperature
  - Adjust strength parameters according to the temperature
- Repeat steps 4 and 5 until sufficient time has been reached

5.4.4 RESULTS

Progressive damage process

The continuous model normally does not have the capacity to simulate the fracture initiation and propagation explicitly, and it is very common to use some indicators to represent this process. Therefore, the plastic region is chosen here as an indicator to investigate the progressive damage process. This damage process is illustrated through a dry granite block under confined condition. The development of the temperature distribution and plastic region with time development is shown in Figure 64 to Figure 68. Similarly, the progressive damage process was divided into four stages: i) initial nucleation; (ii) initiation of the process zone; iii) progressive fracturing and iv) formation of stable geometry.

Stage I (Figure 64): This stage shows the initiation of fractures occurred near tunnel surface within a narrow region. The fractures initiate where thermally induced tensile stress has reached the strength of rock. Since the material is homogeneous and the thermal load is uniformly applied on the tunnel boundary, the temperature distribution is uniform in the model and the observed plastic regions are also uniformly distributed along the tunnel boundary.

Stage II (Figure 65): As the thermal time increases, the maximum temperature and temperature gradient become higher around the tunnel boundary. New plastic regions appear and the depth of the plastic regions increases, which indicates that a large fractured zone has formed.

Stage III (Figure 66): This stage is characterised by a high density of tensile and shear fracturing near the tunnel boundary. The high density of fractures in the process zone leads to an increase in the formation of the plastic regions. Also, the remote tensile fracture appears and propagates radially towards the model boundary. It is very clear that the remote tensile fracture initiates at a certain point which is far away from the tunnel boundary and where the tensile stress has exceeded the tensile strength of the rock. It is also noted that the remote tensile fracture propagates along the diagonal direction in the model.

Stage IV (Figure 67 and Figure 68): During this stage, the development of the plastic regions becomes slow. The distribution of the plastic region near the tunnel boundary becomes stable and the remote fracture along the diagonal direction has reached the model boundary. The same explanation can be found in section 5.2.4. It is also noted that after the diagonal fracture has reached the model boundary, some other fractures appear and mainly propagate along a

horizontal direction. It should be emphasized that the temperature distribution is not uniform any more in the model due to the use of dynamic boundary condition in the modelling. It is very clear that the temperature along the vertical direction of the tunnel roof is much higher than that along the horizontal direction of the tunnel sidewall since more plastic regions (spalling material) have occurred on the roof.

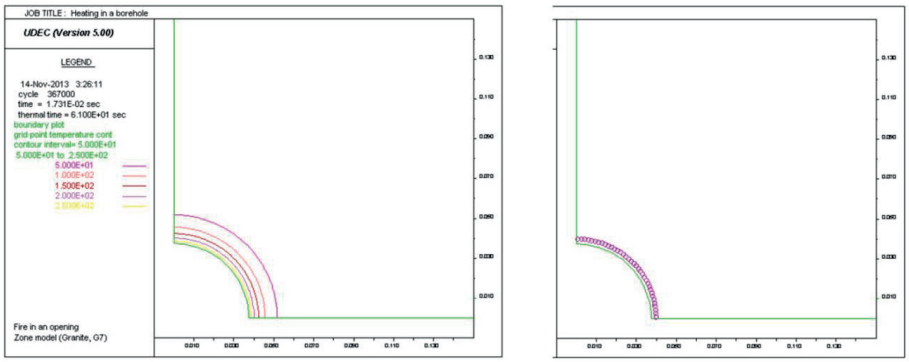

Figure 64 Temperature distribution and plastic region at thermal time t =61 ms.

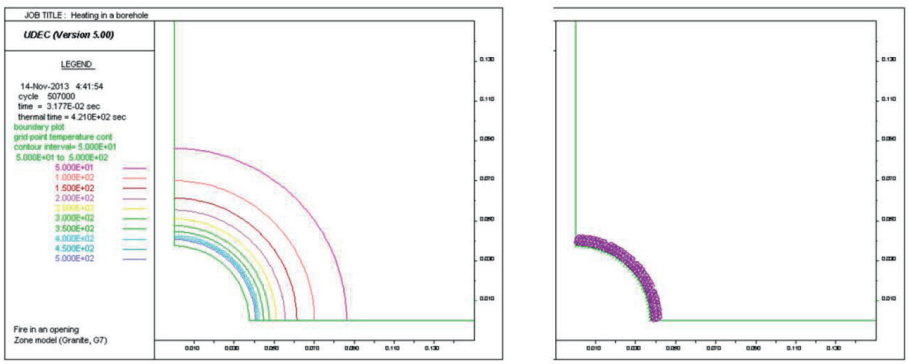

Figure 65 Temperature distribution and plastic region at thermal time t =421 ms.

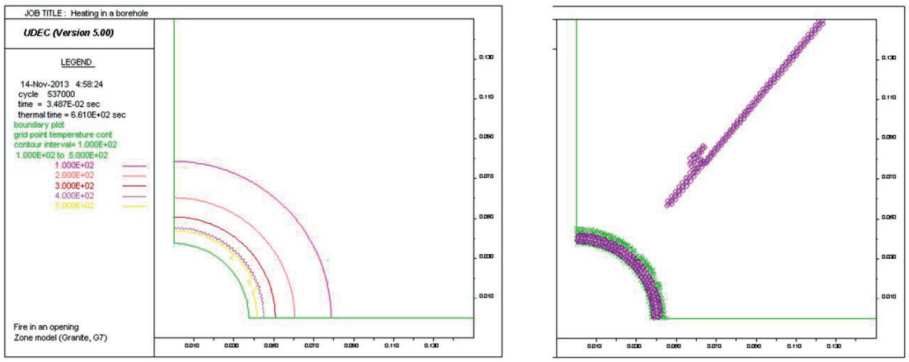

Figure 66 Temperature distribution and plastic region at thermal time t =661 ms.

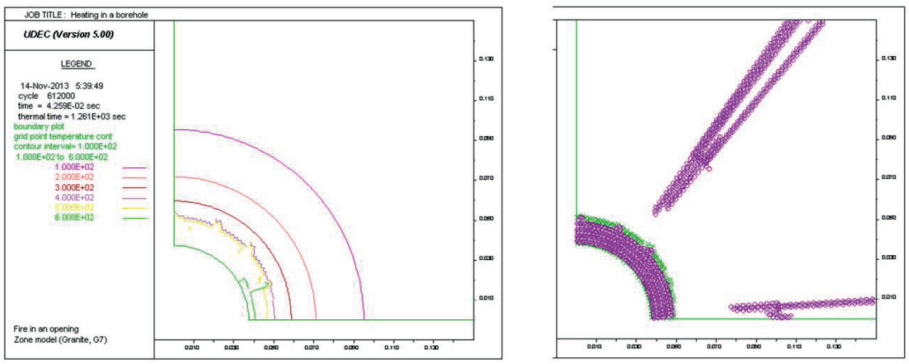

Figure 67 Temperature distribution and plastic region at thermal time t =1261 ms.

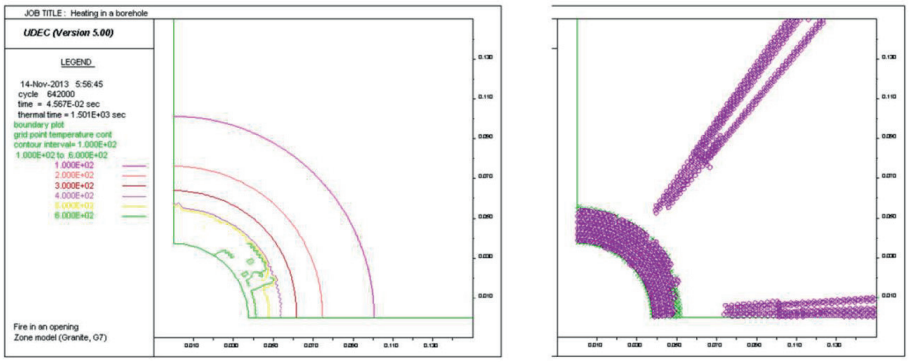

Figure 68 Temperature distribution and plastic region at thermal time t =1501 ms.

Figure 69 shows the stress distribution with time development. The sequence of plots can further explain how the damage process develops. At the beginning of heating, there is a large stress concentration around the tunnel boundary which will lead to yield of rock (spalling). After rock is yielded near the tunnel boundary, their properties start to deteriorate and then rock in the plastic region carries a lesser load. The stress starts to transfer from near tunnel surface to inside the rock block and subsequently create more plastic regions and increase the depth of the plastic regions. Also, there is tensile stress along a circumferential direction located a little far from the tunnel boundary which causes remote tensile fractures in the physical model.

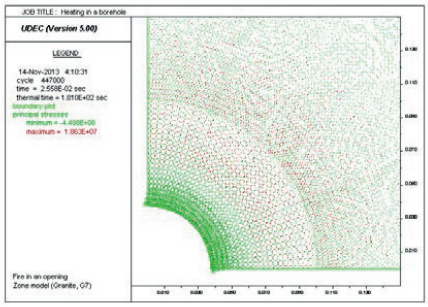

(a) t =181 ms

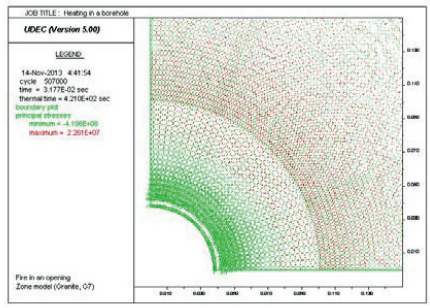

(b) t = 421 ms

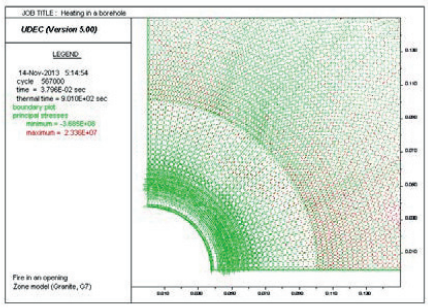

(c) t =901 ms

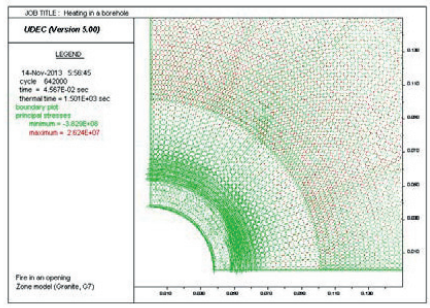

(d) t = 1501 ms

Figure 69 Stress distribution with time development.

Effect of boundary condition

Figure 70 and Figure 71 show the numerical results of granite blocks both from free and confined boundary conditions at thermal time t = 241 ms and t = 1501 ms. For comparison, Figure 72 shows the tunnel boundary after spalling and fracture pattern on the front surface of the model tunnel tests of the granite blocks under free and confined boundary conditions at thermal time 1501 ms. It is clear from the comparison in Figure 70 and Figure 71 that the remote tensile fractures have been prohibited under confined boundary conditions and the fractures at the beginning of heating (t =241 ms) are mainly concentrated near the tunnel boundary which has promoted more spalling events. These findings are very helpful to explain the difference observed from oven-dried granite blocks in the laboratory tests, see Figure 72. As can be seen in Figure 72, the oven-dried unconfined granite block (G8) showed only small chips detached from the opening boundary and much less spalling material than that from the confined granite block (G7). It should be also pointed out that there is a large difference between the laboratory test and numerical model under free boundary conditions at t =1501 ms. This difference is mainly caused by using a continuous numerical modelling technique. If there is not any confinement in the physical model, the stress will release when remote tensile fractures occur and propagate into the tunnel boundary. It then causes much less compressive stress concentration along the tunnel boundary, which of course will produce

much less spalling materials. This explains why there is less spalling material for tested granite block under free boundary conditions. However, the continuous numerical model does not have the capacity to simulate the stress release due to initiation and propagation of remote tensile fractures and hence the large difference compared with the laboratory tests under free boundary condition.

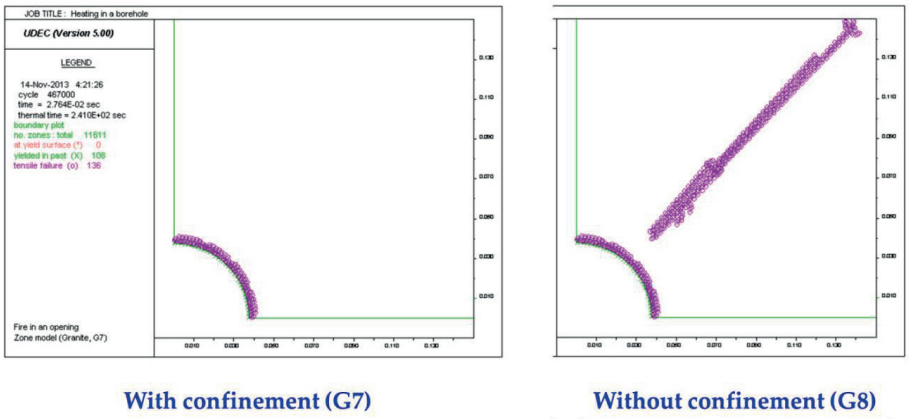

Figure 70 Comparison of plastic regions under free and confined boundary conditions (t =241 ms).

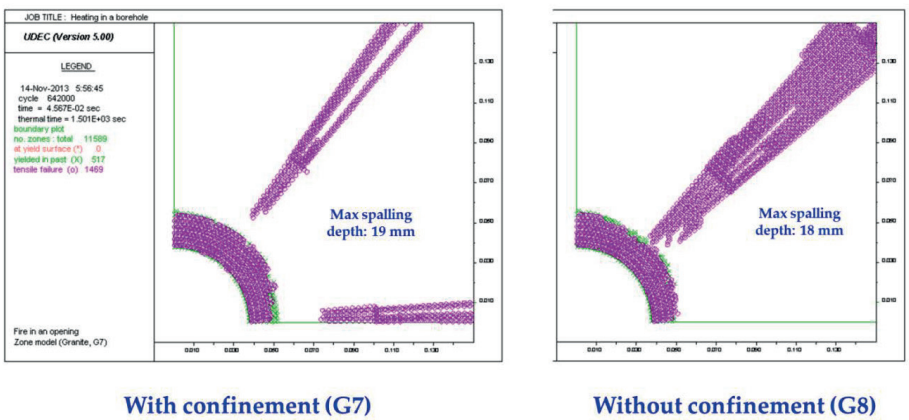

Figure 71 Comparison of plastic regions under free and confined boundary conditions (t =1501 ms).

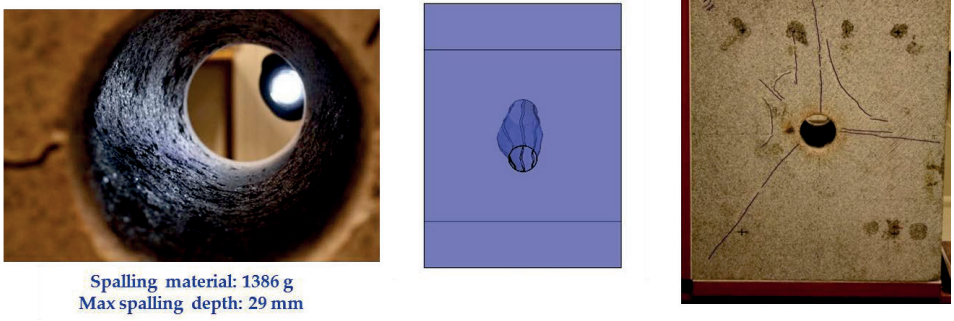

(a) Confined boundary condition (G7)

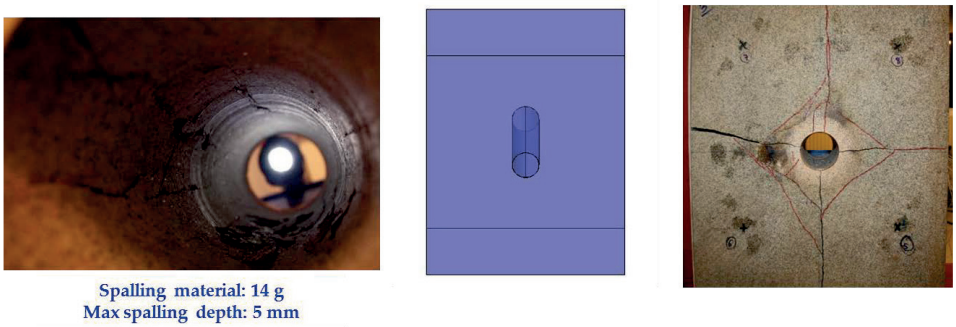

(b) Free boundary condition (G8)

Figure 72 Comparison of laboratory test results under free and confined boundary conditions (granite, t =1501 ms).

6 DISCUSSION

6.1 Heating of core-based specimens

The saturation of the rock samples in water did not show any difference in results, especially for the granite and gabbro both during the heat treatment as well as in the mechanical tests. This is because these rock types have low porosity which hinders water permeating the rock samples. On the other hand schist samples showed some variation in the results, which is due mainly to its foliated nature. Since the schist samples were loaded in two orientations, perpendicular and parallel to the foliation plane, the differences in results were also due to the orientation of the foliation plane to the loading axis. Schist samples with foliation plane perpendicular to loading axis showed higher strength value compared to the schist samples loaded parallel to the foliation plane.

6.1.1 MECHANICAL PROPERTIES

The notable changes observed in the mechanical properties of the rocks with the increase of the heat treatment temperature level are summarized and presented here.

Compared to the compressive strength of the gabbro in its unheated (original) state, the compressive strength of gabbro when heat treated at 400°C increased by 22 %. At the 750°C level the compressive strength value was still slightly higher, by 3% than that of the gabbro in the unheated state. At the 1100°C temperature level, a very significant rapid decay in the compressive strength is observed with a 55% decrease compared to the uniaxial compressive strength of the gabbro at its original state. The elastic modulus of the gabbro decreased stepwise with the increase of the temperature while the Poisson's ratio of gabbro was seen to increase. The most significant change observed for these properties of gabbro are at the temperature levels 750°C and 1100°C.

As for granite the compressive strength was observed to increase only slightly at the 400°C, which may not be a significant enough change in behaviour to draw any subsequent conclusions. However, at 750°C and 1100°C, significant decreases in the uniaxial compressive strengths of granite are observed. At 1100°C, granite had lost 94% of its uniaxial compressive strength compared to its compressive strength in its original state. The elastic modulus of granite at 400°C showed only a slight decrease while more significant increases of the elastic modulus of granite were observed at 750 and 1100°C implying significant loss in elasticity at 750°C and 1100°C.

The compressive strength of schist was observed to increase quite significantly at 400°C and at 750°C schist still exhibited a higher compressive strength compared to gabbro and granite. However, at 1100°C the decrease in compressive strength is very rapid. A notable increase is observed in the elastic modulus of the schist at 400°C, which correlates to the significant increase in the compressive strength. A rapid decrease is observed in the elasticity of schist at 1100°C which correlates with the rapid decrease in compressive strength.

6.1.2 MINERALOGICAL COMPOSITION

The mineralogical changes that occurred in the heat treated rock samples as a result of the increase in temperature were manifested by distinctive colour changes with the increasing temperatures. It was observed that the colour change in the rocks increased in intensity with

the increase of the temperature levels and is due to the mineral transformation and phase changes of the minerals. It is primarily the Fe bearing minerals such as the mica (biotite), olivine and pyroxene that appear to be more sensitive to the increase in temperature. The most intense colour change is attributed to the oxidation iron bearing minerals.

Gabbro which composed mainly of plagioclase, pyroxene, olivine and biotite with apatite, calcite, amphibole (hornblende), ilmenite and Fe-oxide (magnetite) occurring as accessory minerals showed significant evidence of being sensitive to mineralogical alterations as a result of the increase in temperature. As seen from the analyses, the main mineralogical changes as a result of the temperature increase in gabbro include the decrease in the mica, olivine and pyroxene content. Olivine and mica minerals showed significant decrease in amount after heat treatment at 400°C. After heat treatment at 750°C, no mica and olivine mineral could be detected in gabbro using the polarizing microscope. This is also the case after heat treatment at 1100°C. Unlike the olivine and mica, pyroxene did not show any significant change at the 400°C temperature level but showed a marked decrease after heat treatment at 1100°C. Parallel to the decrease in the content of olivine, mica and pyroxene a step-wise increase is observed in the content of other phases. These mineral phases defined as other phases could not be identified using the polarizing microscope. They were, therefore, loosely classified as opaque minerals and could not be adequately identified. Using the SEM/EDZ method, the other phases were identified to compose mainly of ilmenite and magnetite. The presence and increase in content of these other phases suggest that these mineral phases are a result of the transformation and/or phase transition of the olivine and mica which after heat treatment at 750°C appear to be extinct in gabbro. A Fe-Ti-Mg rich phase which corresponds by its chemical composition to alloys rather than to minerals is identified in gabbro after heat treatment at 1100°C. This Fe-Ti-Mg rich phase was observed to originate from pyroxene close to the ilmenite and/or magnetite phases. This indicates the reason for the marked decrease of pyroxene at 1100°C which transformed into the Fe-Ti-Mg rich alloy phase.

The granite is in its original state composed mainly of feldspars (alkali feldspar>plagioclase), quartz and biotite with apatite, zircon, ilmenite and Fe-oxides occurring as accessory minerals. With increase in temperature, the amount of biotite decreased and the amount of other phases increased Fluorite and calcite were observed in accessory amounts in granite heated to 400°C while Ti-Fe-Mg phase corresponding by its chemical composition to alloys instead of mineral is observed in granite heated 750°C. For granite heated to 1100°C, K feldspar and biotite which had minor amounts of Na2O included are observed. Also allanite, epidote and aluminocerrite were observed in accessory amount only in granite at 1100°C. With the increase of the heat treatment temperature level the mineralogical changes in granite showed similar trends to that observed in gabbro. The marked change being the decrease in the mica content and simultaneous increase in the content of other phases with the increasing temperatures. The content of feldspar and quartz, the dominant minerals, showed only slight changes with the increasing treatment temperature and without any regular pattern so it is not obvious whether these changes are directly related to temperature increase while the mica mineral showed significant decrease in amount as a result of the temperature increase indicating the decrease as a direct influence of the increase in the heat intensity. As observed in gabbro there was a marked decrease in the amount of mica at the 400°C temperature level. After treatment at 750 and 1100°C temperature levels mica was significantly reduced and as such was observed to be absent in granite at the aforementioned temperature levels. Similar to the gabbro observations there was a parallel step-wise increase in the content of the other phases with the increasing temperature levels. The other phases present in granite composed

mainly of apatite, zircon, ilmenite Fe-oxide (magnetite), fluorite, calcite and Ti-Fe-Mn- rich phase corresponding by its chemical composition to alloys rather than to minerals. The Ti-Fe-Mn- rich phase in granite was observed to partially fill the micro-cracks in mica (biotite).

The schist samples are mainly composed of quartz, biotite and minor amount of feldspars. Allanite, epidote, sphene, zircon and Ti-rich magnetite make-up the other phases observed in schist. The significant mineralogical observation in schist with the increasing temperature levels is the increase in the amount of the other phases with the increasing temperatures.

6.1.3 MICRO-CRACK DISTRIBUTIONS

From the micro-crack analyses, it can be seen that the micro-crack distribution increases with increasing temperature. In gabbro, a marked increase in the micro-crack distribution is observed in all of the constituting minerals. Micro-cracks were identified in the mineral grains of the other phases using the SEM/EDS method but micro-crack distribution analysis was not performed because the mineral grains were below the resolution limit of the polarizing microscope. It can also be stated that the higher the temperature level, the minerals exhibit a higher micro-crack distribution and as such the highest micro-crack distribution in the minerals is exhibited by rock samples subjected to the highest temperature level. A significant change in the micro-crack distribution in gabbro is the micro-crack distribution of the pyroxene mineral at the 1100°C temperature level. After treatment at 1100°C the micro-crack distribution of the pyroxene mineral showed a 77% increase compared to the micro-crack distribution of the gabbro in its unheated (original) state. This is particularly noteworthy when comparing the micro-crack distribution of the two lower temperature levels, 400 and 750°C. The increase in the micro-crack distribution of the pyroxene mineral at 400 and 750°C are 33 and 43 % respectively. The micro-crack distribution change in pyroxene mineral is also significant because it coincides with the formation of the Fe-Ti-Mg-rich phases (which corresponding to its mineral composition is classified as an alloy rather than a mineral) observed in gabbro. This alloy phase as already stated (in the mineral composition analysis summary) originates from the pyroxene mineral grains and therefore, indicates a relationship between the mineralogical change and the micro-crack distribution change in pyroxene at the 1100°C temperature level. In granite a more regular pattern of increase in the micro-crack distribution is observed in feldspar, quartz and mica with the increasing temperature. However, as noted in the mineral composition results analyses summary, the Ti-Fe-Mn-rich alloy phase identified in granite was observed to partially fill the micro-cracks in the mica mineral. For schist, the micro-crack distribution was able to be performed only on quartz which shows a regular increase with the increase in temperature.

6.2 Block tests

6.2.1 EFFECT OF ROCK TYPES ON THERMAL SPALLING

The photographs of the heated surfaces of these three blocks after the locally and uniformly heated tests are shown in Figure 29 and

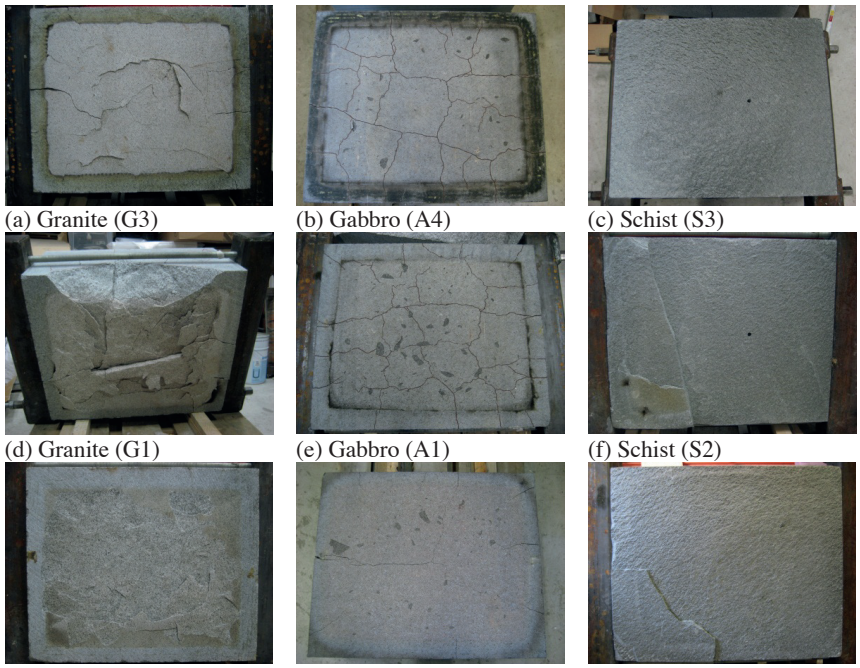

(a) Granite (G3) (b) Gabbro (A4) (c) Schist (S3)

(d) Granite (G1) (e) Gabbro (A1) (f) Schist (S2)

(g) Granite (G2) (h) Gabbro (A3) (i) Schist (S1)

Figure 73. It is clear that there is great difference in spalling behaviour among the three tested rock types under different conditions.

When heating a multi-mineral or poly-crystalline rock, internal thermal stresses may develop due to variation in thermal and mechanical properties. As it is shown in Table 1, the tested granite, gabbro and schist contain different minerals with different coefficients of thermal expansion. Thermal stresses can be theoretically evaluated for a spherical quartz grain embedded in a feldspar matrix. In absence of external stress, a temperature rise of 200 ºC can lead to radial stress σ_{rr} =100 MPa and a tangential stress of $\sigma_{\theta\theta}$ =-50 MPa (tensile) (Hettema, 1996). If the tangential stress exceeds the tensile strength of the matrix, a tensile fracture will be initiated. That is why the initiation and propagation of thermal fractures can be seen in all three rock types during heating. However, thermal fractures can occur in any directions around a mineral grain, and they do not necessitate sudden removal of surface material, i.e. thermal spalling.

Except thermal fractures, the granite shows substantial explosive spalling characterized by a sudden forcible separation and a loud noise. As it is shown in Table 1, the tested granite contains different minerals and is rich in quartz. Since quartz has a much larger coefficient of thermal expansion than the other minerals of the granite, it induces great thermal stress between mineral grains. Furthermore, the blocks were heated on one side in our tests, therefore it must be realized that compressive stresses will develop parallel to the surface due to temperature gradient perpendicular to the heated surface. Only cracks with an orientation parallel to the heated surface will hence be able to grow. The surface buckling may increase as the flaw extends and the spall may finally bend up violently (see Figure 74) (Preston and

White, 1934). For this reason, the spalling for granite presents a continuous process and is repeated as long as the conditions are met.

The tested gabbro consists almost entirely of plagioclase feldspar and lacks quartz (see Table 1), and hence the thermal stresses due to differences in thermal expansion between minerals were largely reduced on the heated surface during heating. Therefore, only surface pitting occurs.

The tested schist is composed of a laminate of two materials with different thermal expansion coefficients. According to the bi-crystal model proposed by Kingery et al. (1976), the shear stress can develop at the interface. If the interfacial bond strength between the layers is high compared to the tensile strength of the layer, the development of extension fractures is favoured (shown in layer B in Figure 75). If the interfacial bond strength is relatively low or if the layers are relatively thick, shear fractures at the interface are more likely to occur. In our tests, although the interfacial bond strength and tensile strength of the layer were not tested, the relative movement along the failed interface (Figure 27(a)) and pulverized material (Figure 27(d)) was found on the delaminated interface. It shows that there was large shear stress on the interface during heating and the blocks failed in sliding along layers.

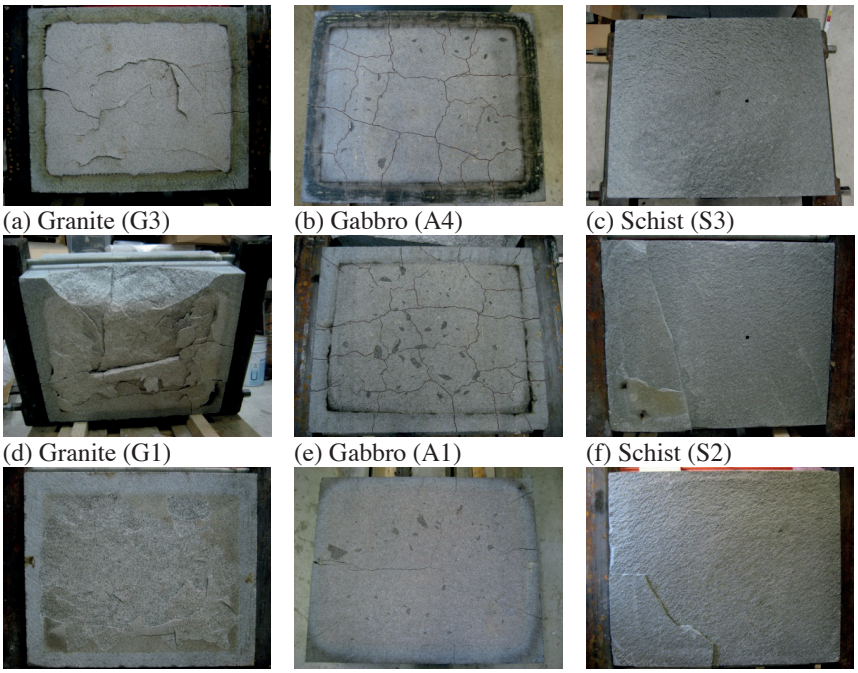

Figure 73 Comparison of exposure surface among three rocks under uniform heating (a)-(c) for oven-dried blocks; (d)-(i) for water-stored blocks.

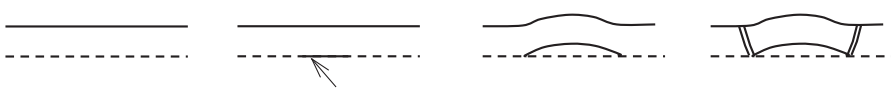

Figure 74 Chain of events which could lead to spalling by compression (Preston and White, 1934).

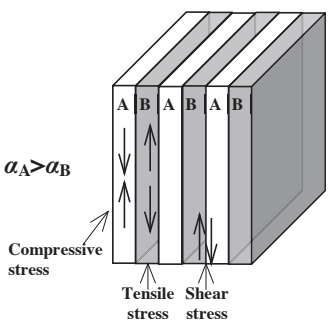

Figure 75 The bi-crystal model.

6.2.2 EFFECT OF WATER ON THERMAL SPALLING

Although the water content (0.2%) was very low for granite, the water-stored granite still presented more intensive spalling behaviour and produced more spalling material than the oven-dried granite in the uniformly heated tests and the model tunnel tests, see

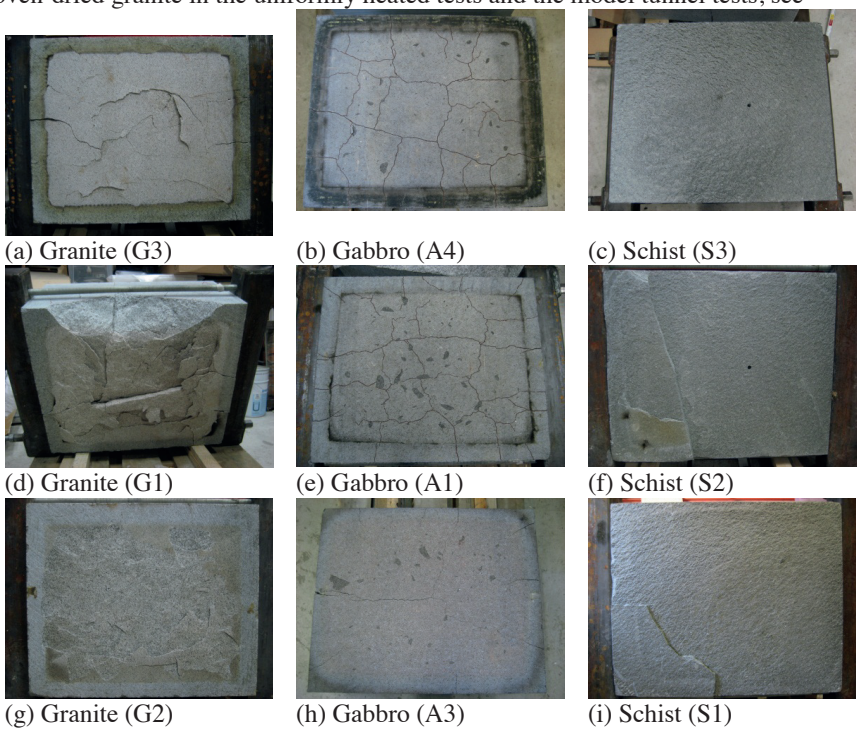

(a) Granite (G3) (b) Gabbro (A4) (c) Schist (S3)

(d) Granite (G1) (e) Gabbro (A1) (f) Schist (S2)

(g) Granite (G2) (h) Gabbro (A3) (i) Schist (S1)

Figure 73, Table 24 and Table 27. The mechanism causing more spalling could be primarily due to the generation of pore (air, vapour, liquid water) pressure during heating.

Another interesting finding was that the spalling depth for oven-dried and water-stored granite did not differ significantly after the heat-exposed surface of the oven-dried granite block was scaled (see Table 25). This indicated that the spalled pieces of the oven-dried granite detached from the rock matrix but without falling into the furnace. Thus, it can be deduced that restrained thermal expansion induces surface buckling and later heat-induced pore pressure completes spalling violently for water-stored granite. In this spalling process, pore pressure plays a minor role since the tested rocks are hard and have low porosity and water content. This inference can also be supported from the pore pressure measurement in fire-exposed concrete. According to some fire test results on concrete blocks, the maximum steam pressure measured is low (less than 1 MPa) compared to the normal tensile strength of concrete (Jansson et al., 2010; Mindeguia et al., 2010). Bazant (2005) has proposed that the pore pressure alone cannot cause explosive spalling. If the pore pressure is involved, the role may be only as a trigger, i.e. the pressure leads to a slight deformation that initiates the process of thermal stress induced brittle fracture and delamination buckling. This explanation further

helps us to understand why the water-stored granite and gabbro blocks produced more spalling material than that of oven-dried blocks in our tests, but definitive proof of the role of pore pressure needs to be studied in the future.

Furthermore, the thermal fractures occur on all tested rock blocks due to thermal heterogeneities of rock minerals and temperature gradient, and hence vapour could easily escape through these fractures and further release the pore pressure. Figure 76 shows that vapour in a water-stored gabbro block flowed out through thermal fractures and then disappeared at free surface.

(a) (b) (c)

Figure 76 Steam flow process along the outer surface of gabbro block.

6.2.3 EFFECT OF INITIAL COMPRESSIVE STRESSES ON THERMAL DAMAGE

The application of initial compressive stresses on the rock blocks during heating has a twofold effect. First, when the rock block is confined, the amount of tensile stress is reduced during heating and hence the thermal fractures appear later than for the blocks without confinement. Correspondingly, the fracturing itself is restrained and the propagation of the fractures slows down Secondly, the quantity of compressive stress near the opening boundary is increased during heating, and the spalling is greatly promoted in an extensive and explosive manner resulting in large amounts of spalling material.

6.2.4 EFFECT OF FIRE TYPES ON THERMAL SPALLING

Although the surface temperature followed the same temperature-time curve between uniformly and locally heated tests, the quantity of heat input was less under locally heated tests. Therefore, the thermal spalling induced by local heating was limited at the heated area and the destructive effect was further decreased.

When the fire is widespread, the steam front can generate and propagate perpendicular to the heated surface. Pore pressure might then be an important factor on thermal spalling. However, the pore pressure can easily dissipate due to the locally heated area when there is a localized fire. That is why there is not any large difference between oven-dried and water-stored rocks under local heating test.

6.2.5 EFFECT OF MODEL SIZE AND MODEL BOUNDARY

Researchers using physical model studies have identified three types of fractures around circular openings: tensile or primary fractures, remote or secondary fractures and sidewall fractures (spalling or breakout) (e.g. Carter, 1992; Martin et al., 1994). However, the remote or secondary fractures were only found in laboratory tests when the circular opening is small (e.g. less than 62 mm). Also, Martin et al. (1994) compared the borehole breakouts both from the laboratory and field tests and pointed out that a strength-scale effect is strongly evident for boreholes that have a diameter of less than 75 mm and increases with decreasing diameter. For boreholes with a diameter greater than 75 mm, the laboratory strength of the rock around the borehole approaches the UCS of the intact rock. Based on their investigation, in order to reduce the strength-scale effect, a 75 mm diameter of borehole was chosen in our test to simulate a ‘rock tunnel’. However, as can be seen from both the laboratory tests and the numerical analyses, the remote tensile stress and fractures appear in both cases. Martin (2013) pointed out that this type of fracture could be affected by the size of the model and the model boundary and that applying the laboratory results to real projects should be done with great caution. Whether the remote tensile fractures are caused by model size or model boundary need to be further investigated by numerical modelling with larger model size.

6.3 Acoustic emission

6.3.1 UNIFORM HEATING

The comparison between the AE activity rate, magnitude, type, and spatial distribution in different types of rocks and in the same type of rock but different conditions (saturated and dry) showed that some trends can be identified. Most of the discussion is based on the results

from the tests with 25-minutes heating as the comparison between these results is more straightforward.

After the heating started in some blocks the AE activity rate increased slowly (saturated gabbro (A1 and A3) and in dry granite (G3)) while for the rest of the blocks the AE activity started with a sudden sharp step. This was especially pronounced for schist where the AE activity reached the maximum within 2-3 minutes after the heating started when the oven temperature was ~750°C. In contrast for gabbro and granite the AE rate increased to the maximum in about 15 minutes after the heating started when the oven temperature was about 1000°C.

In overall the maximum rate of AE was highest for gabbro and lowest for schist. There were differences between the maximum rate for the blocks of the same type with different conditions - dry or saturated. For all three types of rocks in overall the maximum rate was lower for saturated blocks then for dry ones.

If we compare the total and maximum numbers between different types of rocks but with similar conditions – saturated or dry, it can be seen that the total number of AE events and the maximum rate was highest for gabbro and lowest for schist. For the blocks heated for 25 minutes the total number of AE for gabbro within 1 hour of monitoring (including 25 minutes of heating and 35 minutes of cooling) was around 1.5 times larger than for granite and around 15 times larger than for schist. The blocks with dry rock generated around two times more AE events than in saturated rock for gabbro and granite. For schist the results for the two saturated blocks were very different and in one case the number of events was higher and in the other lower than in dry schist. For the ratio between the events during heating and cooling a clear trend is found - more events are generated during heating than during cooling. The results are comparable for gabbro and granite although for schist almost all recorded events are only during heating (90-96%). It is interesting to note that a similar difference between saturated and dry blocks for both gabbro and granite is observed. The saturated blocks experience around three times more events during heating than during cooling, while the number of the events in dry blocks was almost the same during heating and cooling.

The magnitude range of the AE events was the same within the blocks of the same rock type but slightly varied among the three rock types. There were events with slightly higher magnitudes in gabbro and granite than in schist.

In all rock types most of the events had E_s/E_p below 5 suggesting that the cracking process during these experiments was predominantly tensile failure. There were still some events with E_s/E_p up to 10. Most of these events (~40-50) were in dry gabbro (A4) around 5 times more than in saturated gabbro (A1). On contrary the saturated granite (G1) experienced two times more events of this type than dry granite (G3). These types of events can be interpreted as shear failure. No events of shear failure type were recorded in schist.

On overall the crack lengths (double the source radius) had similar size distribution for dry and saturated gabbro and granite – between 0.4 and 1.4 mm with some exceptions up to 4 mm. The crack lengths for schist – dry and saturated were smaller and varied in a smaller range between 0.4 and 1.0 mm.

It is important to note also that the AE activity in schist was considerably lower than in gabbro and granite. Most of the events occurred at the beginning of the test until 10 minutes.

Probably, the high AE activity at the beginning was a result of the intense thermal loading, which leads to differential expansion of the layers of different minerals and in turn resulted in debonding of the layers. This probably prevented further heat transfer from the heat source and lead to a decrease and stop of the activity.

The observed trends in the AE emission activity in different types of rocks and different conditions – dry or saturated can be explained by the different mineral composition, but also by the different mechanisms of the AE generation in different types of rock and conditions at different temperatures.

A few different types of AE generation mechanisms were suggested previously. For example, Keshavarz et al. (2010) suggested four types of mechanisms that play a role in micro-crack development (respectively AE generation): (i) Crystal boundary separation due to differential thermal expansion coefficients of the minerals that compose the rocks;(ii) Separation of existing texture within minerals; (iii) Phase transformation of crystals (e.g. in granite due to quartz transformation at 573°C) or oxidation (e-g- oxidation of Fe and Mg in pyroxenes in gabbro above 600°C) and (iv) Bursting of small fluid inclusions due to an increase in temperature. Future analysis has to try to identify which type of mechanism applies to different types of rocks in different conditions and at different temperatures.

6.3.2 LOCAL HEATING

The results from AE monitoring during local heating showed significant differences in the location distribution of the AE events between different types of rock but almost no difference between the blocks of the same type but in different conditions - dry or saturated. In gabbro the AE activity formed linear clusters where the centre corresponds to the visible macro-cracks. The clusters developed from the centre of the block where the heating source was and developed towards the edge of the block. In contrast, the AE activity in granite was concentrated only around the heating source and spread slightly over time. No alignment of the AE locations with visual cracks on the surface was observed. The AE activity in schist was much lower than in gabbro and granite and there was no concentration of the events and no dense clouds formed around the heating source. The comparison between the results from uniform and local heating shows a substantial difference in the pattern of the AE activity. More analysis is required to identify the mechanism of the AE event related to the local heating with a rock mechanical interpretation.

6.4 Numerical analysis

6.4.1 LIMITATION

A limitation of the discontinuous and continuous model is the inability to model the fracturing that occurred along out of plane direction (tunnel axis direction) as the numerical code used for building the model is a 2D program. The laboratory test results of schist blocks showed separation of the blocks along their layer interfaces which are located along the out of plane direction as the layers have a weaker strength compared to the material between layers and it was free of restraints along the out of plane direction. However, for granite and gabbro, the visible fractures observed were either near the tunnel surface or radiated from the tunnel surface and penetrated the whole block. In this case, it can be concluded that the effect of

stress along the out of plane direction has less effect on the results for gabbro and granite blocks.

The effect of vapour pressure on granite and gabbro spallation has been ignored in this numerical modelling. But from the measurement and the observation of laboratory tests, it appears that the vapour pressure influences the spall initiation, as the rapid expansion of fluid within micro pores serves to concentrate stresses at existing sites of weakness. Incorporating the effects of pore fluid content on the spalling response is also clearly important when considering thermal spalling in other rocks (most notably sedimentary rock type) as well as fractured media and should be investigated in the future.

6.4.2 DISCONTINUOUS MODEL

In order to further illustrate the strengths and shortcomings of the discontinuous model (micromechanical model), the fracture distribution at the last stage (stage IV) is compared with the observations in the model tunnel test (gabbro A8, oven-dried, under confinement). As can be seen in Figure 77(a) and (b) from the laboratory test, there are fractures near the tunnel boundary which has produced chips or spalling material and also remote tensile fractures propagating along diagonal and near horizontal directions. Compared with the laboratory test results, the fracture patterns near the tunnel surface and on the front surface of the gabbro block from the numerical model in Figure 77 are quite similar. In the numerical model in Figure 77(c), there are densely distributed fractures near the tunnel boundary but without being fully connected which can explain the observed spalling material and chips. Also, the remote diagonal tensile fractures can represent the ones observed in the laboratory test. However, the near horizontal tensile fractures which appeared on the front surface near the tunnel sidewall of the gabbro block from the laboratory test were not found out in the numerical model. Instead, there is tensile fracture that was propagated in a vertical direction near the tunnel roof of the numerical model. This difference could be attributed to several factors. Firstly, there is a different fire load used in the laboratory test and numerical model. According to the test plan, the fire load (or thermal flux) should be uniformly applied along the tunnel boundary, which is the case in the numerical model. During testing, it was found that the fire flame spreads more towards the sidewall and the roof of the tunnel boundary due to the effect of blowing air. This is confirmed by laboratory tests, in which there is more observed spalling material on the sidewalls and roof for the granite block, see detailed measurements in Taleghani (2013). Secondly, during heating, the spalling material detaches from the tunnel boundary, which causes a change in the thermal boundary condition near the tunnel boundary and further stress distribution. However, the dynamic variation of the thermal boundary condition is not considered in the numerical modelling which might lead to the difference of the fracture distribution between laboratory tests and numerical modelling. Thirdly, the tested rocks contain different minerals randomly distributed in the rocks and the minerals have different thermal and mechanical properties which may create tensile fractures at any places where the stress has just exceeded its local strength. In this case, the tensile fractures might occur along a horizontal direction near the sidewalls ora vertical direction near the roof, since the difference of applied stress (confinement) between x-direction (2.778 MPa) and y-direction (3.333 MPa) is small compared to the thermally induced stress which could be hundreds of MPa. Even the numerical model has the capacity to consider the heterogeneity of rock-forming minerals and random distribution of the minerals, the result only comes from one realization (solution). In this case, the random distribution of material behaviour is not reflected.

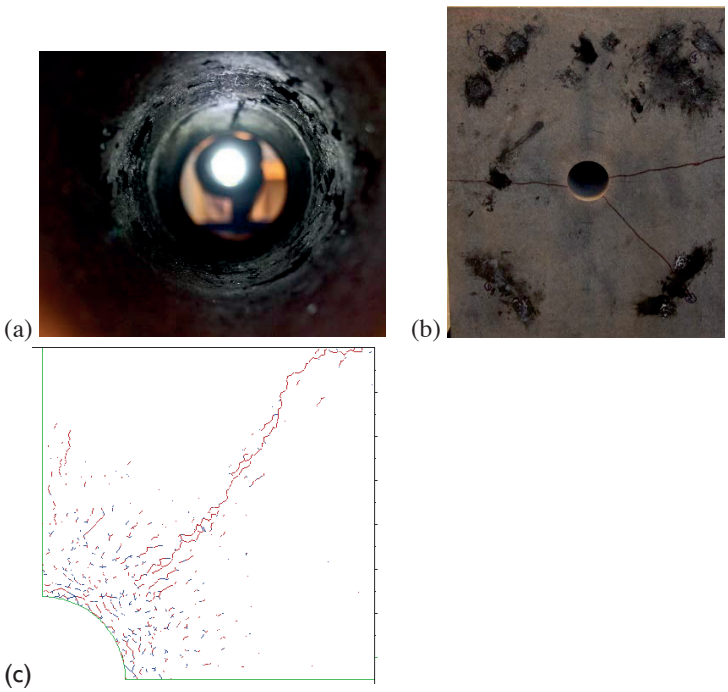

Figure 77 Comparison of fracture distribution between laboratory and numerical results (Gabbro A8, oven-dried, under confinement) ((a) Tunnel surface, (b) Front surface, (c) Numerical modelling)

The results of the grain-scale simulations highlight the importance of microstructural effects in determining the mechanical response of granite and gabbro under thermal spallation conditions. Such high resolution models, while not practical for tunnel scale simulations, are vital in understanding the small-scale processes that drive larger scale phenomena. The main shortcoming of the micromechanical model is that it cannot simulate the change of the dynamic thermal boundary when thermal spalling occurs and material detaches from the block. There is still space to improve the model in order to overcome the shortcoming. Although drawbacks exist, the agreement with laboratory tests illustrates that the modelling approach is able to reveal a complex fracturing process and failure mechanism.

6.4.3 CONTINUOUS MODEL

In order to further illustrate the strengths and shortcomings of the continuous model (macromechanical model), the distribution of plastic regions at the last stage (stage IV) is compared with the observations in the model tunnel test (Granite G7, oven-dried, under confinement). As can be seen in Figure 78(a) and (b) from the laboratory test, there are fractures near the tunnel boundary which have produced large amount of chips or spalling material and also remote tensile fractures propagating along diagonal and near horizontal and vertical directions. Compared to the laboratory test results, the fracture patterns near the tunnel surface and on the front surface of the granite block from the numerical model in

Figure 78(c) are quite similar. In the numerical model in Figure 78(c), there are continuous plastic regions near the tunnel boundary which can explain the observed spalling material. The depth of the plastic regions near the tunnel roof from the numerical model is around 19 mm which can represent the depth of the spalling zone (9-24 mm) from the laboratory test (Taleghani, 2013). Also, the remote plastic regions along diagonal and horizontal directions can represent the fractures observed in the laboratory test. It should be pointed out that by applying dynamic thermal boundary conditions, the numerical model seems to be able to capture the temperature evolution with time development (Figure 79). The major difference is observed between the measured and predicted response at the depth of 2 cm from the tunnel boundary when heating duration is longer than 600 s.

However, as discussed in section 5.3.4, the numerical model shows a large difference compared to the laboratory test when there is a free boundary condition in the model. This difference is mainly caused by using a continuous numerical modelling technique. The continuous numerical model does not have the capacity to simulate the stress release due to initiation and propagation of remote tensile fractures and hence yield a large difference compared with the laboratory tests under free boundary conditions.

(a)  (b) 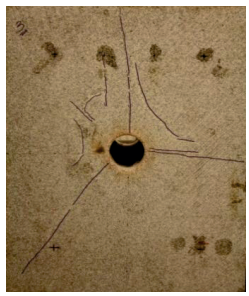

(c) 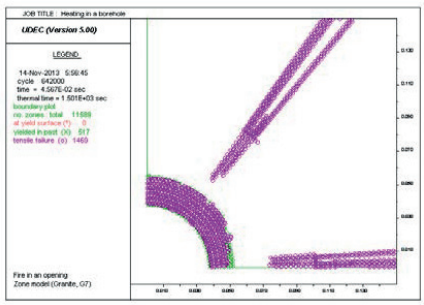

Figure 78 Comparison of fracture distribution between laboratory and numerical results (Granite G7, oven-dried, under confinement) (a) Tunnel surface, (b) Front surface, (c) Numerical modelling

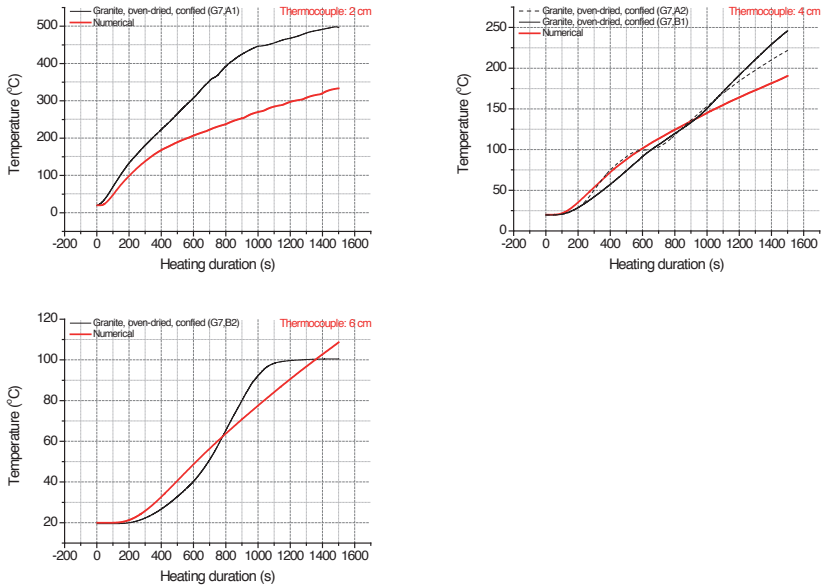

Figure 79 Comparison of temperature evolution at fixed depth from the tunnel boundary between the laboratory test and numerical model (G7, oven-dried, under confinement).

The results predicted using the macro-mechanical model are in reasonable agreement with the important phenomena (e.g. temperature evolution, damage process) recorded or observed from the laboratory tests during the whole heating phases. It is important to have such a model which can be used in real tunnel scale simulations. The main shortcoming of the macro-mechanical (continuous) model is that it does not have the capacity to simulate the stress release due to initiation and propagation of remote tensile fractures. However, in practice, the rock is in a confined condition therefore the shortcoming of the numerical model will have less effects on the final results.

7 CONCLUSIONS

It can be stated that the physical and mechanical properties of all three of the rock types investigated have been influenced to some extent as a result of being subjected to increasing heat intensities. The results clearly suggest that exposure to heat at the variable temperature levels does affect the mechanical, physical and even the chemical properties of the gabbro, granite and schist.

For all of the rock types, similar trends were observed with regard to the variation of their mechanical behaviour when subjected to different temperature levels. The changes in the mechanical properties of the rocks showed reasonable correlation with the mineralogical changes and accompanying changes in the micro-cracks distribution of the rock types at the different temperature levels. The direct relationship between the mineralogical changes of the rocks and their micro-cracks distribution is unclear and as such has not been established here. However, there is a clear relationship between the distribution of micro-cracks and the temperature. With the increase of temperature the distribution of micro-cracks in all minerals is seen to increase.

It is obvious that micro-crack distribution, measured in terms of specific crack lengths, does have an influence on the compressive strengths of the rocks, particularly for the temperature levels of 750°C and 1100°C. At these temperatures the micro-cracking of the minerals such as pyroxene, olivine and mica were observed to be accelerated and accompanying these, a rapid decrease in compressive strength was observed. A slight increase in compressive strength of the rocks is observed for gabbro, granite and schist after heat treatment at the 400°C. It is not clear what caused this slight increase in the strength at this temperature level. Although there is sufficient increase in the micro-cracks at 400°C they do not seem to have significant effect on the samples' mechanical behaviour at this temperature, since it would have an opposite effect on compressive strength by reducing it. However, this increase in the strength coincides with the initial reaction of Fe minerals at 400°C.The iron containing minerals such as olivine and mica were notably reactive at temperatures between 400°C and 750°C. Beyond 750°C it was difficult to identify these minerals as they had become components of the opaque minerals (other phases) that existed as alloys rather than minerals. At 750°C the micro-cracks appeared to have a dominating role on the strength and stiffness of the rock samples. By 1100°C the samples were highly friable and crumbled easily upon compression. In conclusion, the exposure of rocks to any temperature elevation, especially that caused by a tunnel fire which is of a much higher magnitude, will certainly affect the chemical and physical properties of exposed rocks. This will then, in turn affect the mechanical properties of rocks.

The experiment on rock blocks has assessed the behaviour of Fennoscandian rock types, granite, gabbro and schist under different heating conditions (uniformly heated and locally heated) and the response of a model tunnel under fire.

The three tested rock types behaved differently during uniformly and locally heated tests

- Granite: showed substantial explosive spalling chacterized by a sudden forcible separation.
- Gabbro: presented only surface pitting and it was only a temporary process.

- Schist: presented delamination failure along layers due to different thermal expansion between layers and low interfacial bond strength.

The response of the model tunnel within three tested rock types was different under confined conditions during heating.

- The granites show a continuous process of explosive spalling under confined conditions.
- The gabbro suffers only surface pitting.
- Since the naturally existing layers of schist are located perpendicular to the borehole axis, no obvious spalling was observed but the layers separated after the test due to expansion along the borehole axis.

Without confinement, the oven-dried granite shows significantly less spalling. The tests show that the initial compressive stress has facilitated spalling by means of reducing tensile stress within the rock block and increasing the compressive stress concentration near the opening boundary.

These different responses among these three rock types can be attributed to the mineralogy (different minerals, expansion anisotropy) and rock texture. Spalling can result from both restrained thermal dilation and pore pressure. Whether one or the other is dominant depends notably on the rock type and water content.

The results of the grain-scale numerical simulations highlight the importance of microstructural effects in determining the mechanical response of granite and gabbro under thermal spallation conditions. Such high resolution models, while not practical for tunnel scale simulations, are vital in understanding the small-scale processes that drive larger scale phenomena. The main shortcoming of the micromechanical model is that it can not simulate the change of the dynamic thermal boundary when thermal spalling occurs and material detaches from the block. There is still space to improve the model in order to overcome the shortcoming. Although drawbacks exist, the agreement with laboratory tests illustrates that the modelling approach is able to reveal a complex fracturing process and failure mechanism.

The results predicted using the macro-mechanical model are in reasonable agreement with the important phenomena recorded or observed from the laboratory tests during all of the heating phases. It is important to have such a model which can be used in real tunnel scale simulations. The main shortcoming of the macro-mechanical (continuous) model is that it does not have the capacity to simulate the stress release due to initiation and propagation of remote tensile fractures. However, in practice, the rock is in a confined condition therefore the shortcoming of the numerical model will have much less effect on final results.

The results from the analysis of the acoustic emission generated during the process of rock heating (uniform and local) provided valuable information on the number, timing, position, and size of micro-cracks developed in the test blocks during local and uniform heating. The results can be used for studying the rock failure process in heating conditions.

The most general conclusions that could be made from the uniform and local heating tests are:

- Micro-cracking is more substantial in granite and gabbro – a large number of AE are generated during both local and uniform heating. Very few events are generated in schist.
- For all rock types during uniform heating the initiation of micro-cracks takes place 2-3 minutes after the fire start (~700°C oven temperature). While in schist the maximum is reached almost at the same time, in granite and gabbro it takes up to 15 minutes and higher temperature, over~1000°C.
- The propagation of micro-cracks continues also during the cooling process for gabbro and granite but not for schist.
- AE is generated in the whole rock blocks.
- The micro-cracks in all rock types are predominantly tensile but there are also some shear types.
- For all rock types the crack length corresponding to the recorded AE is between 0.4 and 1.4 mm, although there are some micro-cracks up to 4 mm.
- The visual cracks on the surface of the rock blocks correlate very well with the dense AE event location of the rock block.

The AE monitoring conducted in the tests can identify, locate and quantify AE and the damaged areas, allowing for a better understanding of the rock fracture mechanism during heating. The results may be used to characterize the mechanical degradation of the rock mass which experiences high temperatures.

AE events could reveal not only the processes of initiation, development and expansion of micro-fractures inside the rock block but could also give an indication of active weakness planes /zones.

Further study of the mechanisms of the source of the generated AE is necessary. A comparison between the location, length, and type of AE event and the microscopic observations could be very useful for this aim. The AE data could also provide other useful information if a study of the 3D changes in the velocity of the seismic waves in time and space is conducted. As a result the changes in the elastic parameter with the temperature can be studied.

ACKNOWLEDGEMENTS

This work was financially supported by Banverket, Vattenfall, SKB, Formas and BeFo and Centre of Advanced Mining & Metallurgy at LTU (CAMM) which are gratefully acknowledged. The laboratory work was assisted by Roger Lindfors, Mats Petersson and Lars Åström from CompLab, LTU and by Patrik Nilsson, Bijan Adl-Zarrabi, Lars Boström and Robert Jansson from SP. The model tunnel tests were mainly conducted by Pouria Taleghani, LTU. Dimitar Mihaylov from LTU has provided valuable suggestions on improving the model tunnel tests. Faez Sayahi from LTU has assisted in processing the AE data. The authors would like to acknowledge them for their help.

REFERENCES

Adl-Zarrabi B. 2009. Determination of thermal properties of rock material. Technical report: SP Technical Research Institute of Sweden, Båras, Sweden, 10p.
Ahrens T. J. 1995. Mineral Physics and Crystallography Handbook of Physical Constants, AGU Reference Shelf, Vol. 2, American Geophysical Union, USA, 45-63.
Barbish A B. & Gardner G H F. The effect of heat on some mechanical properties of igneous rocks. Society of Petroleum Engineers Journal, 1969.
Bazant Z.P. 2005. Concrete creep at high temperature and its interaction with fracture: recent progress. In: Concreep-7 Conference: Creep. Shrinkage and Durability of Concrete and Concrete Structures, 449-460.
Beard A. and Carvel R. 2005. The handbook of tunnel fire safety. Thomas Telford Publishing, London, UK, 514p.
Boström L. 2009. Fire test on steel fibre reinforced shotcrete with granite. Personal Communication: SP Technical Research Institute of Sweden, Borås, Sweden
Brune, J. N., 1970. Tectonic stress and the spectra of shear waves from earthquakes. Journal of Geophysical Research. 75, 4997-5009
Cai, M., Kaiser, P.K., and Martin C.D., 1998. A tensile model for the interpretation of microseismicevents near underground openings. Pure Appl. Geophys. 153, 67-92.
Carter B. J. 1992. Size and stress gradient effects on fracture around cavities. Rock Mechanics and Rock Engineering, 25(3): 167-186.
Carvel, R., Beard, A., 2005, Chapter 9 in Handbook of Tunnel Fire Safety. Beard and Carvel (eds.), London: Thomas Telford Publ. ISBN:0-7277-3168-8
Chang, Wie-Tun and Giang, Yun-Seng. 1995, Concrete at temperatures above 1000°C. Fire safety Journal, Vol. 23, 223-243
Clauser, C & Huenges, E. 1995. Thermal conductivity of rocks and minerals. American Geophysical Union
Cooper H.W Q. & Simmons G. 1977. The effects of cracks on thermal expansion of rocks. Earth & Planetary Science Letters. Vol 36, Issue 3. pp 404-412.
Diederichs M. S. 2007. The 2003 Canadian geotechnical colloquium: Mechanistic interpretation and practical application of damage and spalling prediction criteria for deep tunnelling. Canadian Geotechnical Journal, 44(9): 1082-1116.
Duclos, R.; and Paquet, J., 1991. High-temperature behaviour of basalts; role of temperature and strain rate on compressive strength and KIc toughness of partially glassy basalts at atmospheric pressure. International Journal of Rock Mechanics and Mining Sciences and Geomechanics Abstracts: 28, 71-76.
Dwivedi R.D ., Goel R.K., Prasad V.V. R., Sinha A. 2007. Thermo-mechanical properties of Indian and other granites. International Journal of Rock Mechanics and Mining Sciences, Vol..45, Issue 3. 303-315
Edelbro C. 2010. Different approaches for simulating brittle failure in two hard rock mass cases: A parametric study. Rock Mechanics and Rock Engineering, 43: 151-165.
Engineering Seismology Group (ESG), 2010. Hyperion Software Suite Version 15.0 (HSS Suite). www.esgsolutions.com. Canada.
Georgali, B. & Tsakiridis, P.E. 2005. Microstructure of fire-damaged concrete. A case study. Cement and concrete composites. Vol. 25. 255-259
Hajiabdolmajida V., Kaiser P. K. and Martin C. D. 2002. Modelling brittle failure of rock. International Journal of Rock Mechanics & Mining Sciences, 39: 731-741.
Hajpal, M. 1999. Burning effects on sandstones of historic buildings and their petrophysical and mineralogical studies. Periodica Polytechnica: Civil Engineering 43, 207-218.

Hajpál M. 2002. Changes in sandstones of historical monuments exposed to fire or high temperature. Fire Technology, 38(4): 373-382.
Hajpál M. 2004. Mineralogical and colour changes of quartz sandstones by heat. Environmental geology, 46(3-4): 311-322.
Hajpal M. & Török A. 2004. Mineralogical and colour changes of quartz sandstones by heat. In Environmental Geology. Vol. 46, No.. 3-4, pp 311-322, DOI: 10.1007/s00254-004-1034-z
Hajpal, M. Burning effects on sandstones of historic buildings and their petrophysical and mineralogical studies. Periodica Polytechnica: Civil Engineering 1999. 43, 207-218.
Hettema M. H. H. 1996. The thermo-mechanical behaviour of sedimentary rock: an experimental study. Ph.D thesis: Delft University of Technology, Delft, The Netherlands, 319p.
Hettema M. H. H., Wolf K-H. A. A. and Pater C. J. DE. 1998. The influence of steam pressure on thermal spalling of sedimentary rock: Theory and experiments. International Journal of Rock Mechanics and Mining Sciences, 35(1): 3-15.
Heuze, F.E., 1983. High-temperature mechanical, physical and thermal properties of granitic rocks - a review. International Journal of Rock Mechanics and Mining Science & Geomechanics Abstracts. 20(1), 3–10
Homand, F., Troalen, J. P., 1984. Behaviour of granites and limestone subjected to slow and homogeneous temperature changes. Eng. Geol. 20, 219-33.
Hommand-Etienne, F.; and Houpert R., 1989. Thermally induced micro-cracking in granites: characterisation and analysis. International Journal of Rock Mechanics and Mining Science & Geomechanics Abstracts. 26, 125–34.
Hueze F E. High-temperature mechanical, physical and thermal properties of granitic rocks-A Review. International Journal of Rock Mechanics and Mining Sciences & Geomechanics Abstracts, 1983, Vol. 20, No.1, pp 3-10.
Itasca Consulting Group. 2013. UDEC-Universal Distinct Element Code, Version 5.0, User Manual, Minnesota, USA.
Jansen, D. P., Hutchins, A. D., and Young R. P. 1993. Ultrasonic imaging and acoustic emission monitoring of thermally induced micro-cracks in Lac du Bonnet granite. J. Geophys., 98, 22231–22243.
Jansson R. and Boström L. 2008. Spalling of concrete exposed to fire. SP report 2008: 52, SP Technical Research Institute of Sweden, Borås, Sweden, 286p.
Jansson R. and Boström L. 2010 The influence of pressure in the pore system on fire spalling of concrete. Fire Technology, 46(1): 217-230.
Jonsson K. 2009. Preliminary testing and numerical analysis - Project status report. Research report: Luleå University of Technology, Luleå, Sweden, 29p
Keshavarz, M.; Pellet, F. L.; Loret, B., 2010. Damage and changes in mechanical properties of a gabbro thermally loaded up to 1,000 degrees C. Pure and Applied Geophysics. 167, 1511–1523.
Keski-Rahkonen O., Holmlund C., Loikkanen P., Ludvigsen H. and Mikkola E. 1986. Two full scale pilot fire experiments in a tunnel. Research report: Technical Research Centre (Valtion Teknillinen Tutkimuskeskus, VTT), Espoo, Finland, 149p.
Khoury G. A. 2000. Effect of fire on concrete and concrete structures. Progress in Structural Engineering and Materials, 2(4): 429-447.
Kingery W. D., Bowen H. D. and Uhlmann D. R. 1976. Introduction to ceramics. 2nd ed., John Wiley & Sons, New York, USA, 1056p.
Kwiatek, G., and Y, Ben-Zion.; 2013. Assessment of P and S wave energy radiated from very small shear-tensile seismic events in a Deep South African mine. J. Geophys. Res. Solid Earth. 118, 3630–3641.

Lan H. X., Martin C. D. and Andersson J. C. 2013. Evolution of in situ rock mass damage induced by mechanical – thermal loading. Rock Mechanics and Rock Engineering, 46: 153-168
Larsson K. 2006. Fires in tunnels and their effect on rock - A review. Research report: Luleå University of Technology, Luleå, Sweden, 60p.
Madariaga, R.; 1976. Dynamics of an expanding circular fault. Bulletin of the Seismological Society of America. 66(3), 639-666.
Markwell S J. High temperature deformation of dry diabase with application to tectonics on Venus. Journal of Geophysical Research, Vol. 13 pp 975-984, 1998
Martin C. D., Martino J. B. and Dzik E. J. 1994. Comparison of borehole breakouts from laboratory and field tests. Eurock'94, Balkema, Rotterdam, 183-190.
Martin C. D. and Christiansson R. 2009. Estimating the potential for spalling around a deep nuclear waste repository in crystalline rock. International Journal of Rock Mechanics & Mining Sciences, 46: 219-228.
Martin C. D. 2013. Personal Communication, Sweden
Mavko G., Mukerji T. and Dvorkin J. 2003. The Rock Physics Handbook: Tools for Seismic Analysis of Porous Media. Cambridge University Press, Cambridge, UK, 329p.
Mindeguia, J. C., Pimienta P., Noumowé A. and Kanema M. 2010. Temperature, pore pressure and mass variation of concrete subjected to high temperature - Experimental and numerical discussion on spalling risk. Cement and Concrete Research, 40(3): 477-487.
Miskovsky K. Värmebehandlingen inverkan på mekansika egenskaper hosgrovballast bestående av graniter och ortognejser, Institution for miljö- och hälsoskydd, Umeå Univesitet. 1991
Nelder, J. A., Mead. R. 1965. A Simplex Method for Function Minimization. The Computer Journal. 7, 308-313.
Poirier S., Fecteau J.-M., Laflamme M. and Brisebois D. 2003. Thermal rock fragmentation - Applications in narrow-vein extraction. CIM Bulletin, 96(1071): 66-71.
Preston, F. W. and White H. E. 1934. Observations on spalling. Journal of the American Ceramic Society, 17: 137-144.
Promat. 2014. Fire curves. http://www.promat-tunnel.com/en/advices/fire-protection/fire%20curves
Rao, Q., Wang, Z., Xie, H., Xie, Q. 2007. Experimental study of mechanical properties of sandstone at high temperature. In Journal of Central South University of Technology, Volume 14, Supplement 1, pp 478-483.
Rauenzahn R. M. and Tester J. W. 1989. Rock failure mechanisms of flame-jet thermal spallation drilling-theory and experimental testing. International Journal of Rock Mechanics and Mining Sciences & Geomechanics Abstracts, 26(5): 381-399.
Ritcher D. & Simmons G. 1974. Thermal expansion behaviour of igneous rocks. International Journal of Rock Mechanics and Mining Sciences and Geomechanics, Volume 11, pp 403-411.
Robertson E. C. 1988. Thermal properties of rocks. Open-File Report 88-441: United States Department of the Interior Geological Survey. USA.
Saiang C. 2011. Influence of heat on the physical and mechanical properties of selected rock types, Licentiate thesis: Luleå University of Technology, Luleå, Sweden, 115 p.
Smith, A.G. & Pells, P.J.N. 2008. Impact of fires on tunnels in Hawkesbury sandstone. In Tunnelling and Underground Space Technology. Vol.23, Issue 1, 65-74.
Smith A. G. and Pells P. J. 2009. Discussion of the paper "Impact of fire on tunnels in Hawkesbury sandstone" by Smith and Pells [Tunnelling and Underground Space Technology 23 (2008) 65-74]. Tunnelling and Underground Space Technology, 24(1): 112-114.

Sommerton, W. H. 1992. Thermal properties and temperature-related behaviour of rock/fluid systems. Armsterdam; Elsiever Science Publishers. ISBN 0-444-89001-7
Takarli, M. & Prince Agbodjan, W. 2011. Temperature effects of physical and mechanical behaviour of granite : Experimental investigation of material damage. Journal if ASTM International, Vol..5, No 3
Taleghani P. 2013. Laboratory test on thermal spalling and cracking around cylindrical opening in rock under bi-axial loading condition. Master thesis: Luleå University of Technology, Luleå, Sweden, 93 p.
Tratebas A. M., Cerveny N. V. and Dorn R. I. 2004. The effects of fire on rock art: Microscopic evidence reveals the importance of weathering rinds. Physical Geography 25(4): 313-333.
Williams R. E., Potter R. M. and Miska S. 1996. Experiments in thermal spallation of various rocks. Journal of Energy Resources Technology, 118(1): 2-6.
XU Xiao-li1, GAO Feng1, SHEN Xiao-ming and XIE He-ping. 2008. Mechanical characteristics and microcosmic mechanisms of granite under temperature loads: Journal of China University of Technology, 18 (2008) 0413-0417.
Zhang L Y, Mao X B & Lu, A H. 2009.Experimental study on the mechanical properties of rocks at high temperature. Science in China, Series E: Technological Sciences, Vol 52. No.3, 641-646.
Zhang P., Li N., Li X. B. and Nordlund E. 2009. Compressive failure model for brittle rocks by shear faulting and its evolution of strength components. International Journal of Rock Mechanics and Mining Sciences, 46(5): 830-841.
Zhang, P., Nordlund, E., Mainali, G., Saiang, C. Jansson, R. & Adl-Zarrabi, B. 2010. Experimental study of thermal spalling of rock blocks exposed to fire. Bergmekanik I Norden 2010 (Rock mechanics in the Nordic countries 2010): Konsberg, Norway, 9-12. June 2010. Li, C.C (Ed) 294-305.
Zhang P., Nordlund E., Mainali G., Saiang C. and Jansson R. 2011. Experimental study of thermal spalling on rock blocks exposed to different fire/heating conditions. Bergmekanikdag 2011, 53-63.

BeFo

Box 5501
SE-114 85 Stockholm

info@befoonline.org • www.befoonline.org
Visiting address: Storgatan 19

ISSN 1104-1773